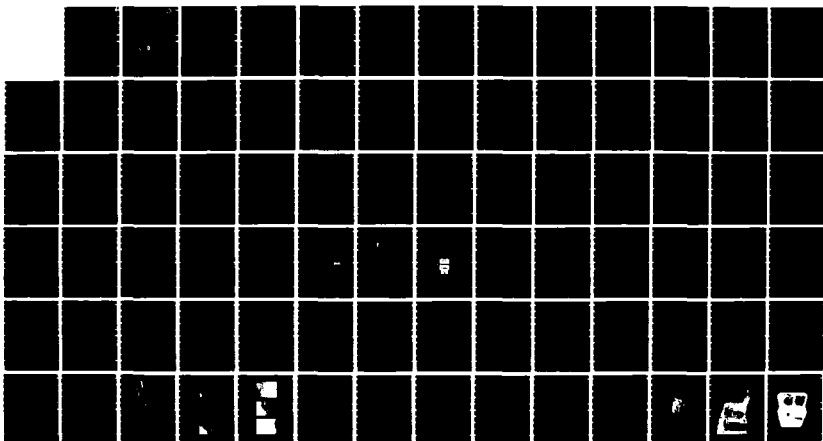


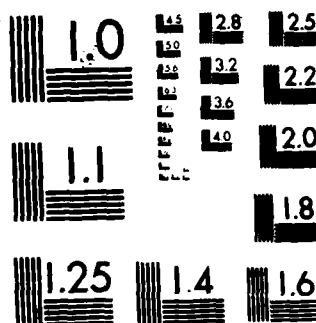
NO-A179 888 ION BEAM PROCESSING(U) NAVAL RESEARCH LAB WASHINGTON DC 1/1  
G K HUBLER 13 MAR 87 NRL-MR-5928

UNCLASSIFIED

F/G 13/8

NL





MICROCOPY RESOLUTION TEST CHART  
NATIONAL BUREAU OF STANDARDS 1963 A



NRL Memorandum Report 5928

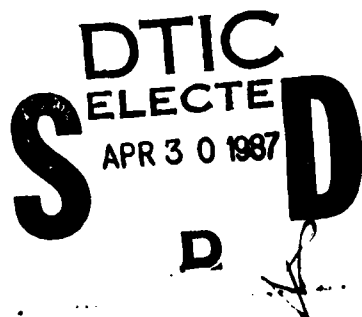
AD-A179 880

## Ion Beam Processing

G. K. HUBLER

*Materials Modification and Analysis Branch  
Condensed Matter and Radiation Sciences Division*

March 13, 1987



Approved for public release; distribution unlimited.

87 4 00 084

SECURITY CLASSIFICATION OF THIS PAGE

A179880

## REPORT DOCUMENTATION PAGE

1a. REPORT SECURITY CLASSIFICATION UNCLASSIFIED			1b. RESTRICTIVE MARKINGS		
2a. SECURITY CLASSIFICATION AUTHORITY			3. DISTRIBUTION/AVAILABILITY OF REPORT Approved for public release; distribution unlimited.		
2b. DECLASSIFICATION/DOWNGRADING SCHEDULE					
4. PERFORMING ORGANIZATION REPORT NUMBER(S) NRL-Memorandum Report 5928			5. MONITORING ORGANIZATION REPORT NUMBER(S)		
6a. NAME OF PERFORMING ORGANIZATION Naval Research Laboratory		6b. OFFICE SYMBOL (If applicable)		7a. NAME OF MONITORING ORGANIZATION	
6c. ADDRESS (City, State, and ZIP Code) Washington, DC 20375-5000			7b. ADDRESS (City, State, and ZIP Code)		
8a. NAME OF FUNDING/SPONSORING ORGANIZATION Office of Naval Research		8b. OFFICE SYMBOL (If applicable)		9. PROCUREMENT INSTRUMENT IDENTIFICATION NUMBER	
8c. ADDRESS (City, State, and ZIP Code) Arlington, VA 22217			10. SOURCE OF FUNDING NUMBERS		
			PROGRAM ELEMENT NO. 61153N	PROJECT NO. RR022- 06-42	TASK NO. WORK UNIT ACCESSION NO. DN280 062
11. TITLE (Include Security Classification) Ion Beam Processing					
12. PERSONAL AUTHOR(S) Hubler, G.K.					
13a. TYPE OF REPORT Final		13b. TIME COVERED FROM TO		14. DATE OF REPORT (Year, Month, Day) 1987 March 13	
15. PAGE COUNT 83					
16. SUPPLEMENTARY NOTATION					
17. COSATI CODES			18. SUBJECT TERMS (Continue on reverse if necessary and identify by block number)		
FIELD	GROUP	SUB-GROUP	Ion implantation Ion beam analysis		
			Surface modification Ion beam processing → end page (Cont'd)		
19. ABSTRACT (Continue on reverse if necessary and identify by block number)					
<p>The primary purpose of this memo is to introduce ion implantation processing to materials scientists and engineers who have no prior experience with surface modification with ion beams. The introduction and background sections inform the reader as to the kinds of applications that might be considered for ion implantation processing and give a brief description of the apparatus and the physical principles underlying the techniques. In subsequent sections, the entire process of ion beam processing is described in enough detail that the reader will have a sufficient grasp of the technology to be able to plan treatment parameters for parts and/or to double-check treatment parameters recommended by vendors.</p> <p>A secondary purpose is to provide workers already in the field with a handbook of tables, graphs and equations that are needed for doing ion implantation processing. These include tables of ion ranges and straggling, formulae and tables which allow estimates to be simply made for sputtering coefficients, depth profiles of implanted elements, damage profiles, dose for sputter saturation of implanted profiles, temperatures reached by parts in vacuum during implantation, and estimates of the time and cost of ion implantation.</p>					
20. DISTRIBUTION/AVAILABILITY OF ABSTRACT <input checked="" type="checkbox"/> UNCLASSIFIED/UNLIMITED <input type="checkbox"/> SAME AS RPT. <input type="checkbox"/> DTIC USERS			21. ABSTRACT SECURITY CLASSIFICATION UNCLASSIFIED		
22a. NAME OF RESPONSIBLE INDIVIDUAL G.K. Hubler			22b. TELEPHONE (Include Area Code) (202) 767-4800		22c. OFFICE SYMBOL Code 4671

DD FORM 1473, 84 MAR

83 APR edition may be used until exhausted.  
All other editions are obsolete.

SECURITY CLASSIFICATION OF THIS PAGE

18. SUBJECT TERMS

Corrosion,	Wear
Ion Range,	Straggling
Sputtering,	Alloy formation
Materials processing,	Tribology
Applications of ion implantation	



Accession For	
NTIS CRA&I	<input checked="" type="checkbox"/>
DTIC TAB	<input type="checkbox"/>
Unannounced	<input type="checkbox"/>
Justification	
By	
Distribution/	
Availability Codes	
Dist	Avail and/or Special
A-1	

## CONTENTS

I.	INTRODUCTION .....	1
II.	ION IMPLANTATION BACKGROUND .....	2
	A. Applications .....	2
	B. Description of Ion Implantation Process .....	3
	C. Comparison to Coating Techniques .....	3
	D. Historical Perspective .....	4
	E. Ion Implantation - Advantages and Limitations of the Technique .....	4
	F. Ion Implantation Equipment .....	5
III.	RADIATION DAMAGE AND PHASE FORMATION .....	7
	A. Introduction .....	7
	B. The Structure of Radiation Damage .....	7
	C. Annealing of Damage .....	8
	D. Damage at High Dose .....	8
	E. Final Site of Implanted Ions .....	9
	F. Phase Formation .....	10
IV.	ION BEAM PROCESSING .....	11
	A. Introduction .....	11
	B. Ion Range Parameters .....	11
	i. General Features of Range Distributions .....	11
	ii. Ion Range Tables for Elemental Targets .....	12
	C. Sputtering .....	17
	D. Atomic Fraction of Implanted Ions .....	18
	i. Low Dose Concentration for all Ion Masses .....	18
	ii. High Dose Concentration for Light Ions: $M_1 \lesssim 20$ .....	19
	iii. High Dose Concentration for Heavy Ions: $M_1 \gtrsim 20$ .....	19
	iv. Comparison of Calculated Profiles to Experimental Results .....	23
	E. Selected Experimental Range Profiles .....	24
	F. Influence of Masking .....	24
	G. Topographical Changes .....	25
	H. Workpiece Manipulation .....	25
	I. Workpiece Cooling .....	25
	J. Examples of Fixtures for Manipulation and Cooling .....	27
	K. Cleaning of Workpiece .....	28
	L. Size of Workpiece .....	29
	M. Implantation Time and Cost .....	29

V.	DETERMINATION OF IMPLANT PARAMETERS AND QUALITY CONTROL .....	31
	A. Flat Geometry Workpiece .....	31
	B. Cylindrical geometry Workpiece .....	33
	C. Quality Control .....	35
VI.	SUMMARY .....	36
VII.	ACKNOWLEDGMENTS .....	36
VIII.	REFERENCES .....	37

# ION BEAM PROCESSING

## I. INTRODUCTION

The primary purpose of this memo is to introduce ion implantation processing to materials scientists and engineers who have no prior experience with surface modification with ion beams. The introduction and background sections inform the reader as to the kinds of applications that might be considered for ion implantation processing and give a brief description of the apparatus and the physical principles underlying the techniques. In subsequent sections, the entire process of implantation processing is described in enough detail that the reader will have a sufficient grasp of the technology to be able to plan treatment parameters for parts and/or to double-check treatment parameters recommended by vendors. Thus, this memo explains what ion implantation technology is, how to actually implant ions into surfaces and gives examples of parts where it has been successfully used.

A secondary purpose of the chapter is to provide workers already in the field with a handbook of tables, graphs and equations that are needed for doing ion implantation processing. A few of the expressions or tables are original but most of the information contained in the chapter has appeared elsewhere in the literature and is collected here for convenient reference.

Ion implantation processing of metals is now a viable alternative treatment for specific wear and corrosion applications, with vendors distributed in the U.S., U.K., Europe and Japan that provide service where parts can be treated. The gross dollar amount of business for implantation processing of metals is negligible when compared to other treatments such as plasma deposition, thermal spraying, sputter deposition, etc., but the field has generated great interest and is developing along a typical growth curve for a high technology industry. The primary function of the vendors is to treat surfaces for companies that are doing research and development of a proprietary nature that involves the implantation of a limited number of parts for industrial trials. Some applications have reached the production stage where a large number of parts have been treated and it is anticipated that the number of applications reaching production will increase.

Why is ion implantation technology useful? One way to answer this question is by viewing the entire field with the aid of Fig. (1.1). It presents a periodic table of the elements which is coded with letters in the corners to indicate if the implanted element is used to improve oxidation (O), aqueous corrosion (C), wear (W) or fatigue (F). In Fig. (1.1), all metals that have been implanted are included as the substrate base (e.g., iron and ferrous alloys, Ti and Ti alloys, etc.) and the ions cited in the figure are only those which had the greatest effect. Several features of this periodic chart are worth noting: i) some elements improve more than one property. ii) Ion implantation is a versatile process because it can forcibly inject any element in the periodic table into a surface. iii) Elements from nearly all the groups of the periodic table can have beneficial effects on a given property. iv) Ions which improve properties are highlighted here, but ions which have deleterious effects may also be implanted which facilitates the study of mechanisms of wear and corrosion. v) Elements to implant may be chosen for a particular property with respect to the substrate such as atomic size, electronegativity, whether the oxides are n or p type semiconductors or insulators, catalytic tendency, to name a few, and in most cases the element will form a solid solution alloy independent of the rules of thermodynamic equilibrium. Thus, the interest in ion implantation lies in the unparalleled freedom of choice in the selection of ions to treat and/or study various surface sensitive properties.

This memo first informs the reader of the types of applications under investigation or in use and then introduces the general features of ion implantation. This includes a brief description of the process of injecting ions into the surface, a description of implantation equipment, comparisons with other surface treatments, and a complete accounting of the advantages and disadvantages of ion implantation processing. Section III discusses the physical processes of radiation damage and phase formation that occur during high dose implantation and provides a simple picture of the development of microstructures that enhance mechanical properties. Section IV gives a detailed account of the procedures used to ion implant metal parts including: calculation of the concentration versus depth of the implanted ions; manipulation and cooling of the workpiece, and estimation of the time and cost of the treatment. The



last section provides case studies where implantation treatments are planned and the treatment parameters selected in a step-by-step procedure that illustrates the use of the formulas and tables that are given in the chapter.

## II. ION IMPLANTATION BACKGROUND

### A. Applications

Ion implantation is used in applications and research to modify many surface sensitive properties. Table (2.1) is a partial list of these properties and shows that ion implantation can be applied to many materials problems. Although metals are emphasized in this chapter, ion implantation is used to modify other materials such as semiconductors, ceramics, insulators and polymers because it is universally applicable to any solid material.

Table 2.1 — Surface Sensitive Properties Modified by Ion Implantation

Wear	Corrosion	Resistivity
Friction	Oxidation	Dielectric Constant
Fatigue	Catalysis	Superconductivity
Hardness		
Adhesion		
Toughness		

A partial list of applications of ion implantation to metals is given in Table (2.2). From this list one can acquire a good overall view of the types of parts that may be treated using ion implantation and the kinds of problems to which it is being applied. Some general points of interest are worth noting: i) the workpieces that are treated with ion implantation are not large, seldom exceeding 10 inches in length or diameter. ii) the workpieces usually have a polished surface finish. iii) most applications are for improvement of wear or corrosion resistance. iv) many items are high technology, expensive parts or tooling. These points show that the focus of applications is on small, high-cost, critical parts or tools used in the manufacturing of parts.

Table 2.2 — Selected Examples of Applications of Ion Implantation

Paper slitting knives	Printed circuit board drills
Rubber slitting knives	Wire guides
Taps for plastics	Orthopedic implants (hip and knee joints, etc.)
Extrusion spinnerettes	Finishing rolls for copper rod
Extrusion nozzles	Punches for acetate sheet
Extrusion dies	Tool inserts
Pellet punches for nuclear fuel	Fuel injectors and metering pumps
Forming dies for cans	Cam followers
Scoring dies for cans	Cutters of plastics
Rolling elements bearings for air and space	Precision punches for electronic parts
Instrument bearings	Swaging dies and press tools for wheels
Gas bearings	Injection mold nozzles and screws
Wire drawing dies for Cu, Mo	Gears for ultra high vacuum manipulators
Dental drills	

Every surface modification technique has advantages and disadvantages that ultimately determine its applicability. Table (2.3) is a list of criteria for when ion implantation should be considered as the treatment of choice, and it is based upon the advantages and disadvantage that are discussed in detail later in this section. If any one of these criteria or features are important then ion implantation bears a close look as a possible solution, and further reading of this chapter is recommended.

Table 2.3 — Criteria/Features Influencing the Applicability  
of Ion Implantation

Ion implantation should be considered when -

1. Low process temperature is required (although not a necessary condition)
2. Maintenance of high tolerances and/or surface finish is desired
3. Superior adherence of treated surface is important
4. Reproducibility and control of process is necessary
5. Parts to be treated are small, high-cost, and critical to operation of a system
6. Surface layer of 0.1 to 1.0 microns remains intact during service life (note that lifetime is frequently improved by factors of 2 to 100 by treatment)
7. There is a line-of-sight access to the surfaces requiring treatment (a necessary condition)

#### **B. Description of Ion Implantation Process**

Ion implantation is a process by which virtually any element can be injected into the near-surface region of any solid by causing a beam of high-velocity ions, usually 10 to 400 keV in energy, to strike a target mounted in a vacuum chamber. The incident ions come to a stop at depths of tens to thousands of angstroms (i.e., 0.01 to 1  $\mu\text{m}$ ) in the host material as a result of losing energy during collisions with substrate atoms. The resulting depth concentration profile of implanted dopant atoms can be calculated for any projectile-target combination from well established theoretical considerations. At low ion doses (i.e., the number of ions per unit area), the depth concentration profiles are well characterized by a Gaussian distribution centered about an average projected range. During the slowing down process, collisions between the incident projectile ions and the target atoms result in the displacement of target atoms. This process is called radiation damage and will be discussed later in more detail. At high fluences, where the concentration of implanted atoms approaches tens of atomic percent, other effects such as sputtering and ion beam induced migration of atoms can significantly alter or limit the ultimate concentrations attainable. There is a probability of atoms being ejected (sputtered) from the surface of the target as a result of collisions in the surface region, especially for heavier mass incident projectiles. An equilibrium condition is eventually reached where as many implanted atoms are removed by sputtering as are replenished by implantation. The depth distribution of implanted atoms under this condition typically has a maximum at the surface and falls off over a distance comparable to the initial ion range. Figure (2.1) is a schematic demonstration of the development of the atomic concentration profile during a high dose implantation. Depth concentrations, radiation damage, sputtering and phase formation are discussed in greater detail in following sections.

#### **C. Comparison to Coating Techniques**

Because ion implantation is a process that modifies surface properties it is often compared with conventional techniques, such as physical vapor deposition, chemical vapor deposition, and ion plating, which are all used for enhancing surface properties such as corrosion or wear resistance. It shares a number of advantages with these techniques but also has basic limitations. Therefore, it is important to understand the differences between ion implantation and coating techniques, especially ion plating. The result of ion implantation into materials is the formation of a surface alloy of graded composition that possesses no well-defined interface with respect to the substrate, in contrast to a deposited layer where the interface is very abrupt. The thickness of the implanted region is typically less than 2000

Angstroms ( $\text{\AA}$ ) for implantation energies of 100 keV (1000  $\text{\AA}$  for heavy ions). In ion plating, however, the coating is typically much thicker, and its composition is independent of the nature of the substrate. Although ion plating is often carried out with the substrates electrically biased at several keV, the mean energy of the charged particles reaching the surface is of the order of only 100 eV. This occurs because only a small fraction ( $\sim 10\%$ ) of the particles are ionized when they reach the substrate. Hence, there is virtually no penetration of the incident beam into the substrate. Ion plating is carried out under a relatively high pressure that causes atomic collisions and scattering. This factor is responsible for the high "throwing power" of the ion plating technique versus the "line-of-sight" limitation of implantation.

#### D. Historical Perspective

Since the early 1970's, ion implantation has been extensively used by the semiconductor device industry as a method of introducing controlled amounts of dopants into the surface region of semiconductor substrates. Its principal advantages for this application include improved controllability and reproducibility for device fabrication, as compared to thermal diffusion. The absolute concentration of implanted atoms and the uniformity across the sample surface may be controlled to better than 5% and 1% respectively. The volume concentrations of impurities required for semiconductor applications typically range from parts per million to as high as 0.1 at.%, whereas the concentrations required for many of the non-semiconductor applications, such as for bearings, are typically ten to thirty atomic percent. Development of techniques and equipment for ion implantation is driven by the semiconductor industry; the equipment for implantation of metals is a spin-off from that effort. Therefore, the technology ion implantation of metals advances along with technological progress in the semiconductor field.

#### E. Ion Implantation - Advantages and Limitations of the Technique

Some of the advantages and limitations of ion implantation in comparison to other surface treatments (such as coatings) are listed in Table (2.4).

Table 2.4 — Advantages and Limitations of Ion Implantation  
as a Surface Modification Technique

Advantages	Limitations
(1) Low temperature process	(1) Line-of-sight process
(2) No significant dimensional changes	(2) Shallow penetration
(3) <i>No adhesion problems since there is no sharp interface</i>	(3) Relatively expensive equipment and processing costs
(4) No sacrifice of bulk properties	
(5) Solid solubility limit can be exceeded	
(6) Alloy preparation independent of diffusion constants	
(7) Allows fast screening of the effects of changes in alloy composition	
(8) Depth concentration distribution controllable	
(9) Highly controllable and reproducible	

The chief advantages of ion implantation are low temperature processing (no distortion of part), no change in dimensions (no refinishing required), excellent adhesion of the implanted surface, and that the surface properties can be optimized independently from the bulk properties. The fact that ion implantation is a nonequilibrium, fast quench technique permits the formation of surface alloys independently of solubility limits and diffusivities that govern conventional alloy formation.

Ion implantation often allows the convenient production and subsequent study of surface alloys with well defined compositions. In this manner the technique can be used as a powerful research tool to examine the physical state of alloys as a function of varying alloy composition. Using implantation alloying one can avoid changing other parameters (e.g., grain size) which may effect the property of interest such as oxidation behavior.

A basic limitation of ion implantation is that as a line-of-sight process, it is not feasible to apply it to samples having complicated re-entrant surfaces. The shallow depth of penetration would seemingly limit the technique for engineering applications; however, there are many situations involving both physical and chemical properties in which the effect of the implanted ions is to change the mode of wear or corrosion behavior resulting in significant extension of lifetime of the part. The disadvantages determine the applicability of a process. The limitation of shallow depth and relatively high cost imply that the most appropriate applications are for high cost, high technology critical parts which limit the performance or lifetime of end use hardware or expensive tools used in the production of hardware.

#### **F. Ion Implantation Equipment**

A typical production-type ion implanter is shown in Fig. (2.2). It consists of an ion source capable of producing ion beams of practically any stable element. Ions are extracted from the ion source by an electrode held at high potential. Since ion sources normally produce ions of several species in addition to the one desired for implantation, it is ordinarily essential to mass-analyze the beam in order to allow only the species of interest to continue toward the target. The separation of the isotopes of Cr is depicted here. After mass analysis, the beam is accelerated through an evacuated acceleration column during passage from the high voltage terminal to ground potential. After acceleration the beam is electrostatically focussed and raster scanned over an aperture held in front of the target to ensure uniformity. The ion beam current striking the target is then current integrated to obtain the impurity concentration (in dimensions of atoms per unit area) which in turn can be converted into a volume concentration by knowledge of the range-energy relationships for the projectile-ion host combination. A schematic diagram of a typical ion source for metals implantation is shown in Fig. (2.3). A low pressure plasma is sustained by an arc discharge voltage of 100V and by a hot filament to supply electrons. The positive ions that are extracted from the plasma through a 25kV potential can be composed of the gas used to sustain the arc discharge, or of metallic ions derived from volatile metal chlorides produced in a reaction chamber in the rear of the ion source. Ion beams of most of the elements in the periodic table can be produced in this simple ion source configuration.

Non-mass analyzed implanters are available for applications requiring ions formed from pure gases and are cheaper to manufacture. The newest generation commercial implanters are capable of beam currents of 10 mA, and development of 100 mA machines is in progress. The flux of ions for these beam currents is  $6.2 \times 10^{16}$  and  $6.2 \times 10^{17}$  ions/s, respectively. A typical dose for metals implantation is  $2 \times 10^{17}$  ions/cm<sup>2</sup>. The time required to treat one square inch of flat surface with these beam currents would be 21 seconds and 2.1 seconds, respectively.

This introduction to implantation has been very brief because the process itself is straight-forward and therefore easy to understand. For further reading on the equipment or other aspects of ion implantation covered in this report, the references cited in Table (2.5) are recommended.

Table 2.5 — References for Information Related to Ion Implantation

1. **Applications**  
P. Sioshansi, Thin Solid Films **118** (1984)61  
R.E. Hoisington, D.E. Technology, (Jan. 1984)10.
2. **Catalysis**  
G.K. Wolf, Nucl. Instrum. and Meth. **182/183** (1981)875.
3. **Corrosion**  
C.R. Clayton, Nucl. Instrum. and Meth. **182/183** (1981)865.
4. **Deformation**  
D.A. Hills and D.W. Ashelby, Wear **75** (1982)221.
5. **Equipment and Techniques**  
G. Dearnaley and P.D. Goode, Nucl. Instrum. and Meth. **189** (1981)117.  
J.W. Butler, Encyclopedia of Chemical Technology (John Wiley, 1981)  
Vol. 13, p. 706.
6. **Fatigue (Ion Implantation)**  
R.G. Vardiman, in "The Application of Ion Plating and Ion  
Implantation to Materials" Ed., R.W. Hockman, ASM, (1986).
7. **General Ion Implantation Review**  
S.T. Picraux, Ann. Rev. Mater. Sci. **14** (1984)335.
8. **Oxidation**  
K.S. Grabowdki and L.E. Rehn, in "Corrosion of Metals Processed by  
Directed Energy Beams" (eds., C.R. Clayton and C.M. Preece, The  
Metallurgical Society of AIME, Louisville, Kentucky, 1981) p. 23.
9. **Phase Formation**  
S.T. Picraux, in "Site Characterization and Aggregation of Implanted  
Atoms in Materials" (eds., A. Perez and R. Coussement; Plenum NY,  
1980) pp. 307 and 325.
10. **Wear**  
"Fundamentals of Friction and Wear of Materials," Ed., D.A. Rigney,  
ASM, Metals Park, OH (1981).
11. **Wear (Ion Implantation)**  
I.L. Singer, Materials Research Society Symp. Proc. Vol. **27**  
(Elsevier, NY, 1984) p. 585.

### III. RADIATION DAMAGE AND PHASE FORMATION

#### A. Introduction

This section gives a brief introduction to the basic processes that occur on an atomic scale during ion implantation in order to provide an understanding of how the composition and microstructure of surfaces are modified as the ion dose increases and impurity atoms are forced into a crystalline host to concentrations of 10 to 30 atomic percent.

An energetic ion loses energy in its passage through a solid via electronic and atomic collisions. As far as damage is concerned, electronic collisions do nothing more than heat up the lattice (Czjzek et al., 1968). On the other hand, atomic collisions can recoil lattice atoms with energies well in excess of the minimum energy for displacement,  $E_D$  which for most materials is  $\sim 30$  eV, and the recoils consequently undergo further collisions with other lattice atoms before they themselves come to rest. This multiplication process is called a "collision cascade" and for incident energies relevant to ion implantation (10 to 400 keV) can involve thousands of atoms and result in hundreds of atoms becoming permanently displaced from equilibrium lattice sites. Holes which remain in the crystalline lattice after displacement are called vacancies, and the displaced atoms which become squeezed into the lattice are called interstitials. These vacancies, interstitials and defect aggregates produced by atomic collisions comprise what is commonly called "radiation damage." Figure (3.1) illustrates a possible sequence of events in a single collision cascade.

The maximum energy that a lattice atom can receive in a head-on collision is large and is given by

$$E^{\max} = \frac{4M_1 M_2}{(M_1 + M_2)^2} E_0$$

where  $E_0$  is the incident ion energy and  $M_1$  and  $M_2$  are the ion and target atomic masses, respectively. The average primary-knock-on atom (PKA) energy is much smaller than  $E^{\max}$  because the random distribution of trajectories in the solid makes large impact parameters much more likely than small ones. Therefore average PKA energies are on the order of a few keV. The following discussion therefore focusses on the radiation damage of few keV PKA iron atoms in an iron target in order to illustrate the nature of radiation damage.

#### B. The Structure of Radiation Damage

The damage caused by the collision cascade of one primary knock-on atom (PKA) with an energy of 1 keV (i.e. one iron lattice atom suddenly given 1 keV of energy) can be estimated from the modified theory of Kinchin and Pease (Kinchin and Pease, 1955). They suggested that the number of Frenkel defects  $n_D$  (1 defect = 1 interstitial + 1 vacancy) created by one PKA with energy  $E_p$  can be expressed as

$$n_D = \frac{0.8 E_p}{2E_D} \quad (3.1)$$

where  $E_D$  is the minimum energy for a displacement. For a 1000 eV recoil in Fe ( $E_D = 30$  eV) (Erginsoy et al., 1964)  $n_D$  equals 13. In an important work, Erginsoy et al. performed a computer study by means of Monte Carlo techniques of low energy knock-ons in iron at 0°K where no defect annealing occurs and found that the number of defects created could be well described by equation (3.1) for  $E_p$  energies of  $\leq 1500$  eV (Erginsoy et al., 1965).

Another consequence of collision cascades is that they can lead to a dynamic separation of the vacancy and its associated interstitial which is very much greater than that for random collisions at the same energy. Accordingly, computer studies of Erginsoy et al. (Erginsoy et al., 1964 and 1965) have

shown that the displacement-spike (damage due to one primary knock-on) has a non-uniform spatial distribution of damage. The vacancy population is higher than the interstitial in the central part of the cascade, but the reverse is found in the annular volume surrounding the central vacancy rich region. Beeler et al. (Beeler, 1964 and 1969) found that on the average, the structure of damage for a 1 keV primary knock-on is a vacancy concentration of 3 atomic %, with monovacancies (isolated vacancies) comprising about 35% of the total vacancy population, divacancies 20%, and clusters of three or more vacancies 45%. About 3% of the vacancies are contained in clusters of more than ten vacancies. More than 95% of the interstitial atoms are mono-interstitials and the remainder di-interstitials. Following the work of Beeler, Doran performed a similar study for PKA's between 5 and 20 keV and found that the damage consisted mainly of isolated interstitial clusters and vacancy clusters (Doran, 1970).

### C. Annealing of Damage

In iron considerable annealing of damage takes place at room temperature. Johnson (Johnson, 1964) performed computer simulations of defects in an iron lattice and found the migration energies of the defects to be 0.68 eV for a monovacancy, 0.66 eV for a divacancy, 0.33 eV for a monointerstitial, and 0.18 eV for a di-interstitial. At room temperature the vacancies are considered immobile, while the interstitials are mobile. Clusters of three or more vacancies or interstitials are considered to be immobile. Hence, the annealing takes place when interstitials find vacancies. There is always residual damage after annealing is completed since some of the mobile interstitials may cluster and become immobile (higher migration energy) or travel to dislocations, grain boundaries or the sample surface which act as interstitial sinks. This leads to some net residual vacancy concentration. At elevated temperatures the migration of interstitials and vacancies is faster and annealing more complete. The activation (migration) energy for motion  $E_m$  associated with each defect gives roughly the mean time  $\tau$ , for one jump using the formula,

$$kT = 0.026 \text{ eV (at 300 K)}$$

$$\tau = \tau_0 e^{\frac{E_m}{kT}} \quad \tau_0 \approx 10^{-13} \text{ s.} \quad (3.2)$$

Beeler (1964) studied annealing in the damage spike during 25 jumps per existing mobile interstitial, and found that 50% of all mobile interstitials were removed within these 25 jumps. Since the possible vacancies for the remainder of the interstitials to combine with is reduced, the number of jumps needed to completely anneal out the interstitials is much larger than 25. Doran (1970) has used computer simulation to calculate displacement spike annealing at room temperature for a PKA energy of 5 to 20 keV in iron using the migration energies of Johnson. Doran's studies found that allowing only interstitials to be mobile, annealing was completed after 500 jumps per interstitial, and that about 70% of the damage was removed. Many interstitials remained as immobile clusters of three or more interstitials. Upon allowing a small monovacancy mobility, annealing was complete after 6000 interstitial jumps and 1260 vacancy jumps, and about 95% of the damage was removed, the remainder being immobile vacancy clusters. This would be likely to characterize the implantation damage at low doses and for implantation at room temperature. As the dose increases, the individual collision cascades overlap and every atom in the implanted region is eventually displaced and moved to another lattice or defect position. At high doses, a dynamic balance is set up where as many frenkel pairs are annihilated as are created and saturation of the radiation damage occurs.

### D. Damage at High Dose

Expressions for the total amount of energy deposited in displacement collisions (atomic collisions) per ion, per unit length,  $S_n$ , is given in a later section. In Figure (3.2)  $S_n$  is plotted for 150 keV Fe ions implanted into an Fe substrate. The depth distribution of implanted iron ions is also shown which has a Gaussian shape and is characterized by the mean range  $R_p$  and standard deviation of the range  $\Delta R_p$ . Note that the maximum in the damage distribution occurs at a shallower depth than  $R_p$ . The

number of displacements vs depth can be obtained with the modified Kinchin and Pease (1955) expression,

$$n_D(x) = \frac{0.8 S_n(x)}{2 E_D} \quad (3.3)$$

and the total number of displacements in the implanted volume is

$$n_D = \frac{0.8}{2 E_D} \int S_n(x) dx.$$

A commonly used unit of damage is displacements per atom (DPA). A unit of 1 DPA means that on the average, every atom in the affected volume has been displaced from its equilibrium lattice site once. The dependence of DPA vs depth is obtained by dividing equation (3.3), the number of displaced atoms per unit length, by the atomic density  $N$  (atoms/cm<sup>3</sup>) or;

$$DPA(x) = \frac{0.8 S_n(x)}{2 E_D N} \phi \quad (3.4)$$

where  $\phi$  is the ion dose in units of atoms/cm<sup>2</sup>. For ion masses  $M_1 \geq 20$  and for energies of 10 to 400 keV, the displacement damage profile in Figure (3.2) is quite typical so that an estimate of DPA for these ion/target combinations can be made by assuming a uniform damage profile to a depth  $R_p$  and by using  $S_n(x=0)$  as the total energy expended in displacement collisions. Then the DPA in the implanted region is simply

$$DPA \cong \frac{0.8 S_n(x=0)}{2 E_D N} \phi \quad (3.5)$$

For the ions and energies relevant to ion implantation, calculations using equation (3.5) indicate that a damage dose of 1 DPA occurs in the dose range of  $10^{14}$  (for mass 150) to  $10^{16}$  (mass 8) atoms/cm<sup>2</sup>. Typical doses for implantation of metals are  $10^{17}$ /cm<sup>2</sup> or greater. Hence each atom in the implanted volume is displaced tens to hundreds of times and the individual collision cascade volumes overlap. For self ion implantation (e.g. Fe into Fe), transmission electron micrographs show a high density of dislocation tangles, vacancy clusters, and vacancy and interstitial loops as contrasted with low dose ( $< 1$  DPA) where individual vacancy clusters are observed that are produced in a single collision cascade. The excess vacancy concentrations from individual cascades coalesce into these defect structures as the dose increases. It has often been observed that the highly ion damaged layer resembles a surface that has undergone severe cold work, and by analogy, the surface should be in a state of compression. This is certainly true if the implanted ion has a larger atomic size than the substrate.

#### E. Final Site of Implanted Ions

The computer simulation work of Erginsoy et al. (1965) predicts that for low energy PKA's in iron the primary always ends up in a substitutional site via a replacement collision with the associated interstitial several sites away, and the vacancy at a first, second, or third nearest neighbor site. Dautreppe (Dautreppe, 1971) has reviewed the question of the final site of the implant and found that experiment and theory suggest the findings of Erginsoy et al. are correct as long as  $M_1 > M_2$ . There are expectations such as the cases of Xe (Feldman and Murnick, 1971) and Pb (Feldman et al., 1971) in iron. In general, each case of  $M_1$  in any target should be examined individually to be certain of the final site of the implant.

There are a number of papers that report lattice-site location of implanted ions in metals (Vanden, 1980; Borders and Poate, 1976; Sood, 1978). Borders and Poate state that for concentrations less than or equal to 1 at %, substitutional and interstitial solutions have been observed for implantation into Be, Fe, Ni and Cu, and at concentrations greater than 10 at %, both metastable solid solutions



and amorphous alloys have been formed in Fe, Ni and Cu. The substitutional fraction tends to increase with increasing atomic number of implanted ions (Borders and Poate, 1976). For example, it was found that B implanted into Ni occupies interstitial sites and Sn implanted into nickel is located at substitutional sites with a high probability (>60%).

Light ions such as H, He, B, C, N, and O usually reside at interstitial sites in the lattice unless compound formation changes the phase or structure of the target. This can occur at high doses when the implanted ion concentration exceeds  $\approx 10$  at. %.

## F. Phase Formation

A very useful picture to represent the temporal dependence of a collision cascade has recently been proposed by Johnson et. al. to explain the phenomenon of ion mixing (Johnson et al., 1985). We use this model to introduce the factors influencing phase formation because of the strong similarity between ion mixing of bi-layer and multilayer metallic samples and high dose ion implantation. In the latter, ion mixing processes are occurring when the impurity concentration becomes greater than  $\sim 10$  at. % because subsequent implanted atoms ion mix the previously implanted atom concentration.

The time evolution of a system undergoing ion mixing may be divided into two regimes. The prompt regime (PR) is the time from the initial interaction to when thermal equilibrium is reestablished within the metal ( $t = 0$  to  $\sim 10^{-9}$ s). Longer times are called the delayed regime (DR) where nonequilibrium concentrations of defects may exist which can continue to migrate in the delayed regime ( $t > 10^{-9}$ s) as earlier described by the calculations of Doran and Beeler. Figure (3.3) illustrates the various regimes. Following the work of Johnson et al. (1985), the prompt regime may be further broken down into two sub-regimes. The time required for the ion and secondary ions in the collision cascade to lose most of their energy is defined as the ballistic regime and occurs in the approximate time regime from the initial interaction to  $10^{-13}$  seconds. The time required for the kinetic energy to be shared equally among the atoms in the volume of the cascade where a thermal equilibrium is established is defined as the thermalizing regime and occurs in the approximate time regime of  $10^{-13}$  to  $10^{-9}$  seconds. The majority of atomic mixing occurs in the ballistic regime and in the initial stages of the thermalizing regime where high local equilibrium temperatures (perhaps even melting) can cause diffusional mixing over distances on the order of the cascade volume. The amount of mixing that occurs in the ballistic regime, 0 to  $10^{-13}$  seconds, depends to first order upon the mass and atomic charge of the ion, the energy of the ion, and the atomic masses and atomic charges of the two metals involved. Mixing in the thermalizing regime in the time span of  $10^{-13}$  to  $10^{-11}$  seconds can be influenced by thermodynamics as has been shown by Cheng et al. (Cheng et al., 1985). Heats of mixing play a role in determining the rate constant for mixing kinetics which proceeds as ion dose to the 1/2 power.

Most of the mixing of A atoms with B atoms and therefore the establishment of the atomic concentrations occurs in the ballistic regime and the thermalizing regime from time 0 to  $10^{-11}$  seconds. Phase formation occurs in the thermalizing regime in the time span of  $10^{-11}$  to  $10^{-9}$  seconds where the average energy of the atoms in the cascade goes from 1 eV to thermal equilibrium values. Any phases which form must arise from diffusionless transformations or from near epitaxial growth on existing  $\alpha$ -solution or  $\beta$ -solution surfaces. This rapid quench rate rules out the formation of phases with complex structures. For compositions where  $\alpha$ - and  $\beta$ -solutions are unstable to melting or amorphization, amorphous phases are formed.

In the phase formation time regime of  $10^{-11}$  to  $10^{-9}$  seconds nucleation theory of solid-solid or liquid-solid transformations can be used to rationalize the influence of thermodynamic driving forces on the phases which form. Figure (3.4) is a temperature-time to transformation plot illustrating the kinetics of a solid-solid phase transformation upon cooling from the equilibration temperature  $T_{eq}$ . At temperatures near  $T_{eq}$ , the rate of formation of the new phase is controlled by nucleation and epitaxial growth. As the temperature drops, diffusion of atoms to the phase interfaces controls the rate of phase

formation. The lower curve shows that for a linear temperature drop with time at a slow cooling rate, the temperature passes through a region where growth of the phase is allowed and complete transformation to the new phase occurs. For the faster cooling rate, the region of formation of the new phase is completely bypassed and metastable or amorphous phases are likely to be produced. For the phase formation region in Figure (3.3) the temperature drops by  $10^3$  to  $10^4$  K in  $10^{-10}$  to  $10^{-11}$  seconds so that the effective quench rate is on the order of  $10^{14}$  K/s. This is much faster than melt-quenching techniques ( $10^7$ – $10^9$  K/s). The primary differences between quenching in a cascade and melt quenching is that cascade quenching occurs in the solid state, is accompanied by a high density of defects, and is faster. Further approach to equilibrium can occur in the delayed regime because the presence of a high density of defects that can assist in atomic transport. Thus, precipitation and segregation that began in the phase formation regime can continue in the delayed regime. Formation or ripening of phases in the regime is controlled by the mobility of defects and defect complexes and therefore differs widely among materials.

Interstitial and substitutional metastable solid solutions are frequently observed in ion implanted surfaces. Molybdenum which has negligible solubility in Al, can be formed in continuous metastable solid solution in Al up to 20 at.% concentration (Benson, 1984). Nickel-Boron, Fe-B and Fe-P amorphous alloys prepared by melt quenching are also readily formed by implantation of the metalloid into the metal (Grant, 1981). The ability to form unique metastable and amorphous alloys is one of the most attractive features of ion implantation processing. Studies cited earlier in the chapter (Table 2.5) indicate that metastable surface alloys possess interesting and useful properties for tribological and corrosion applications.

## IV. ION BEAM PROCESSING

### A. Introduction

Once it is decided that the implantation of a certain ion is required to treat a part, questions arise such as what is the correct ion dose and energy? What incident angle of the ion beam should be used to implant facets or curved surfaces on the workpiece? How is the workpiece cooled and mounted in the vacuum chamber?.... and so on. This section organizes answers to these and other questions into manageable elements and is designed to allow the reader to make informed estimates of the ion beam parameters that should be used for proper treatment of a workpiece. These considerations for choosing ion beam parameters are similar to those used by ion implantation vendors. By being familiar with the principles and terminology, it should facilitate discussions with vendors and allow the materials engineer to double-check the implantation conditions that vendors recommend.

### B. Ion Range Parameters

#### i. General Features of Range Distributions

The most frequently asked question about ion implantation is "what is the depth of the implanted layer"? This section discusses the factors determining the ion range and range distribution and includes a table from which the ion range can be conveniently estimated for many ion/target combinations.

The depth of penetration (ion range)  $R_p$  varies between about 5 nm and 1  $\mu$ m for the ion/target combinations of interest, with 50 nm being rather typical. Penetration occurs by means of momentum expenditure rather than by thermal diffusion into the lattice. Therefore, the ion range is small compared to the thickness of diffusion coatings (carburization, nitriding, etc.). Figure (4.1) is a plot of the calculated projected range  $R_p$  and standard deviation of the projected range  $\Delta R_p$  (also called straggling) of nitrogen in iron versus the incident nitrogen ion energy. As shown in the insert, the range distribution of implanted ions is well represented by a Gaussian curve at low doses. Figure (4.2) shows the calculated dependence of the ion range distribution on initial ion energy for iron incident on an iron substrate (Butler, 1981). The implantation doses are equal for all four cases. As the energy increases

the ion range  $R_p$  increases, the width of the distribution  $\Delta R_p$  increases, and the peak concentration decreases. Consequently, the dose for the 200 keV implant would have to increase in order to maintain the same peak concentration as for lower energy implants. This general behavior applies to all ion/target combinations. Two additional trends are worth noting. For a given substrate,  $R_p$  decreases as the atomic number of the ion increases; for a given ion,  $R_p$  also decreases as the atomic number of the substrate increases. The latter trend depends upon the substrate density and significant departures from this rule are possible in regions of the periodic table where the density of the elements changes rapidly.

A Gaussian shape for the profile arises from the statistical nature of the stopping process wherein the ion loses energy in collisions with both electrons and atoms in the solid. Only a small amount of energy is exchanged per collision with electrons because of the small electron mass. A much larger amount of energy per collision is transferred in collisions with the more massive atoms in the solid but the absolute value of the average energy per atomic collision is still much less than the incident ion energy. Ion implantation is done at ion energies where the sum of all the energy lost in collisions with electrons and the sum of all the energy lost in collisions with atoms are of the same order-of-magnitude. The details of the energy transfer of ions in solids is a large subject (Butler, 1981; Borders, 1980) and beyond the scope of this chapter. For our purposes it is sufficient to note that the Gaussian shape of the concentration profile for implanted atoms derives from the statistical distribution of possible energy losses in random and independent collisions with electrons and atoms in the solid as the ion slows down. Because hundreds to thousands of collisions typically occur before the ion comes to rest, statistical principles may be applied to the problem. Indeed, calculations of ion range parameters are often called range statistics.

## ii. Ion Range Tables for Elemental Targets

A number of tables (Johnson, 1970; Gibbons, 1985), graphs (Smith, 1977; Winterbon, 1985), and computer codes (Manning, 1974; Biersack, 1980; Biersack, 1983; Manning, 1984) may be found in the literature which predict the range parameters of ions in solids. We have included in this section another range table which differs from those previously published in several ways. The entries in Table (4.1) were calculated using a modified version of the code E-DEP-1 (Manning, 1974; Manning, 1984). The modifications are, i) improved estimates for the atomic collision cross section (Wilson, 1977) and, ii) a semi-empirical adjustment of the electronic collision cross-sections (Land, 1978). With these modifications, which apply to all ions in the table heavier than boron, the code is the most accurate available for a Boltzmann transport approach to range calculations. Even with these modifications the tabulated values are accurate only to  $\pm 15\%$  in  $R_p$  and  $\pm 20\%$  in  $\Delta R_p$ . Relative values between different ions in a substrate or different ion energies should be considerably more accurate. The tables are simplified and more concise than previous tables because i) ions and substrates of interest for metal implantations are emphasized, ii) only two or three significant figures are included, iii) only five ion energies (10, 50, 100, 200 and 400 keV) per ion/target combination are included because linear interpolation between the energies is accurate to a few percent which is much better than the errors in the absolute value, and iv) the values of  $R_p$  and  $\Delta R_p$  are given in nm rather than the usual  $\text{mg}/\text{cm}^2$ . Seventeen ions and Seventeen substrates are included in Table (4.1). The usual nomenclature to define the atomic numbers and atomic weights is as follows:  $Z_1$ ,  $M_1$  are the atomic number and the atomic weight of the ion, respectively; and  $Z_2$  and  $M_2$  are the atomic number and atomic weight of the target, respectively.

For ions other than those in the Table (4.1), linear interpolation for  $R_p$  and  $\Delta R_p$  using the atomic number  $Z_1$  of the ions is accurate to better than 4%. For targets other than those in the table, one must first convert the appropriate table entries to  $\text{mg}/\text{cm}^2$  by multiplying by the density of the targets, perform the linear interpolation with the  $\text{mg}/\text{cm}^2$  values using the atomic numbers, and then reconvert the answer to nm by dividing by the density of the elemental target of interest.

TABLE 4-1: ION RANGE,  $R_p$ , AND STRAGGLING ( $\Delta R_p$ ) IN UNITS OF HANDBOOKS FOR SELECTED ELEMENTAL TARGETS

TABLE 1

ION (REV)	9.01	Be	24.31	26.98	28.09	47.9	52.0	55.85	58.7	63.54	97.59	97.91	107.9	118.7	157.3	180.9	195.1	274.0
			$M_{12}$	$A_{13}$	$S_{14}$	$T_{22}$	$Cr_{24}$	$Fe_{26}$	$Ni_{28}$	$Cu_{29}$	$Mo_{42}$	$Mo_{41}$	$R_{47}$	$Sm_{60}$	$Cd_{64}$	$La_{73}$	$Pt_{78}$	$U_{83}$
$^4He$	10	106(23)	142(58)	96(42)	109(49)	69(42)	44(27)	41(25)	36(23)	37(23)	67(40)	44	38	58	60	30	28	54
	50	376(39)	603(121)	414(88)	478(106)	325(98)	209(67)	196(64)	174(63)	182(65)	320(129)	222(102)	191(96)	290(150)	297(167)	144(78)	116(62)	293(144)
	100	596(43)	1020(144)	704(105)	822(128)	582(123)	378(85)	354(84)	323(81)	334(86)	612(168)	423(138)	348(132)	542(211)	580(260)	294(162)	237(119)	524(273)
	200	913(66)	1650(161)	1150(117)	1340(144)	984(143)	644(100)	612(100)	560(97)	582(103)	1070(203)	760(172)	671(167)	1030(248)	1110(344)	561(192)	456(164)	1020(381)
$^7Li$	10	42(15)	57(26)	39(18)	44(21)	29(18)	19(12)	17(12)	15(11)	16(12)	29(20)	20	17	27	28	14	12	27
	50	207(39)	279(60)	190(57)	217(68)	141(57)	90(38)	83(37)	73(34)	77(36)	138(69)	92(53)	78(49)	119(77)	122(76)	61(30)	48(29)	106(65)
	100	371(48)	527(115)	340(82)	413(98)	274(86)	175(57)	163(56)	144(51)	151(55)	273(106)	182(83)	154(73)	232(122)	242(145)	120(74)	96(55)	214(128)
	200	531(55)	938(149)	643(107)	742(129)	504(116)	326(79)	305(77)	271(72)	285(78)	517(150)	352(119)	304(113)	462(179)	479(218)	239(118)	190(98)	427(229)
	400	1010(40)	1580(179)	1080(129)	1260(156)	882(144)	573(99)	539(98)	481(91)	509(99)	930(193)	645(158)	564(151)	863(241)	912(302)	459(166)	368(139)	829(327)
$^{11}B$	10	30(9.4)	44(19)	29(13)	34(15)	22(13)	15(8.9)	14(8.7)	13(8.1)	13(8.1)	24(17)	16(11)	14	21	22	12	9.5	21
	50	125(21)	197(55)	127(36)	146(43)	95(35)	64(26)	60(25)	54(24)	59(27)	101(47)	63(32)	54(31)	84(48)	82(50)	43(24)	35(21)	77(47)
	100	212(29)	344(80)	230(49)	267(59)	174(49)	121(37)	113(36)	103(35)	112(40)	191(70)	117(46)	109(49)	158(70)	151(73)	79(43)	64(38)	142(82)
	200	352(40)	629(97)	397(62)	463(76)	308(64)	217(50)	205(49)	188(48)	207(55)	351(96)	212(63)	203(69)	288(97)	273(101)	164(60)	135(54)	293(116)
	400	553(30)	1040(115)	654(73)	766(90)	518(78)	372(61)	353(61)	329(61)	364(70)	614(121)	371(79)	343(89)	512(125)	488(129)	263(79)	225(73)	477(154)
$^{12}C$	10	27(9.1)	40(18)	27(12)	31(14)	20(12)	14(8.2)	13(8.0)	11(7.4)	12(8.3)	22(15)	14(9.8)	13	20	21	11	8.8	20
	50	119(23)	182(54)	117(35)	135(42)	88(34)	59(25)	55(23)	50(23)	53(26)	92(46)	58(31)	53(32)	77(47)	74(50)	39(25)	32(20)	83(52)
	100	212(29)	344(80)	230(49)	267(59)	174(49)	121(37)	113(36)	103(35)	112(40)	191(70)	117(46)	109(49)	158(70)	151(73)	79(43)	64(38)	142(82)
	200	352(40)	629(97)	397(62)	463(76)	308(64)	217(50)	205(49)	188(48)	207(55)	351(96)	212(63)	203(69)	288(97)	273(101)	164(60)	135(54)	293(116)
	400	553(30)	1040(115)	654(73)	766(90)	518(78)	372(61)	353(61)	329(61)	364(70)	614(121)	371(79)	343(89)	512(125)	488(129)	263(79)	225(73)	477(154)
$^{14}N$	10	25(8.7)	36(18)	24(12)	28(14)	19(11)	13(7.6)	12(7.4)	11(6.9)	11(7.7)	20(14)	14(9.9)	12	18	19	10	8.3	19
	50	114(26)	169(54)	109(35)	126(41)	81(33)	55(24)	51(23)	46(22)	49(25)	86(44)	54(30)	49(31)	71(45)	71(49)	37(24)	30(19)	66(42)
	100	211(34)	327(81)	209(53)	240(63)	156(52)	104(38)	99(37)	90(35)	97(40)	167(71)	103(47)	94(49)	136(71)	132(75)	68(43)	56(36)	122(78)
	200	348(42)	608(115)	382(73)	443(88)	290(74)	202(56)	189(55)	173(53)	189(61)	320(104)	194(59)	182(74)	260(105)	247(109)	129(64)	108(57)	233(123)
	400	607(47)	1070(147)	643(92)	772(112)	514(96)	366(75)	345(75)	318(73)	352(85)	591(145)	354(94)	342(104)	482(147)	456(151)	242(90)	202(82)	435(175)
$^{16}O$	10	17(5.5)	26(12)	17(8.2)	20(9.4)	14(7.8)	9.3(5.4)	8.8(5.2)	7.9(4.9)	8.4(5.3)	15(9.9)	10(7.5)	9.4	14(10)	15	8.8	8.1	15
	50	73(19)	105(42)	70(28)	80(32)	54(24)	36(17)	33(16)	30(15)	32(16)	57(30)	37(21)	34(21)	50(32)	52(37)	27(19)	22(15)	48(33)
	100	141(30)	207(71)	137(46)	156(54)	104(39)	69(28)	65(27)	58(25)	62(27)	110(50)	70(37)	65(34)	94(52)	94(58)	48(32)	39(20)	87(40)
	200	243(42)	408(109)	266(70)	304(82)	201(61)	135(44)	127(43)	115(41)	124(46)	224(66)	135(54)	123(56)	181(64)	178(62)	92(52)	75(45)	164(100)
	400	464(53)	773(150)	499(95)	572(112)	379(89)	260(66)	257(64)	228(63)	244(72)	422(128)	258(85)	234(88)	349(130)	339(140)	176(81)	145(71)	314(155)
$^{17}Ar$	10	16(4.7)	23(10)	16(7.2)	18(8.5)	13(6.9)	8.5(4.8)	8.0(4.7)	7.3(4.3)	7.7(4.7)	14(8.9)	9.7(6.5)	8.7(6.1)	13(9.6)	14	7.5	6.1	14
	50	62(16)	90(35)	60(24)	69(28)	47(21)	31(15)	29(14)	26(13)	28(14)	50(26)	33(18)	30(18)	45(28)	46(32)	24(11)	19(14)	44(31)
	100	117(25)	175(40)	115(40)	132(46)	89(34)	59(24)	55(23)	49(22)	53(24)	95(43)	61(30)	55(29)	82(45)	83(51)	43(29)	35(24)	77(55)
	200	218(36)	340(95)	223(62)	255(72)	170(53)	114(36)	108(37)	97(35)	105(39)	184(71)	116(49)	104(76)	150(73)	135(80)	68(45)	55(39)	143(87)
	400	386(46)	649(135)	420(88)	481(101)	323(78)	221(58)	208(51)	189(54)	205(61)	358(111)	222(75)	204(76)	290(114)	259(124)	131(62)	125(62)	273(136)
$^{20}Ca$	10	14(3.7)	20(8.1)	14(6.7)	16(6.7)	11(5.5)	7.2(3.8)	6.8(3.7)	6.2(3.4)	6.5(3.8)	12(7.1)	8.4(5.3)	7.5(5.2)	12(8.0)	13	6.5(5.2)	5.3(4.4)	12(9.8)
	50	48(12)	67(28)	45(18)	52(20)	35(16)	23(11)	22(11)	20(9.9)	21(11)	38(20)	26(14)	23(14)	35(21)	37(24)	19(13)	16(11)	35(23)
	100	89(21)	124(45)	81(30)	95(35)	64(27)	42(18)	40(18)	36(17)	38(18)	69(34)	46(23)	41(22)	62(33)	65(30)	33(21)	27(18)	61(43)
	200	170(33)	241(79)	160(52)	182(61)	122(47)	81(32)	76(31)	68(29)	73(32)	131(57)	85(38)	77(36)	115(55)	118(62)	61(35)	49(30)	109(67)
	400	318(49)	477(130)	312(85)	355(99)	238(75)	159(54)	150(52)	134(48)	145(54)	258(95)	165(81)	149(61)	222(92)	223(102)	115(57)	94(45)	206(118)

ENERGY 100 (keV)	9.01 Be <sub>9</sub>	24.31 Mg <sub>12</sub>	26.98 Al <sub>13</sub>	28.09 Si <sub>14</sub>	47.9 Ti <sub>22</sub>	52.0 Cr <sub>24</sub>	55.85 Fe <sub>26</sub>	58.7 Ni <sub>28</sub>	63.55 Cu <sub>29</sub>	92.59 Ge <sub>32</sub>	92.91 Mo <sub>41</sub>	107.9 Ag <sub>47</sub>	110.7 Sn <sub>50</sub>	157.3 Cd <sub>64</sub>	180.4 La <sub>73</sub>	195.1 Pt <sub>78</sub>	209.0 Bi <sub>83</sub>
10	14(3.4)	20(7.9)	13(5.5)	16(6.5)	11(5.4)	7.1(3.7)	6.7(3.6)	6.0(3.3)	6.4(3.6)	12(6.9)	8.2(5.2)	7.4(5.1)	11(7.9)	12	6.4(5.1)	5.2(4.1)	12(9.5)
50	47(12)	55(25)	44(17)	50(20)	34(16)	22(11)	21(10)	19(9.5)	20(10)	37(20)	25(14)	22(13)	34(21)	36(24)	19(13)	15(11)	34(25)
100	88(21)	119(64)	91(34)	61(27)	61(27)	40(18)	38(18)	34(16)	34(16)	65(33)	44(23)	39(22)	59(32)	62(37)	32(21)	26(18)	54(41)
200	168(35)	230(78)	153(51)	174(61)	174(61)	77(32)	72(31)	64(29)	69(31)	124(57)	82(38)	73(37)	110(55)	110(55)	50(34)	47(29)	105(65)
400	324(54)	462(135)	303(89)	344(103)	229(79)	153(55)	143(54)	128(50)	138(55)	246(98)	158(63)	143(61)	213(91)	214(101)	110(56)	90(48)	197(108)
10	14(3.4)	19(7.4)	13(5.5)	15(6.1)	10(5.1)	6.7(3.5)	6.4(3.4)	5.8(3.1)	6.1(3.4)	11(6.5)	7.8(4.9)	7.0(4.8)	11(7.5)	12(8.9)	6.1(5.0)	5.0(4.2)	11(9.7)
50	45(11)	60(22)	40(15)	46(18)	31(14)	21(9.8)	19(9.5)	17(8.7)	18(9.6)	34(18)	23(13)	21(13)	32(19)	34(22)	17(12)	14(10)	32(24)
100	81(19)	107(39)	72(27)	82(31)	55(25)	36(17)	34(16)	30(15)	32(16)	59(30)	40(21)	36(20)	52(31)	52(31)	29(19)	23(17)	54(39)
200	155(34)	204(72)	137(49)	156(56)	104(43)	68(30)	64(29)	57(26)	61(29)	110(53)	73(36)	65(34)	99(52)	102(56)	52(31)	43(26)	95(60)
400	304(56)	413(130)	273(86)	310(100)	205(76)	135(53)	127(51)	113(47)	122(52)	218(93)	141(61)	127(59)	190(88)	193(94)	99(52)	80(44)	178(100)
10	14(3.4)	19(7.4)	13(5.5)	15(6.1)	9.9(4.6)	6.5(3.1)	6.1(3.0)	5.5(2.8)	5.8(3.0)	11(6.5)	7.5(4.4)	6.7(4.2)	10(6.7)	11(8.0)	5.9(4.5)	4.8(3.8)	11(8.8)
50	42(8.9)	55(19)	37(13)	43(15)	29(12)	19(8.4)	18(8.2)	16(7.5)	17(8.2)	31(15)	21(11)	19(11)	29(17)	31(20)	16(11)	13(9.3)	30(21)
100	72(15)	96(32)	64(22)	73(26)	49(21)	32(14)	30(13)	27(12)	29(13)	52(25)	36(18)	32(17)	48(27)	52(31)	27(17)	22(14)	49(33)
200	133(27)	175(57)	117(39)	134(46)	88(36)	58(24)	54(24)	48(21)	52(24)	94(44)	63(31)	56(29)	86(45)	90(50)	44(27)	34(23)	84(52)
400	252(45)	341(104)	226(71)	257(82)	170(64)	112(44)	105(42)	93(39)	100(43)	180(78)	119(53)	106(51)	161(77)	167(83)	86(45)	69(38)	155(85)
10	14(2.7)	18(6.0)	12(4.2)	14(4.9)	9.5(4.1)	6.2(2.8)	5.9(2.7)	5.3(2.5)	5.5(2.7)	10(5.1)	7.1(3.9)	6.4(3.7)	9.7(5.9)	11(7.1)	5.5(3.9)	4.5(3.3)	10(7.7)
50	38(7.4)	51(16)	34(11)	39(13)	26(11)	17(7.2)	16(7.0)	14(6.4)	15(6.5)	28(13)	19(9.8)	17(9.4)	24(15)	26(17)	15(9.5)	12(8.0)	27(19)
100	64(12)	85(26)	57(18)	65(21)	43(7.7)	28(12)	26(11)	24(10)	25(11)	46(21)	31(15)	28(14)	40(21)	43(25)	22(14)	18(11)	41(26)
200	113(21)	149(46)	100(31)	114(36)	75(29)	49(20)	46(19)	41(17)	44(19)	79(35)	54(25)	48(24)	73(37)	77(42)	40(23)	32(19)	73(44)
400	206(34)	278(81)	185(56)	210(64)	139(51)	91(35)	85(33)	76(31)	81(34)	146(62)	96(43)	87(41)	132(63)	138(69)	71(37)	58(31)	130(71)
10	14(2.7)	18(6.0)	12(4.2)	14(4.9)	9.5(4.1)	6.2(2.8)	5.9(2.7)	5.3(2.5)	5.5(2.7)	10(5.1)	7.1(3.9)	6.4(3.7)	9.7(5.9)	11(7.1)	5.5(3.9)	4.5(3.3)	10(7.7)
50	38(7.4)	51(16)	34(11)	39(13)	26(11)	17(7.2)	16(7.0)	14(6.4)	15(6.5)	27(12)	18(9.2)	16(8.7)	25(14)	27(16)	14(8.9)	11(7.6)	26(17)
100	64(12)	82(24)	55(17)	63(20)	43(16)	27(11)	25(10)	22(9.4)	24(10)	43(19)	30(14)	26(14)	40(21)	43(25)	22(14)	18(11)	41(26)
200	110(20)	141(41)	94(28)	108(33)	70(26)	46(18)	43(17)	38(16)	40(17)	73(32)	50(23)	44(22)	67(34)	72(39)	37(21)	30(18)	68(41)
400	200(34)	258(74)	171(51)	195(59)	127(46)	83(31)	77(30)	69(28)	73(30)	132(56)	89(40)	79(37)	120(58)	127(64)	65(35)	53(29)	119(67)
10	14(2.6)	19(5.5)	13(3.8)	15(4.5)	9.4(3.7)	6.1(2.5)	5.8(2.4)	5.2(2.3)	5.4(2.4)	9.8(4.6)	6.9(3.5)	6.1(3.3)	9.4(5.2)	10(6.3)	5.3(3.5)	4.3(2.9)	9.3(6.8)
50	38(6.6)	50(14)	33(10)	38(11)	25(9.2)	16(6.2)	15(5.1)	14(5.5)	14(6.0)	26(11)	18(8.6)	16(8.1)	24(13)	26(15)	14(8.3)	11(7.0)	25(16)
100	62(10)	80(22)	53(15)	61(18)	39(14)	24(9.8)	24(9.4)	21(8.6)	23(9.4)	41(18)	28(13)	25(12)	38(19)	41(23)	21(13)	17(11)	39(26)
200	104(17)	134(37)	89(28)	102(30)	66(24)	43(16)	40(15)	36(14)	38(15)	68(29)	47(21)	41(20)	63(31)	68(36)	35(20)	28(16)	64(34)
400	185(29)	238(65)	159(45)	181(52)	117(41)	76(28)	71(27)	63(24)	67(27)	121(50)	81(36)	72(34)	110(52)	117(59)	60(32)	49(27)	110(61)
10	15(2.3)	19(5.1)	13(3.5)	15(4.1)	9.4(3.3)	6.1(2.3)	5.7(2.2)	5.1(2.0)	5.4(2.2)	9.7(4.1)	6.7(3.0)	5.9(3.0)	9.1(4.7)	9.8(5.6)	5.1(3.1)	4.1(2.6)	9.4(6.0)
50	38(5.7)	49(12)	33(8.6)	37(10)	24(8.1)	15(5.5)	14(5.1)	13(4.6)	14(5.3)	24(10)	17(7.2)	15(7.1)	23(11)	25(13)	13(7.3)	10(6.1)	23(14)
100	59(8.8)	74(19)	51(13)	58(15)	37(12)	24(8.4)	22(8.1)	20(7.4)	21(8.0)	38(15)	25(11)	23(11)	35(17)	38(20)	20(11)	16(9.1)	34(21)
200	96(14)	123(30)	82(21)	94(25)	60(20)	39(13)	36(13)	32(12)	34(13)	61(24)	40(16)	37(17)	56(26)	60(30)	31(17)	25(18)	57(32)
400	162(23)	209(51)	139(35)	159(41)	101(33)	66(22)	61(21)	55(20)	58(21)	104(40)	66(27)	62(27)	95(42)	100(49)	52(26)	42(22)	95(51)
10	16(2.4)	20(5.0)	13(3.5)	15(4.1)	9.4(3.2)	6.2(2.2)	5.8(2.1)	5.2(1.9)	5.4(2.1)	9.8(4.0)	6.7(3.0)	5.9(3.0)	9.0(4.4)	9.8(5.3)	5.0(2.9)	4.1(2.4)	9.3(5.7)
50	40(5.7)	50(12)	33(8.6)	38(9.8)	24(7.8)	15(5.2)	14(5.1)	13(4.6)	14(5.3)	24(10)	17(7.2)	15(7.1)	23(11)	25(13)	13(7.3)	10(6.1)	23(14)
100	61(8.6)	77(18)	51(13)	59(15)	37(12)	24(8.4)	22(8.1)	20(7.4)	21(8.0)	38(15)	25(11)	23(11)	35(17)	38(20)	20(11)	16(9.1)	34(21)
200	98(14)	122(29)	81(20)	93(23)	58(18)	38(12)	35(12)	32(12)	34(13)	61(24)	40(16)	37(17)	56(26)	60(30)	31(17)	25(18)	57(32)
400	163(22)	203(47)	135(33)	154(38)	97(30)	63(20)	58(20)	52(18)	55(19)	98(37)	66(27)	62(27)	95(42)	100(49)	52(26)	42(22)	95(51)
10	17(2.3)	21(4.8)	14(3.3)	16(3.9)	9.8(3.1)	6.3(2.1)	5.9(2.0)	5.3(1.9)	5.5(2.0)	9.9(3.8)	6.7(3.0)	5.9(3.0)	9.0(4.2)	9.7(5.0)	5.0(2.7)	4.0(2.3)	9.2(5.3)
50	41(5.5)	51(11)	34(7.9)	39(9.3)	24(7.4)	15(5.0)	14(4.8)	13(4.7)	14(4.9)	24(10)	17(7.2)	15(7.1)	23(11)	25(13)	13(7.3)	10(6.1)	23(14)
100	62(8.2)	77(17)	51(12)	59(14)	36(11)	23(7.4)	22(7.1)	20(6.5)	20(7.1)	36(13)	25(9.9)	22(9.3)	33(15)	35(17)	19(10)	15(7.9)	33(18)
200	97(13)	121(24)	80(18)	92(21)	57(17)	37(11)	34(11)	30(10)	32(11)	57(21)	34(14)	31(14)	51(22)	55(26)	28(14)	23(12)	52(27)
400	159(20)	196(43)	130(30)	149(35)	93(27)	60(18)	56(18)	49(16)	52(18)	93(33)	62(24)	55(23)	83(35)	88(41)	43(22)	37(19)	83(43)

In many cases, it isn't necessary to interpolate for ions or targets. If the ion is not in Table (4.1) and only differs from the nearest ion in the table by 1 or 2 atomic numbers, then the values of the nearest ion will be adequate. Similarly, for targets that are not in the table and which only differ from the nearest table entry by 1 or 2 atomic units, adequate values for  $R_p$  and  $\Delta R_p$  may be obtained by scaling with the mass densities of the unknown target and the table entry. For example,  $R_p$  for 100 keV Cr in Ni obtained from the table entries for Fe is,

$$R_p (Cr \rightarrow Ni) = R_p (Cr \rightarrow Fe) \times \frac{\rho_{Fe}}{\rho_{Ni}} = 38 \times \frac{7.86}{8.9} = 34 \text{ nm}$$

which agrees with the table entry for 100 keV Cr into Ni. For target atomic numbers  $Z_T \gtrsim 60$  this method can be used with good accuracy for any target between table entries. For example, for 100 keV Zr ions we have  $R_p (Zr \rightarrow Ta) = R_p (Zr \rightarrow Pt) \times 21.4/16.6 = 24 \text{ nm}$  which is the same value as the table entry for Zr  $\rightarrow$  Ta. A list of the densities of the elements is given in Table (4.2) for this purpose. For steels, the table values for iron can be used, scaled by the density of steel (e.g.,  $(R_p \text{ or } \Delta R_p)_{steel} = \rho_{Fe}/\rho_{steel} \times (R_p \text{ or } \Delta R_p)_{Fe}$ ). The densities of steels range from 7.5 to 8.9 g/cm<sup>3</sup>.

Frequently, the target is an alloy composed of two or more elements. There are two methods to derive  $R_p$  and  $\Delta R_p$  for these cases. An approximate method is to find  $R_p$  and  $\Delta R_p$  for the major constituent and scale the results by the ratio of the density of the element in the table and the density of the alloy. For alloys or compounds where there is a large fraction of elements of largely different masses a different approximate approach is required. The table entries for  $R_p$  and  $\Delta R_p$  must be converted to mg/cm<sup>2</sup> by multiplying by the respective densities and a weighted sum of the mg/cm<sup>2</sup> values performed. The result is reconverted to nm by dividing by the density of the alloy or compound. For an alloy or compound  $A_x B_y$  where  $x+y=1$ , we have,

$$R_p^{alloy} = \left[ x \frac{R_p^A}{\rho_A} + y \frac{R_p^B}{\rho_B} \right] \rho_{alloy} \quad (4.1)$$

and in general,

$$R_p^{alloy} = \left[ \sum_i x_i \frac{R_p^i}{\rho_i} \right] \rho_{alloy} \quad (4.2)$$

$$\Delta R_p^{alloy} = \left[ \sum_i x_i \frac{\Delta R_p^i}{\rho_i} \right] \rho_{alloy} \quad (4.3)$$

This estimate of  $R_p$  and  $\Delta R_p$  for alloys is an approximation because, strictly speaking, the calculation should be performed by including different stopping powers of the constituents of the alloy in the Boltzman transport equations to arrive at  $R_p$  and  $\Delta R_p$ . However, the approximation works well enough to provide a 1st order estimate of  $R_p$  and  $\Delta R_p$ . For determination for compounds like stoichiometric oxides, carbides, nitrides, etc., publications mentioned earlier must be consulted because Table (4.1) includes entries only for solid elemental targets.

Some values of  $\Delta R_p$  are not listed in the table. This arises because the numerical calculation of Johnson and Gibbons range parameters on which the code E-DEP-1 is based is unstable for these cases and no solution exists.

Occupying only two book pages, this is the most compact range table in existence and allows convenient estimates of  $R_p$  and  $\Delta R_p$  for most ion/target combinations. Little precision is lost in the interpolations and approximations necessary for arriving at values for ions and targets not included in the table because the starting values of the range parameters are only accurate to 15%.

Table 4.2: Selected Properties of the Elements

Atomic Number ( $z_2$ )	Symbol	$U_o$ (ev)	N ( $\times 10^{22}$ atoms/cm <sup>3</sup> )	$\rho$ (g/cm <sup>3</sup> )	Atomic Number ( $z_2$ )	Symbol	$U_o$ (ev)	N ( $\times 10^{22}$ atoms/cm <sup>3</sup> )	$\rho$ (g/cm)
3	Li	1.67	4.60	0.53	49	In	2.51	3.83	7.31
4	Be	3.35	12.4	1.85	45	Sn	3.12	3.70	7.30
5	B	6.01	13.0	2.34	51	Sb	2.73	3.30	6.68
6	C	7.40	13.1	2.62	52	Te	2.03	2.94	6.24
11	Na	1.12	2.54	0.97	53	I	1.10	2.33	4.92
12	Mg	1.51	4.31	1.74	55	Cs	0.81	0.85	1.87
13	Al	3.41	6.03	2.70	56	Ba	1.84	1.53	3.50
14	Si	4.67	5.00	2.33	57	La	--	2.90	6.70
15	P	3.43	3.54	1.82	58	Ce	4.36	2.91	6.78
16	S	2.86	3.89	2.07	59	Pr	--	2.89	6.77
19	K	0.93	1.32	0.86	60	Nd	--	2.92	7.00
20	Ca	1.84	2.33	1.55	62	Sm	2.14	3.02	7.54
21	Sc	3.90	4.02	3.00	63	Eu	--	2.08	5.26
22	Ti	4.85	5.66	4.50	64	Gd	--	3.02	7.89
23	V	5.32	6.86	5.80	65	Tb	--	3.13	8.27
24	Cr	4.11	8.33	7.19	66	Dy	--	3.16	8.54
25	Mn	2.93	8.14	7.43	67	Ho	--	3.21	8.80
26	Fe	4.29	8.48	7.86	68	Er	3.28	3.26	9.05
27	Co	4.43	9.09	8.90	69	Tm	--	3.33	9.33
28	Ni	4.44	9.13	8.90	70	Yb	1.57	2.43	6.98
29	Cu	3.49	8.49	8.96	71	Lu	--	3.39	9.84
30	Zn	1.35	6.58	7.14	72	Hf	6.40	4.42	13.1
31	Ga	2.83	5.10	5.91	73	Ta	8.08	5.52	16.6
32	Ge	3.87	4.41	5.32	74	W	8.88	6.32	19.3
33	As	3.12	4.60	5.72	75	Re	8.00	6.79	21.0
34	Se	2.35	3.66	4.80	76	Os	8.13	7.09	22.4
35	Br	1.16	2.35	3.12	77	Ir	6.92	7.05	22.5
37	Rb	0.85	1.08	1.53	78	Pt	5.84	6.61	21.4
38	Sr	1.69	1.79	2.60	79	Au	3.80	5.90	19.3
39	Y	4.39	3.05	4.50	80	Hg	0.63	4.06	13.5
40	Zr	6.29	4.28	6.49	81	Tl	1.88	3.49	11.9
41	Nb	7.45	5.54	8.55	82	Pb	2.01	3.31	11.4
42	Mo	6.80	6.40	10.2	83	Bi	2.17	2.82	9.80
44	Ru	6.72	7.27	12.2	90	Th	5.94	3.04	11.7
45	Rh	5.75	7.26	12.4	92	U	5.45	4.78	18.9
46	Pd	3.89	6.79	12.0					
47	Ag	2.94	5.86	10.5					
48	Cd	1.15	4.63	8.65					

+ For N in units of atoms/ $\text{\AA}^3$ , multiply by  $10^{-24} \text{ cm}^3/\text{\AA}^3$ 

N = atomic density

 $U_o$  = sublimation energy

### C. Sputtering

When an ion strikes and penetrates the surface of a solid, some of the near surface target atoms receive enough kinetic energy in the collision cascade to overcome the surface binding energy and are ejected from the surface. The parameter used to describe this phenomenon is the sputtering coefficient,  $S$ , defined as the ratio of the number of atoms ejected from the surface per incident ion. For example, values of  $S$  for 100 keV ions incident on iron vary from 0.05 for He ions to 13 for Bi ions. For high dose implantation, the sputtering coefficient is the major parameter determining the depth distribution and surface concentration of implanted ions. For this reason sputtering theory is presented in enough detail to enable the estimation of  $S$  for any ion/target combination.

The most useful theory is that of P. Sigmund (Sigmund, 1969) who proposed the following expression for the sputtering coefficient,

$$S = \frac{0.042 \alpha S_n (eV/\text{\AA})}{U_o (eV) N (\text{atoms}/\text{\AA})} \frac{1}{(\cos \theta)^{5/3}} \quad (4.4)$$

where  $\alpha$  is a dimensionless constant and is a function of  $M_2/M_1$ ,  $S_n$  is the atomic stopping power (also called nuclear stopping) computed from the equations which follow and contains the dependence of  $S$  on  $Z_1$ ,  $Z_2$ ,  $M_1$ ,  $M_2$  and ion energy  $E$ .  $U_o$  is the surface binding energy,  $N$  is the atomic density, and  $\theta$  is the angle of incidence to the surface normal. For convenience, values of  $U_o$  and  $N$  are given in Table (4.2). Tabulated values of  $N$  have to be multiplied by  $10^{-24} \text{cm}^3/\text{\AA}$  to be in the correct units for the equation. Entries for  $U_o$ , taken from the Handbook of Chemistry and Physics (CRC, Cleveland 1966), are the "Heats of Formation of Gaseous atoms from Elements in their Standard States" converted from Kcal/mole to eV. Because of approximations used in the theory, equation (4.4) is also restricted to values of  $M_1 \gtrsim 14$  where the electronic stopping power is a small fraction of the nuclear stopping power, to values of  $M_2/M_1 < 4$ , and to values of  $\theta \gtrsim 70^\circ$ . In addition, for  $M_1 < M_2$ ,  $S \propto (\cos \theta)^{-1}$ . For  $M_1 \gtrsim 14$ , equation (4.4) overestimates the sputtering coefficient. For ion masses greater than  $M_1 \approx 120$  incident on substrates with masses greater than  $M_2 \approx 120$ , thermal spike effects can sometimes increase  $S$ , but the amount of the increase is always less than 1.8 and it is usually much smaller.

The parameter  $\alpha$  can be converted to an approximate analytical form for convenient calculation of  $S$  with the expression (Matsunami et al. 1984),

$$\alpha = 0.08 + 0.164 \left( \frac{M_2}{M_1} \right)^{0.4} + 0.0145 \left( \frac{M_2}{M_1} \right)^{1.29} \quad (4.5)$$

Substituting this expression into equation (4.4) for  $S$ , and noting all the restrictions we have

$$S = \frac{0.042 S_n \left[ 0.08 + 0.164 \left( \frac{M_2}{M_1} \right)^{0.4} + 0.145 \left( \frac{M_2}{M_1} \right)^{1.29} \right]}{U_o N (\cos \theta)^{5/3}} \quad \left\{ \begin{array}{l} \frac{M_2}{M_1} < 4 \\ M_1 \gtrsim 14 \\ \theta \gtrsim 70^\circ \end{array} \right. \quad (4.6)$$

Equation (4.6) indicates that  $S$  is directly proportional to the atomic stopping power  $S_n$  and inversely proportional to the sublimation energy  $U_o$ . The angular dependence is fairly strong indicating that  $S$  increases by factors of 1.3 and 3.2 at  $30^\circ$  and  $60^\circ$ , respectively. The restriction that  $S$  is not valid for  $M_1 \gtrsim 14$  is not a serious problem because sputtering coefficients are small for light ions and the range distribution is well represented by the Gaussian distribution. The atomic stopping power  $S_n$  is computed from the semi-empirical expression of Wilson et al. (Wilson, 1977) because it is more accurate than that originally used by Sigmund and because of convenient formulation. The atomic stopping is given by:



$$S_n \text{ (eV/\AA)} = \frac{51.1 Z_1 Z_2 M_1 \rho \text{ (g/cm}^3\text{)}}{M_2 (M_1 + M_2) Z_a} S_r \quad (4.7)$$

$$Z_a = \left( Z_1^{1/2} + Z_2^{1/2} \right)^{2/3} \quad (4.8)$$

$$S_r = \frac{0.5626 \ln(1.1776 \epsilon)}{1.1776 \epsilon - (1.1776 \epsilon)^{-0.6268}} \quad (4.9)$$

$$\epsilon = \frac{32.58 M_2 E \text{ (keV)}}{Z_1 Z_2 (M_1 + M_2) Z_a} \quad (4.10)$$

Epsilon is the reduced energy common to LSS range theory (Lindhart, 1963) but with the Firsov screening length  $Z_a$  instead of the Thomas-Fermi screening length as prescribed by Wilson et al. (Wilson, 1977).  $S_r$  is the Wilson, Haggmark and Biersack atomic stopping power in reduced energy units and equation (4.7) converts  $S_n$  into units of eV/\AA. The expression for  $S_n$  is a simple algebraic formula containing  $Z_1$ ,  $Z_2$ ,  $M_1$ ,  $M_2$ , the ion energy  $E$  and mass density  $\rho$  of the substrate and is easily programmed in Fortran or Basic for the purpose of computing  $S$ . The values of  $S_n$  are valid for all ion/target combinations listed in the range table for energies between 10 and 400 keV.

Equation (4.6) predicts the trends of sputtering data in the literature quite well but is likely to miss the absolute value of  $S$  by as much as a factor of two. Reynolds and Sigmund (Reynolds (1985), ; Sigmund, 1969; Sigmund, 1981) have discussed the reasons for these discrepancies, none of which are easily estimated. The two largest effects are ion channeling in textured polycrystalline targets and surface contamination during sputtering, both of which tend to reduce  $S$ .

Calculated values of  $S$  for the Group IVB and VB elements such as Ti, Nb and Ta on Fe are usually larger than experimental measurements. There is a well known experimental problem in measuring the sputtering coefficient for these elements because of their reactive nature. Impurities chemisorbed on the surface can greatly influence the sublimation energy which in general causes the experiment to yield a value smaller than is calculated. For most other elements, the values for the sputtering coefficient  $S$  should predict the correct value to within 25%. The best choice of  $S$  would be an experimental value from the literature. Two excellent sources of values of  $S$  are references Behrisch, 1981 and Matsunami, 1984. If  $S$  is known for a given system but for a different energy, then the experimental values can be used to calibrate equation (4.6) from which accurate values of  $S$  can be obtained for other ion energies.

#### D. Atomic Fraction of Implanted Ions

To plan a particular experiment or treatment of a part, it is important to be able to predict the concentration profile of the implanted impurity atoms. This section discusses the factors determining the profile in low dose and high dose regimes and gives expressions, tables and graphs to allow predictions of the impurity profile to be made.

##### i. Low Dose Concentration For All Ion Masses

For low ion doses at normal incidence where the amount of material sputtered from the surface  $S\phi/N$  is  $\leq 0.15R_p$ , the ions are completely retained in the surface and the concentration profile can be approximated by a Gaussian distribution characterized by a centroid,  $R_p$ , a standard deviation,  $\Delta R_p$ , and a peak atomic density,  $N_p$ , given as,

$$N_p \left( \frac{\text{atm}}{\text{cm}^3} \right) = \frac{1}{\sqrt{2\pi}} \frac{\phi}{\Delta R_p} \cong \frac{0.4 \phi}{\Delta R_p} . \quad (4.11)$$

Assuming the target density doesn't change, the peak atomic fraction,  $C_p$ , is,

$$C_p = \frac{N_p}{N} , \quad (4.12)$$

where  $N$  is the atomic density of the substrate given as  $\rho A/M_2$  where  $A$  is Avogadro's number =  $6.02 \times 10^{23}$  atoms/mole. For non-normal angles of incidence,  $R_p$  is shortened by a  $\cos \theta$  factor so that,

$$R_p(\theta) = R_p \cos \theta . \quad (4.13)$$

Because lateral straggling spreads the implanted ion distribution in a direction parallel with the surface by about the same magnitude as the straggling  $\Delta R_p$ , it is a good 1st-order approximation to assume that  $\Delta R_p$  is independent of the angle of incidence. This will be discussed in more detail in the following section.

The ion dose a sample receives is always given with respect to an area parallel to the sample surface but the measurement of dose is always with respect to an area normal to the beam direction. Therefore, for non-normal angles of incidence the measured dose has to be increased by a  $\cos \theta$  factor to achieve the required dose in the area projected on the sample surface, or,

$$\phi_{\perp \text{ to beam}}^{\text{meas.}} = \frac{\phi_{\parallel \text{ to surface}}^{\text{implanted}}}{\cos \theta} . \quad (4.14)$$

If  $\phi$  measured stays constant, then substitution of equation (4.11) and (4.14) into equation (4.12) shows that  $C_p(\theta) = C_p(\theta=0) \cos \theta$ . This is the angular dependence of the dose in the low dose limit for a stationary cylinder when the ion beam floods the entire diameter.

Most implantation machines have a minimum energy at which they can operate. Implanting at a non-normal angle of incidence is a means of obtaining shallow implants when it is desired. However, the sputtering coefficient increases sharply with angle so that care must be taken that the condition that the amount of material sputtered away be  $\gtrsim 0.15 R_p$  still applies.

## ii. High Dose Concentration for Light Ions: $M_1 \gtrsim 20$

The sputtering coefficient for light ions (especially H, He, Li, B, C, N and O) is generally small enough ( $\lesssim 1$ ) so that the sputtering can be ignored. The concentration of implanted impurity atoms builds up in a Gaussian shape at depth  $R_p$  without appreciable erosion of the surface. In this case, the atomic fraction at the peak of the Gaussian distribution can be obtained by modifying equation (4.12) to include the sum of the target density  $N$  and the implanted atom density, or

$$C_p = \frac{N_p}{N_p + N} . \quad (4.15)$$

## iii. High Dose Concentration for Heavy Ions: $M_1 \gtrsim 20$

The final concentration profile in the high dose regime is the result of many processes occurring simultaneously. These processes include sputtering, preferential sputtering of the surface fraction of one element when the target is an alloy or a compound, radiation enhanced diffusion, radiation induced segregation, ion mixing, compound formation, surface reactions with gas atoms in the vacuum, as well as other processes. A comprehensive discussion of these effects is beyond the scope of this chapter (Borders, 1980). Furthermore, there is no comprehensive theory that can predict concentration profiles

for high dose implantations because of the interdependence of the complicated effects listed above. It would still be useful however, to devise a means to give a 0th order approximation to the profile at high doses so that a reasonable estimate of ion dose can be made prior to treatment. To that end, this section describes 0th and 1st order approximation methods to predict the saturation dose, the surface concentration of implanted atoms and the concentration profile at saturation dose. It should be noted that a computer code is under development that includes some of the effects listed above (Davisson, 1986) but even this code still doesn't include all 1st order effects.

For high ion doses (e.g.  $\gtrsim 10^{17}$  ions/cm<sup>2</sup>) removal of material from the surface by sputtering uncovers some of the previously implanted ions which are also sputtered from the surface. As a result, less than 100% of the implanted ions are retained. This effect causes large deviations from the Gaussian-like behavior of the implanted atom profile. A 0th order approximation for the surface concentration at saturation,  $C_{surf}$ , the implantation profile,  $C(x)$ , and the saturation dose,  $\phi_s$ , are, respectively (Liau, 1980)

$$C_{surf} = \frac{1}{S} = \frac{N_A}{N_A + N_B} \quad (4.16)$$

$$C(x) = C_{surf} \quad 0 \leq x \leq R_p \quad (4.17)$$

$$= 0 \quad x > R_p$$

$$\phi_s = \frac{R_p N}{S} \quad (4.18)$$

where  $N_A$  is the atomic fraction of implanted atoms and  $N_B$  is the atomic fraction of substrate atoms.

Note that the surface concentration is the same as the bulk concentration and the bulk concentration is approximated as constant from the surface to the depth  $R_p$ . Saturation is assumed to occur when the amount of material sputtered from the surface reaches the depth  $R_p$ , e.g.  $S\phi_s = R_p N$ , from which equation (4.18) obtains. Figure (4.3) illustrates the concentration profile obtained for these assumptions.

A different approach has been reported by Grabowski et al. and Manning (Grabowski, 1984; Manning, 1985) who calculated the actual concentration profiles under certain simplifying assumptions. From that work the product of the sputter coefficient and atomic fraction is plotted versus a dimensionless depth variable  $x/(\sqrt{2}\Delta R_p)$  for the cases of  $R_p = 6\sqrt{2}\Delta R_p$  and  $R_p = \sqrt{2}\Delta R_p$  in Figure (4.4). These curves assume the implanted ions occupy no volume, the sputter coefficient and  $R_p$  remain constant during implantation, and that no diffusion processes occur. The latter condition could be realized if the implantation were performed at a temperature of 0° K. These assumptions are quite restrictive but provide adequate first order estimates of the effects of sputtering on the concentration profile. Sputter saturation is said to occur when the concentration profile no longer changes with increasing ion dose because equilibrium is achieved between the number of ions being implanted and the number of implanted ions being removed. This occurs for  $\omega = 3/2$  in Figure (4.4a) and  $\omega = 3$  in Figure (4.4b) where  $\omega$  is the amount of material removed relative to  $R_p$  and is given by

$$\omega = \frac{S\phi}{R_p N} \quad (4.19)$$

In Figure (4.4a) it is clear that for  $\omega = 1/6$  the median of the profile is only slightly shifted toward the surface by sputtering. As the dose is increased the profile fills in toward the surface and at saturation the concentration profile approaches that of equation (4.17). In figure (4.4b), which represents a more

realistic case for transition elements implanted into transition metals, there is no well defined plateau in the profile for any value of  $\omega$ . The value of  $\omega$  for the 0th order estimate for saturation dose in equation (4.19) is 1.0, whereas the saturation values of  $\omega$  in Figures (4.4a) and (4.4b) are 1.5 and 3.0, respectively. This shows that the 0th order calculation tends to underestimate the  $\omega_s$ .

From a family of curves (Manning, 1985) such as those in Figures (4.4a) and (4.4b) we have developed the curves in Figure (4.5) for  $\omega$  at the saturation dose versus  $R_p/(\sqrt{2}\Delta R_p)$  to allow the calculation of  $\omega_s$  for any arbitrary ion/target combination. Because the surface concentration approaches the saturation value asymptotically, we include the saturation dose which achieves 90% of the surface concentration at the true saturation dose. Otherwise, considerably more ions have to be implanted for the limited benefit of increasing the surface concentration by 10%. A curve for  $\omega$  at 99% saturation dose is also shown. Particularly at small values of  $R_p/(\sqrt{2}\Delta R_p)$  the dose required to achieve 99% saturation is substantially higher than for 90% saturation. Also shown in Figure (4.5) is the parameter  $\beta$  which is a correction factor applied to the calculation of  $C_{surf}$ . It arises from the fact that for small values of  $R_p/(\sqrt{2}\Delta R_p)$ , some of the Gaussian profile resides outside the surface of the sample and is assumed in the theory to be lost by reflection. Given  $R_p$ ,  $\Delta R_p$  and  $S$  one can find  $\phi_s$  (90%) by solving equation (4.19) after first finding  $\omega$  (90%) from Figure (4.5); e.g.,

$$\phi_s(90\%) = \frac{R_p \omega(90\%) N}{S} \quad (4.20)$$

The concentration or atomic fraction at the surface for the  $\phi_s(90\%)$  and  $\phi_s(99\%)$  are,

$$C_{surf}(90\%) = \frac{0.9\beta}{S} \quad (4.21)$$

$$C_{surf}(99\%) = \frac{0.99\beta}{S} \quad (4.22)$$

where it is assumed that there is no change in the substrate density. The entire profile is approximated by equation (4.17) but with the atomic fraction equal to  $C(x) = C_{surf}$  in equation (4.21) or (4.22).

The plot of  $\omega$  versus  $R_p/\sqrt{2}\Delta R_p$  in Figure (4.5) may be accurately represented by the analytical form,

$$\omega(90\%) = 0.96 \left[ 1 + \frac{1}{R_p/\sqrt{2}\Delta R_p} \right] \quad (4.23)$$

$$\omega(99\%) = 1 + \frac{1.64}{R_p/\sqrt{2}\Delta R_p} \quad (4.24)$$

Substituting equation (4.23) and (4.24) into equation (4.20) then gives  $\phi_s$  for normal incidence;

$$\phi_s(90\%) = 0.96 \frac{N}{S} \left[ R_p + \sqrt{2}\Delta R_p \right] \quad (4.25)$$

$$\phi_s(99\%) = \frac{N}{S} \left[ R_p + 1.64\sqrt{2}\Delta R_p \right] \quad (4.26)$$

For non-normal angles of incidence one must begin with the corrected values of  $R_p$ ,  $\Delta R_p$  and  $S$ . Substituting the correct angular dependence into equation (4.20) we have,

$$\phi_s(\theta) = \frac{R_p(\theta=0) \omega_s(\theta)}{S(\theta=0)} (\cos \theta)^{8.3} \quad (4.27)$$

The surface atomic fraction of implanted atoms becomes,

$$C_{surf}(90\%) = \frac{0.9\beta}{S(\theta=0)} (\cos \theta)^{5/3}. \quad (4.28)$$

These expressions show that as the angle of incidence increases, the saturation dose and surface atomic fraction decrease by the factors  $(\cos \theta)^{8/3}$  and  $(\cos \theta)^{5/3}$ , respectively, and the depth of the implanted layer decreases by the factor  $\cos \theta$ .

The angular dependence  $(\cos \theta)^{8/3}$  for  $\phi_s$  in equation (4.27) is a good 1st order approximation but it is not explicitly correct because  $\phi_s$  also depends upon  $\omega$ . Inserting equation (4.23) into equation (4.27) yields,

$$\phi_s(90\%) = 0.96 \frac{N}{S} (\cos \theta)^{5/3} \left[ R_p \cos \theta + \sqrt{2} \Delta R_p \right]. \quad (4.29)$$

Note that only if  $\Delta R_p(\theta) = \Delta R_p \cos \theta$  does the  $(\cos \theta)^{8/3}$  dependence strictly apply which may be shown by factoring  $\cos \theta$  out of the sum in equation (4.29). The correct angular dependence of  $\Delta R_p$  is

$$\Delta R_p(\theta) = \left[ \Delta R_p^2(\theta=0) \cos^2 \theta + \Delta R_{\perp}^2(\theta=0) \sin^2 \theta \right]^{1/2} \quad (4.30)$$

for  $M_1 \gtrsim 20$ ;  $\theta \gtrsim 45^\circ$

where  $\Delta R_{\perp}$  is the lateral straggling. Lateral straggling refers to the fact that ions are displaced by atomic collisions from their initial trajectory so that the final site of the implanted ions has a statistical deviation from a straight line path described by  $\Delta R_{\perp}$ , or straggling in a direction perpendicular to the initial beam direction. Lateral straggling has in general a similar magnitude as  $\Delta R_p$ . If  $\Delta R_{\perp} = \Delta R_p$  then the straggling is isotropic and  $\Delta R_p$  is independent of the angle of incidence. We have computed  $\Delta R_p(\theta)$  from equation (4.30) at an angle of  $45^\circ$  for ions ranging from B to Bi and substrates from Be to Bi in order to assess the magnitude of the angular dependence of  $\Delta R_p$ . The values of  $\Delta R_{\perp}$  were obtained from the code E-DEP-1 and  $\Delta R_p(\theta)$  was evaluated for energies between 10 and 400 keV that are covered in Table (4.1). For ion masses  $M_1 > 20$ ,  $\Delta R_p(\theta)$  deviated from  $\Delta R_p$  by the average of -4%, with the largest deviations being -15% and +12%. For ions with  $M_1 < 20$ , deviations were as high as +40%, with +20% being rather typical. Therefore, equation (4.29) should be quite accurate if we assume that  $\Delta R_p$  is independent of angle for ion masses greater than about 20 and for angles  $\gtrsim 45^\circ$ . The deviations of  $\Delta R_p(\theta)$  from  $\Delta R_p$  rapidly become less as the angle decreases from  $45^\circ$ , and vice-versa. For ion masses less than 20 the sputtering coefficient is frequently small enough that implantation to saturation is not practical so that equation (4.29) wouldn't be applicable in the first place.

As an example, consider the implantation of normally incident Cr ions into Fe at an energy of 90 keV. Interpolating Table (4.1) for 90 keV we have  $R_p = 38 - 0.2 \times (38 - 21) = 35$  nm and  $\Delta R_p = 18 - 0.2 \times (18 - 10) = 16$  nm which compare very well with the actual E-DEP-1 values of 34 and 16 nm, respectively. The sputtering yield has been measured to be  $S = 2.8$  ( $S$  differs from the value computed by equation (4.6) because of texturing of the polycrystalline target) (Reynolds, 1981, 1985). From equation (4.29) we have,

$$\begin{aligned} \phi_s(90\%) &= \frac{0.96}{2.8} \left[ 8.48 \times 10^{22} \text{ cm}^{-3} \right] \left[ 35 + \sqrt{2} 16 \right] \text{ nm} \left[ 10^{-7} \frac{\text{cm}}{\text{nm}} \right] \\ &= 1.7 \times 10^{17} \text{ ions/cm}^2 \end{aligned}$$

and the surface concentration from equation (4.21) and the graph in Figure (4.5) for  $\beta$  is,

$$C_{surf}(90\%) = \frac{0.9 \times 0.99}{2.8} = 0.32.$$

For an angle of incidence of  $45^\circ$ , the saturation dose computed from equation (4.29) becomes

$$\begin{aligned}\phi_s (90\%) &= \frac{0.96}{2.8} \left( 8.48 \times 10^{22} \right) \cos \left( 45^\circ \right)^{5/3} \left[ 35 \cos 45^\circ + \sqrt{2} 16 \right] \left( 10^{-7} \right) \\ &= 7.7 \times 10^{16} \text{ ions/cm}^2\end{aligned}$$

and the surface concentration becomes,

$$C_{surf} (90\%) = \frac{0.9 \times 0.89}{2.8} (\cos 45^\circ)^{5/3} = 0.16$$

where  $\beta$  is now 0.89 because  $\omega = R_p / (\sqrt{2} \Delta R_p)$  is smaller by the fact that the range  $R_p$  is shortened by a  $\cos \theta$  factor.

#### iv. Comparison of Calculated Profiles to Experimental Results

Figure (4.6a) is experimental data for retained dose versus angle of incidence normalized to the retained dose at normal incidence for several ions incident on steel targets and for doses greater than saturation dose (Grabowski, 1984). The retained dose should also to first order follow the  $(\cos \theta)^{5/3}$  dependence. The agreement is good for angles between  $0$  and  $50^\circ$  which indicates that the simple considerations in this section are quite acceptable for making 1st order estimates of  $\phi_s$  and  $C_{surf}$ . Discrepancies can arise in predicting the absolute scale of the  $(\cos \theta)^{5/3}$  dependence as shown in Figure (4.6b) for Ta implantation. At high doses, the retained dose for Ta-implanted 52100 steel is higher than that predicted by the simple theory. The explanation for this arises from two effects. As shown by Grabowski et. al. (Grabowski, 1985), diffusion must be invoked to explain the observed concentration profiles of Ta-implanted iron substrates. Diffusion of Ta into the bulk would tend to reduce the surface concentration and increase the retained dose compared with calculated values. Secondly, it has already been mentioned that group IVB and VB elements will form surface carbides during implantation in high vacuum ( $> 10^{-7}$  Torr) to such an extent that atomic concentrations of C up to 15 at % are not uncommon (Singer, 1984). Our simple theory assumes that the sputtering coefficient doesn't change during implantation. However, carbides in general have a lower sputtering coefficient than the free metal so that  $S$  in equation (4.25) decreases as the carbon content of the surface increases. This effect tends to increase the retained dose and the surface fraction of the implanted element. Figure (4.7) demonstrates this effect for Ta-implanted 52100 steel (Hubler, 1985). Sputter Auger profiles of C and Ta for different doses clearly show that carbon enters the surface during implantation. Therefore, the calculation of  $\phi_s$  and  $C_{surf}$  by means of equations (4.25) and (4.21) should be considered lower limits for the refractory carbide forming elements. Singer (Singer, 1984) and Behrisch (Behrisch, 1981) discuss this problem and point out that many measurements of  $S$  for these elements in the literature are effected by this phenomenon and as a result are factor of 2 to 3 too low.

A definitive experiment demonstrating the reduction in sputtering coefficient with surface absorbed carbon has been performed by Sartwell and Baldwin (1985). Ti was implanted into thin bilayer films of iron on silicon in ultrahigh vacuum ( $10^{-9}$  Torr) or with the chamber backfilled to a partial pressure of  $10^{-5}$  torr with CO. The total amount of Ti retained in the sample and the amount of Fe removed from the film were continuously monitored by means of proton induced X-ray yields. Figure (4.8 a&b) shows the X-ray yields vs dose. It is clear that in the backfill case the sputtering coefficient decreases with respect to the UHV implantation and that more Ti is retained. The sputtering coefficient starts at a value of 3.5 finishes at a value of 1.8. The value calculated from equation (4.6) is 4.1, in reasonable agreement with the UHV measured value. Therefore, the calculated value represents an upper limit for reactive implanted ions.

Comparisons of calculated and experimental values measured by Reynolds et al. (Reynolds, 1981) of  $\phi_s$  and  $C_{surf}$  are given in Table (4.3). The experimental points were generated by monitoring the optical signal from Cr on the surface of iron as a function of dose during Cr implantation. The optical signal from Cr was initially zero, increased rapidly, and then saturated as the dose increased indicating that  $\phi_s$  had been reached. Similar data was produced for Cu implanted into Al. The agreement for  $C_{surf}$  and  $\phi_s (90\%)$  between experiment and the 1st order values is quite good.

Table 4.3 — Experimental and Calculated Values of  $C_{surf}$  and  $\phi_s$  (90%)

	Measurement (Reynolds, 1981)	0th Order (equations 4.16, 4.18)	1st Order (equations 4.21, 4.25)	
$C_{surf}$	0.24	0.28	0.25	
$\phi_s$ (90%)	$1.8 \times 10^{17} cm^2$	$1.1 \times 10^{17}/cm^2$	$1.6 \times 10^{17}/cm^2$	Cu → Al 90 keV
$C_{surf}$	0.33	0.36	0.32	
$\phi_s$ (90%)	$1.7 \times 10^{17}/cm^2$	$1.0 \times 10^{17}/cm^2$	$1.6 \times 10^{17}/cm^2$	Cr → Fe 90 keV

### E. Selected Experimental Range Profiles

Some of the most widely used ions for the implantation of steels are N, Ti and Cr so considerable effort has been expended to determine concentration profiles. Examples of depth profiles for these and other cases are given here in Figures (4.9) through (4.13). In Figure (4.9) the nitrogen concentration profile departs from Gaussian-like behavior for doses greater than  $2 \times 10^{17}/cm^2$  at 40 keV. In this case, it is unclear as to whether radiation enhanced diffusion or sputtering causes the increase in surface concentration of nitrogen and it is probably caused partly by both. For Nb implanted into Fe (Figure 4.12) there is no difference in the profile for doses of  $2.5$  and  $4.0 \times 10^{17}/cm^2$  showing that the equilibrium between implanted ions and sputtered ions was achieved near the dose of  $2.5 \times 10^{17} ion/cm^2$ . The ranges obtained from Table (4.1) are in reasonable agreement with the low dose data in Figures 4.7, 4.9-4.12. The range for 100 keV Be in Ni from Table (4.1) is 1440 Å which is ~35% smaller than the data in Figures (4.13) indicates. This large discrepancy arises because the semi-empirical corrections to electronic stopping power used in the calculation of ranges in the program E-DEP-1 are not available for elements lighter than carbon. An overestimate of the electronic stopping power causes the computed range to be too small. The independence of the shape of the concentration profile with ion dose for light ions that results from a small value of  $S$  is also demonstrated by the data for 100 keV Be in Figure (4.13). Note that the peak position of the profile doesn't change for doses of  $10^{16}$  and  $10^{17} ions/cm^2$ .

### F. Influence of Masking

A common problem to be addressed in processing is the implantation of cylindrical or spherical objects. By masking the samples to allow the beam to impinge only at angles near normal incidence, concentration profiles can be calculated by the simple expression used above. Opening the mask to larger angles or completely flooding the sample makes more efficient use of the ion beam. In this case the depth profiles must be integrated over all angles of incidence. Figure (4.14) is such a calculation for the case of B implanted into Be (Smidt, 1985). Profiles for the same dose are shown for four different masking angles. The sputtering coefficient is very small for this case so most of the differences are caused by range shortening with angle only. More dramatic effects that can occur for larger sputtering coefficients are shown by the data of Singer and Jeffries (Singer, 1984) in Figure (4.15). Profiles of Ti-implanted steel are measured for saturation doses implanted into 52100 steel with 3 different experimental configurations.

## G. Topographical Changes

In general, the larger the sputtering coefficient, the greater the possibility that the surface will be roughened on a microscopic scale during implantation. Examples of roughened surfaces are presented in Figure (4.16) which are surface profiles of AISI M50, CRB7 and 440C steel 3/8" diameter rods after implantation with Ta ions (Hubler). The rods were rotated during treatment and a mask restricted the angles of incidence to  $\pm 30^\circ$ . The region profiled spans unimplanted and implanted material and indicates that, i) 1800 Å of material was removed by sputtering for M50 and CRB7 and 1200 Å for 440C, ii) the surface in the implanted region has been roughened with respect to unimplanted material, especially for CRB7 and 440C. Figure (4.17) presents differential interference contrast photomicrographs of the same rods, additional unimplanted rods, and rods implanted with N ions in the same geometry. N implantation has little effect on surface finish. Mesas have developed on the Ta-implanted rods which result from a faster erosion rate for the iron matrix than for the carbides which form the mesas. The mesas for CRB7 appear as depressions because of a phase reversal of the interference. This roughening effect is minimized by i) confining the beam to near-normal angles of incidence in order to minimize the sputtering coefficient, ii) selecting the minimum ion dose necessary to treat the sample, and iii) by purposely backfilling the target chamber with a hydrocarbon (e.g. CO, CH<sub>4</sub>) in order to produce surface carbide which reduces the sputter coefficient of the matrix (Sartwell and Baldwin, 1985). Only strong carbide-forming substrates and ions are amenable to the latter treatment. Surface roughening is very material dependent as shown by comparing the micrographs in Fig. (4.16) for M50 and CRB7 implanted with Ta ions.

Figure (4.18) compares the surface topography of two 440C steel rods implanted with Ta ions to identical doses, but for one the vacuum was  $1 \times 10^{-6}$  Torr and for the other the target chamber was backfilled to a pressure of  $5 \times 10^{-5}$  torr with CO gas. Note that the amount of material removed decreased by a factor of almost three and the surface retained its initial smoothness in CO backfilled case.

Surfaces can also be smoothed by ion implantation. For example, Pronko et al. (Pronko, 1984) have reported surface smoothing of polished Mo surfaces by Mo ion implantation. Also, removal of very fine final polishing scratches on M50 and 52100 steel is a frequently observed phenomenon.

## H. Workpiece Manipulation

Tools and components of mechanical machinery can have widely varying shapes and complex geometries which present specific problems for ion implantation treatment. Furthermore, beam processing with laser, electron or ion beams is line-of-sight processing which places some limitations on the types of components that can be treated. For example, the internal surfaces of small tubes or holes cannot be ion implanted.

The components to be implanted are described as having planar, cylindrical or spherical surfaces. Planar surfaces are most easily implanted because they frequently require no manipulation in front of the ion beam or only some lateral translation in order to treat the entire area. Cylindrical surfaces are implanted by rotating the piece in front of the ion beam. Long cylindrical objects may be treated by translating the rotating cylinder along the direction of the cylinder axis. Figure (4.19) schematically shows these geometries, including the geometry for treatment of the inner surface of a ring such as a bearing race.

## I. Workpiece Cooling

One of the greatest difficulties in high dose ion implantation processing is the maintenance of low workpiece temperatures. For a beam current of 3 mA at an energy of 100 keV the incident power is 300 watts. This power must be dissipated or the workpiece will be overheated, especially for carbon steels whose tempering temperatures may be as low as 125°C. To address this important problem we refer to the work of Grabowski and Kant (Grabowski, 1983) who have reported methods to remove heat in a vacuum. The following paragraphs summarize their findings.



In a vacuum, heat can be removed by radiation or by conduction through solids to a heat sink. For low doses or large mass objects, the heat capacity of the object can be sufficient to maintain the temperature under a specified limit. Radiative cooling is effective only for high target temperatures ( $\geq 400^\circ\text{C}$ ) or large surface areas, both of which are usually not realizable for high dose ion implantation of metals. Figure (4.20) shows the power radiated per unit surface area as a function of surface temperature for emissivities of 1.0 and 0.2, the latter being a typical value for steels. The dashed lines show that at temperatures of  $500^\circ\text{C}$  and  $200^\circ\text{C}$  the radiated power is  $0.4 \text{ W/cm}^2$  and  $0.05 \text{ W/cm}^2$ , respectively. Thus, for an incident power of 300 Watts a surface area of  $750 \text{ cm}^2$  is required to maintain the temperature at  $500^\circ\text{C}$  by radiation alone. This is an unacceptable temperature rise for many metals and the surface area required to maintain  $500^\circ\text{C}$  implies a part which is near the maximum size that can be conveniently placed in implantation systems. Moreover, the surface area must increase by a factor of 8 in order to maintain the temperature rise to less than  $200^\circ\text{C}$ . Another means to use radiative cooling is to reduce the beam power which can lead to unacceptably long implantation times.

Alternative ways to make use of high beam currents are by conduction through the workpiece to a heat-sink, or by use of the heat capacity of the part as the heat-sink. Grabowski and Kant (Grabowski, 1983) have analyzed the situations of one-dimensional heat flow through a flat plate, a cylinder or a sphere and the results are plotted in Figure (4.21). Radiative cooling is not included in the curves so they do not apply for temperatures  $> 500^\circ\text{C}$ . A dimensionless surface temperature rise  $\theta_s = (T_s - T_o)/(Jl/k)$  is plotted versus dimensionless time  $\tau = \alpha \phi E/l^2 J$ . In these expressions  $T_s$  is the surface temperature,  $T_o$  the initial temperature and  $T_b$  is the temperature either at the back of a plate of thickness  $l$  or at the center of a sphere or cylinder of radius  $l$ .  $T_b$  will be discussed later in relation to the three regimes shown in the figure. The other variables are the incident power density  $J (\text{W/cm}^2)$ , the thermal conductivity  $k (\text{W/(cm-K)})$  the exposure time  $t (\text{s})$ , and the thermal diffusivity  $\alpha (\text{cm}^2/\text{s}) = k/\rho C$  where  $\rho$  is density ( $\text{g/cm}^3$ ) and  $C$  is heat capacity ( $\text{Ws/(g-K)}$ ).  $\phi$  is the ion dose ( $\text{ions/cm}^2$ ) and  $E$  is the ion Energy (Joules/ion). Representative values of  $\alpha$ ,  $k$  and  $C$  are given in Table (4.4) for several materials of interest.

Table 4.4 — Thermal Properties of Selected Materials (from Grabowski and Kant, 1983)

Material	$\alpha$ ( $\text{cm}^2/\text{s}$ )	$k$ ( $\text{W/(cmK)}$ )	$\rho C$ ( $\text{Ws/(cm}^3 \text{ K)}$ )
Cu	1.1	3.9	3.4
Al	0.95	2.3	2.4
Al (2024-T4)	0.50	1.2	2.4
Si	0.53	0.84	1.6
Brass (Cu -30Zn)	0.38	1.2	3.2
Ta	0.24	0.54	2.3
Fe	0.23	0.80	3.5
Fe (0.10C)	0.18	0.65	3.5
Fe (M2 tool steel)	0.058	0.21	3.7
Fe (304 SS)	0.041	0.16	4.0
Ti	0.068	0.16	2.3
Ti (6Al - 4V)	0.026	0.068	2.6
Superalloy (IN 738)	0.035	0.12	3.4

Three different regimes of conduction heat transfer are indicated in Figure (4.2). In regions I and II all deposited energy is retained in the sample. In region III a steady-state condition is reached where heat flow is constant through a plate sample to a heat sink. In region I,  $T_b = T_o$  because the deposited energy has not yet diffused to the boundary of the sample. For cylinders or spheres,  $T_b$  is at the center of the sample. In region II most of the deposited energy is distributed throughout the sample so that  $T_b \approx T_s$ . The transition from region I to either II or III occurs at  $\tau \approx 1$ . For most metal implantations with high current beams,  $\tau$  is greater than 1. For plate samples, expressions for the temperature rise in regions I, II, and III are,

$$I \quad T_s - T_o = \frac{2}{\sqrt{\pi}} \frac{(\phi E)^{1/2}}{\rho C} \left( \frac{J}{\alpha} \right)^{1/2} \quad (4.31)$$

$$II \quad T_s - T_o = \frac{n \phi E}{\rho C l} \quad \begin{array}{l} n = 1 \text{ plate} \\ n = 2 \text{ cylinder} \\ n = 3 \text{ sphere} \end{array} \quad (4.32)$$

$$III \quad T_s - T_o = \frac{Jl}{k} \text{ (ideal heat sink) } . \quad (4.33)$$

In Figure (4.22) the generalized curves of Figure (4.21) are evaluated for the special cases of a tool steel and copper plates for an input power density of  $100 \text{ W/cm}^2$  ( $100 \text{ keV}$ ,  $1 \text{ mA/cm}^2$ ) and a thickness of  $1 \text{ cm}$ . These represent two extreme cases for implantation of metals because steel is a relatively poor conductor of heat whereas copper is a good conductor. In 10 seconds, the copper and steel surface reach temperatures of  $290^\circ\text{C}$  and  $430^\circ\text{C}$ , respectively. For a  $1 \text{ mA/cm}^2$  beam it requires 16 seconds to implant a dose of  $10^{17}/\text{cm}^2$ . Therefore, the steel must be actively cooled in order to maintain the surface temperature below the typical tempering temperatures for carbon steels. Even for the case of conduction to an ideal heat sink, the steel reaches a steady-state value of  $450^\circ\text{C}$ . Therefore, the beam power must be reduced or a duty cycle introduced which lowers the average incident power.

Equation (4.33) for region III implies perfect conduction of heat from the sample to the heat-sink which in practice is rarely achieved in vacuum because temperature drops occur across interfaces where the sample is clamped to the heat-sink. The temperature differential across the interface is expressed as,

$$\Delta T = J/h \quad (4.34)$$

where  $h$  ( $\text{W/cm}^2\text{-K}$ ) is the interface contact conductance. According to Grabowski and Kant (Grabowski, 1983),  $h$  can be maximized by using a pressure contact and by inserting a thin foil of soft high thermal conductivity material at the interface (e.g. Cu, In, Al). Table (4.5) presents values of the heat conductance across interfaces in vacuum for different metal-metal interface configurations measured for a contact pressure of 145 psi. Table (4.5) provides useful guidelines for maximizing the interface contact conductance for most situations that are encountered for implantation of metals.

Hirvonen (1986) has analyzed the situation where a cylinder composed of tool steel is cooled by gripping it at one end over a length equal to 1 diameter, for an incident power density of  $1 \text{ W/cm}^2$ , for a thermal conductivity  $k=0.2 \text{ W/(cm-K)}$ , and for an interface conductance at the heat sunk end equal to  $1 \text{ W/(cm}^2\text{-K)}$ . Figure (4.23) is as plot of the maximum temperature rise of the tip of the tool versus the tool diameter and tool length. By careful interpolation one can predict the maximum temperature rise for tools ranging from 0.01 inches to 10 inches in diameter for lengths between 1 and 10 inches. Examples of the use of equation (4.31-4.34) are given in the final section V.

## J. Examples of Fixtures for Manipulation and Cooling

An example of a rotating water-cooled feed through used to cool and rotate cylindrical geometry samples is shown in Figure (4.24) (Grabowski, 1985a). Proceeding from the top of the feed-through assembly, there is a rotating-seal water jacket with input and output water lines, a gear to attach the motor drive, and a collar around the 4-cm-diameter stainless steel shaft to hold the vertical position of the shaft against the actual vacuum feed-through. The vacuum feed-through is sealed by a ferrofluid to provide vacuum-tight shaft rotation. It is mounted on a welded-type stainless steel bellows with 4" diameter flanges to allow for up to a 30 degree tilt angle of the rotation axis. The bellows and the mounting assembly which secures the entire feed-through are insulated so that charge may be collected

Table 4.5 — Interface Contact Conductance  
(from Grabowski and Kant, 1983)

Interface	$h(W/(cm^2 \cdot K))$
SS/SS	0.04
SS/Al	0.19
SS/Al Foil/SS	> 0.3
SS/Indium/SS	> 0.6
SS/Silver Paint/SS	> 5
<hr/>	
Al/Brass	0.5
Al/Cu	0.9
Al/OF-Cu	1.5
Al/Al	1.6
<hr/>	
Brass/Brass	0.1
Cu/Cu	0.6
OF-Cu/OF-Cu	1.5
<hr/>	
SS: 304 Stainless Steel	Cu: Tough-pitch Cu
Al: 6061, T6 Temper	OF-Cu: Oxygen-free Cu
Brass: Cu-30 Zn	

from the target. Jigs which hold the workpiece are secured to a copper plug in the end of the water cooled feed-through shaft by four screws. A small diameter tube inside the 65-cm-long hollow shaft directs water at the copper plug, so that heat generated by the ion beam conducts through the jig and into the cooled copper plug. Dual O-ring seals in the inner diameter of the ferrofluid vacuum feed-through allow linear translation of the shaft without breaking the vacuum seal.

Flat plate geometry samples can be secured to a water-cooled block of copper or aluminum. Frequently used methods to ensure heat conduction from sample to plate include pressure from a clamping system, silver print (organic carrier with Ag dust in suspension), commercially available heat-sink compounds (i.e. MUNG II, Commonwealth Scientific), and high vacuum fluids (i.e. Santovac 5) with Ag powder in suspension. For batch processing of parts a duty cycle can be introduced by mechanical manipulation in order to lower the average beam power on individual parts. This places less stringent cooling requirements on the fixture that manipulates parts without sacrificing through-put (Smidt and Sartwell, 1985). In high current ion implanters (beam currents  $\geq 1$  mA) space charge blow-up of the ion beam precludes the use of a raster scanned, focussed ion beam so mechanical manipulation or defocussing are required. One way to address the problem is to develop a defocussed ion beam (Armini and Bunker, 1985) which is capable of projecting a 10 mA beam into a 40 cm diameter area with good uniformity of beam density within the diameter. In this scheme, the average beam current density on the samples is reduced to  $10 \mu A/cm^2$ , a value at which the removal of heat from the workpiece is more easily managed. Figure (4.25) is a photograph of this apparatus and Figure (4.26) shows a commercially available non-mass analyzed ion-implanter (Hirvonen, 1984) that uses a low melting point ( $145^\circ C$ ) eutectic metal (60% pb/40% Bi) to both hold tools and act as a heat-sink medium.

#### K. Cleaning of Workpiece

As with all coating techniques, surface cleanliness prior to implantation is essential. In the case of coatings, cleanliness promotes good adhesion of the film to the substrate. There is no adhesion problem with ion implantation, but cleanliness ensures a uniform implantation dose on all areas scanned by

the beam. Since the ions do not penetrate dust particles or oil films that are more than several hundred nanometers in thickness, the areas beneath will not be implanted. Cleanliness and surface finish are most important for corrosion and oxidation applications where unimplanted regions may corrode at rates several orders-of-magnitude faster than implanted material. These weak areas act as initiation sites where corrosion will penetrate deeply or undermine the implanted area. If the surface is pitted prior to implantation such that internal surfaces are present, the ion beam cannot reach these areas and corrosion may proceed unchecked in the pits.

Both cleanliness and surface pits are not as important for wear applications where occasional small unimplanted regions represent only a small fraction of the total area to which the load is applied. However, it is always generally true for ion implantation or thin film coatings that "cleanliness is next to Godliness". The primary culprits to be aware of are oil and grease-based preservative treatments used on many steel parts to keep them from rusting, oil films on cold-rolled sheet, fingerprints and dust particles. It is good practice to clean metal parts with solvents whether or not oil films are known to be present. Methods frequently used are soaking in baths of paint thinner, toluene and high purity methanol or ethanol, in that order. Ultrasonic action improves the cleaning when it is compatible with the part being cleaned (e.g., do not ultrasonically clean Al or Cu because they damage by cavitation). Degreasing in freon vapor is frequently substituted for the paint thinner step.

The best practice is to clean the workpiece immediately prior to performing the implantation and to blow a jet of oil-free air or dry nitrogen over the surface just before insertion into the vacuum chamber to remove dust particles. If this procedure cannot be used then storage of the cleaned workpiece in a desiccating container for long periods or a laminar flow bench for short periods is recommended. Plastic disposable gloves should be used at all times to avoid finger prints. In short, any available means of providing a clean environment throughout the handling of the workpiece should be employed and care should be taken to ensure that the surfaces to be implanted are free from contamination and flaws such as pits.

#### **L. Size Of Workpiece**

The size of a workpiece that may be implanted depends upon the kind of vacuum end-station that is peculiar to each vendor and whether the ion required is a solid or a gas in its elemental form. For ions capable of being formed from a gaseous element, a non-mass analyzed beam may be used which lends itself to the implantation of larger surface areas than do mass analyzed ion beams. However, new implantation machines with mass analysis capable of 10 mA beam current are becoming available so that this distinction is likely to disappear in the near future.

Because of differences in the size of the implantation vacuum chambers employed by different vendors, a useful way to describe the size of workpieces is to give examples of items that have been implanted. A partial list includes: 4-cylinder automobile engine crankshafts (Sioshansi, 1980), 10" diameter (O.D.) bearing races and 7/8" diameter balls (48 balls/batch) (Grabowski, 1985; Popgoshev, 1983), thermo-plastic injection molds and feed screws (Dearnaley, 1983), steel pressing tools and WC punches, dies and drills (Sioshansi, 1985; Dearnaley, 1983; Hirvonen, 1984). Batch processing of a large number of small pieces such as drills is straightforward. Approximate maximum areas for implantation are 12" x 12" for planar geometries and 6" x 30" for cylindrical geometries where 6" is the diameter. The group at the Atomic Energy Research Establishment at Harwell, U.K. has a non-analyzed-beam ion implanter which can treat an area 1 meter by 1 meter (Dearnaley, 1984).

#### **M. Implantation Time and Cost**

The time necessary to implant a sample depends upon the beam current available at the vendor's facility, the maximum allowable temperature for the material, and the sample geometry. The latter determines the beam utilization efficiency. Smidt and Sartwell (Smidt, 1985) have analyzed the costs associated with running a Manufacturing Technology Facility. Table (4.6) is extracted from their work and shows the projected costs of implanting flat and spherical geometries which correspond to the best

and worst case geometries, respectively. It is important to note that these costs are projected for a state-of-the art facility purposely designed for high through-put production runs. The costs of 64cents/cm<sup>2</sup> for spheres and 14cents/cm<sup>2</sup> for flats are realistic estimates for this facility. Much of the implantation work currently conducted is of an experimental nature or involves a limited number of work pieces. The vendor is continually faced with new processing problems involving the fabrication of jigs and masks for new geometries. This necessitates long set up times which would not occur for large scale production runs. Therefore, the cost of implanting work pieces for research or limited numbers of samples is presently 3 to 5 times those quoted in the Table. Accordingly, vendors are presently charging \$300 to \$500 per hour for time that the beam is on the target.

Table 4.6 — Estimate of the operating costs for the Man Tech ion implantation facility (from Smidt and Sartwell, 1985)

	1 shift	2 shifts	3 shifts
Capital investment <sup>d</sup>	\$100K	\$100K	\$100K
Full time operator	\$ 70K	\$175K <sup>d</sup>	\$280K <sup>d</sup>
Management	\$30K	\$60K	\$90K
Utilities, consumables	\$ 25K	\$ 50K	\$ 75K
Maintenance support	\$ 20K	\$ 30K	\$ 40K
	—	—	—
Total annual cost	\$245K	\$415K	\$585K
Hourly cost <sup>b</sup>	\$136/h	\$115/h	\$108/h
Throughput costs <sup>c</sup>			
Balls	\$0.64/cm <sup>2</sup>	\$0.54/cm <sup>2</sup>	\$0.50/cm <sup>2</sup>
Flats	\$0.14/cm <sup>2</sup>	\$0.12/cm <sup>2</sup>	\$0.11/cm <sup>2</sup>

a) \$1M/10 years = \$100K/year.

b) 2000 h shift year at 0.9 available = 1800 h

c)  $2 \times 10^{17}$  ions/cm<sup>2</sup>, 10 mA.

d) Assume time and one half for shift work

To estimate the time for a given sample area we note that it required 16 seconds to implant a dose of  $10^{17}$  ions for a beam current of 1 mA. If the total beam current of the vendor is known, one can find the time to implant the required dose from,

$$t_f (s) = \frac{16 (mA-s)}{10^{17} (ions)} \times \frac{\phi (ions/cm^2)}{I (mA)} \times A (cm^2) \quad (4.35)$$

where  $\phi$  is the required dose,  $I$  is the total beam current available at the vendor's facility, and  $A$  is the total area to be implanted. Following Smidt and Sartwell this number must be divided by two beam utilization factors  $F_t$  and  $F_h$  which have values between 0 and 1. If the total beam current available must be reduced to permit adequate workpiece cooling, then the cooling factor  $F_t$  will be less than 1. Because in most implantations the beam is raster scanned across a beam defining aperture, the beam spends a fraction of time on the apertures and masks rather than on the sample. This factor is highly dependent on the workpiece geometry. To ensure dose uniformity in the implanted area, the beam must sweep entirely off the sample on each side of the aperture. A typical beam spot diameter is 1/2 cm. For an area of 1 cm  $\times$  1 cm, the beam is incident on the mask for as much time as it is on the sample and  $F_h = 0.5$ . For a 5 cm  $\times$  5 cm swept area,  $F_h = 0.83$ . Beam utilization for rotating cylindrical geometry for a single workpiece is similar to plane geometries. However, if several workpieces are to be implanted simultaneously and if masks are required to limit sputtering at large incident angles then a packing factor must be introduced into  $F_h$  to account for the mask areas. For spherical geometries  $F_h$  is on the order of 0.1 to 0.2. Including the beam utilization factor in the equation for implantation time  $t_f$  we have,

$$t_i (s) = \frac{16 (mA-s)}{10^{17} (ions)} \times \frac{\phi (ions/cm^2)}{I (mA)} \times \frac{A (cm^2)}{F_i F_b} \quad (4.36)$$

This section on ion beam processing has covered range statistics, sputtering, heat flow calculations, and time and cost of implantation processing and has included enough detail to allow the reader to plan the processing parameters for any given ion-implantation treatment. As a further aid, the next section presents case studies which use the formulae and tables presented here in order to illustrate the actual calculation of implantation parameters.

## V. DETERMINATION OF IMPLANT PARAMETERS AND QUALITY CONTROL

Let us suppose that implantation of P ions into flat steel specimens and implantation of Ti ions into cylindrically shaped steel specimens is required for a particular application. What is the ion dose required? What power density limit is appropriate to avoid overheating the samples? and so on. This section gives a step-by-step procedure for the calculation of first-order estimates of ion dose, ion energy, beam power, time and cost of implantation, and in so doing, illustrates the use of the formulae given in the previous section.

### A. Flat Geometry Workpiece

The problem at hand is to implant P ions into a stainless steel in planer geometry. The workpiece is  $5\text{cm} \times 5\text{cm} = 25\text{cm}^2$  in area and is 1 cm thick. The vendor has a maximum beam energy of 90 keV and a total beam current of 1 mA available. It is desirable to create an amorphous surface layer which requires a concentration of 20 to 40 atomic % of P. We do not want to overdose the sample because, as we have seen, too much dose can roughen the surface and because too much ion dose unnecessarily raises the cost of the implant. Also, since the material is 440C steel, the temperature during implantation cannot exceed  $150^\circ\text{C}$ .

The procedure is to calculate  $R_p$ ,  $\Delta R_p$ ,  $S$ ,  $\phi_s$  (90%), the beam power required to maintain temperature below  $150^\circ\text{C}$ , and the time and cost of the implantation treatment.

$$\underline{R_p, \Delta R_p, S}$$

Interpolation of Table (4.1) for P ions incident on an Fe target gives,

$$R_p = [55-29] \times 0.8 + 29 = 50 \text{ nm}$$

$$\Delta R_p = [23-14] \times 0.8 + 14 = 21 \text{ nm.}$$

From equations (4.7-4.10) we compute  $S_n = 76 \text{ eV}$ . Substituting entries for Fe of  $U_o = 4.29 \text{ eV}$  and  $N=0.0848 \text{ \AA}^{-3}$  from Table (4.2), and  $M_2 = 56$  and  $M_1 = 31$  into equation (4.6) gives,

$$S = 0.042 \times 76 \times [0.319]/[4.29 \times 0.0848] = 2.8.$$

$$\underline{\phi_s (90\%), C_s (90\%)}$$

Equation (4.25) for the dose to reach 90% of sputter saturation at normal incidence gives,

$$\phi_s (90\%) = 0.96 \times (8.48 \times 10^{22} \text{ atm/cm}^3) \times [50 + \sqrt{2} 21](10^{-7} \text{ cm/nm})/2.8$$

$$= 2.3 \times 10^{17}/\text{cm}^2.$$

Using equation (4.21) for the surface concentration at 90% of sputter saturation yields,

$$C_s(90\%) = 0.9 \times 1/2.8 = 0.32.$$

This concentration is in the range of 20 to 40% P that is required so a dose of  $2.3 \times 10^{17} P/cm^2$  is appropriate. The concentration of P is then approximated by a 32% concentration from the surface to a depth  $R_p = 50$  nm, and 0 for depths greater than 50 nm.

#### Power Limit

The area that the beam will scan is  $25 \text{ cm}^2$ . The total power available is  $90 \text{ keV} \times 1 \text{ mA} = 90$  Watts. Because the beam is scanned off the samples on all sides to achieve uniformity, the beam spends some time off the samples so that the true average power is less than 90 watts. It is also necessary to determine the method of heat sinking the samples. We will assume that they are fastened with a metal powder bearing glue that has good heat conduction properties ( $h=1 \text{ W/cm}^2\text{-K}$ ). Assume that the entire available beam power is incident on the sample or  $90\text{W}/25\text{cm}^2 = 3.6 \text{ W/cm}^2$ . Using equation (4.34) the temperature rise as a result of the interface between the sample and the heat sink is

$$\Delta T = J/h = 3.6 (\text{W/cm}^2)/1 (\text{W/cm}^2\text{-K}) = 3.6 \text{ K}.$$

This is a very acceptable temperature drop across the interface but notice that if the samples were only lightly clamped to the heat sink, the value of  $h$  could be  $< 0.01$  and  $\Delta T$  could be 360K. This shows that the method of heat sinking the sample is extremely important for maintenance of temperature control. Even if the samples are well heat sunk, they may still be overheated because of heat conduction limitations through the sample to the heat sink. In our case the surface temperature at steady state is given by equation (4.33), or

$$\Delta T = 90 (\text{W/cm}^2) \times 1(\text{cm})/0.21(\text{W/cm-K}) = 429 \text{ K}$$

where the thickness of the sample is 1 cm and the heat conductance  $k$  is obtained from Table (4.4) from the entry for a tool steel. Thus, even with good heat sinking the surface reaches a temperature of  $300 + 429 = 729 \text{ C}$ . To maintain a temperature limit of  $150^\circ\text{C}$  requires that  $\Delta T$  be less than  $150^\circ\text{C} - 25^\circ\text{C}$  (room temp.) = 125 K. This can be achieved by reducing the beam current by  $1 \text{ mA} \times 125 \text{ K}/429 \text{ K} = 0.3 \text{ mA}$ . Note that if the sample thickness were only 0.1 cm,  $\Delta T$  would be 43 K which is an acceptable temperature rise and the full available beam power could be utilized.

Equation (4.32) can be used to calculate the temperature rise for the worst case scenario where there is no heat sinking with the result,

$$T_s - T_o = 2.3 \times 10^{17} (\text{ions/cm}^2) \times 90,000 (\text{eV}) \times 1.6 \times 10^{-19} (\text{Joules/eV})/3.7 (\text{Ws/cm}^3\text{-K}) = 895 \text{ K}$$

or, if  $T_o = 25 \text{ C}$ , then  $T_{\text{max}} = 920 \text{ C}$ . This is clearly too hot for most applications. Hence, implantation without heat sinking can be considered only for doses about one order-of-magnitude less, or about  $3 \times 10^{16}/\text{cm}^2$  for steels.

#### Time and Cost

The time required to implant this target is computed using equation (4.36) with the result,

$$t_i = \frac{16 (\text{mA-s})}{10^{17} (\text{ions})} \times \frac{2.3 \times 10^{17} (\text{ions/cm}^2)}{1.0 (\text{mA}) \times 1.0 \times 0.3} \times 25 (\text{cm}^2) = 51 \text{ min}$$

where  $F_b = 1.0$  is estimated for the beam utilization factor and  $F_i = 0.3$ .  $F_b$  is always 1.0 when  $F_i$  is less than 1 for a flat geometry workpiece or in general when there is no packing factor associated with placing parts in the beam. If the sample were 1 mm thick, instead of 1 cm, or if it had the thermal conductivity of Cu, then full beam power could be used,  $F_i$  would be 1.0 and the implant would take 18 min. For an hourly charge of \$300/hour, these samples would cost approximately \$300/hour, for a single batch. For a large number of such implants the cost could be as low as  $\$0.14 \times 25 \text{ cm}^2 = \$3.50$  per flat (from Table 4.6).

## B. Cylindrical Geometry Workpiece

Suppose we have a 3" long tool steel cylinder that is clamped along a 1" length at one end such that there is good heat conduction at the interface ( $h=1 \text{ W/cm}^2\text{-K}$ ). The remaining 2" length of the 1/2" diameter cylinder is to be implanted with Ti ions at an energy of 100 KeV as it is rotated at a speed of 10 rpm. The treatment requires the sputter saturated dose. The available beam current is 1 mA and the vendor can either flood the entire diameter of the rod or place a mask in front of the rod to confine the beam to a width equal to the radius of the rod. This limits the impingement angles to  $\pm 30^\circ$  with respect to the surface normal whereas in the former geometry, all angles  $\pm 90^\circ$  are allowed to impinge upon the sample.

$R_p, \Delta R_p, S$

From Table (4.1),  $R_p$  and  $\Delta R_p$  are 40 nm and 18 nm, respectively. From equation (4.6) the sputtering coefficient is

$$S = \frac{0.042 \times 149 [0.271]}{4.92 \times 0.0848} = 4.7$$

Sartwell and Baldwin (1985) have established that during implantation of reactive ions into steels, surface carburization causes the effective sputtering coefficient to be reduced by about a factor-of-two in vacuum pressures greater than  $10^{-6}$  Torr. Therefore, a more realistic estimate of the sputtering coefficient is  $4.7/2 = 2.4$ .

$\phi_s, C_s$

We will compute  $\phi_s$  and  $C_s$  for implantation with and without a mask. For a mask with a width equal to the radius of the cylinder, the beam is confined to impingement angles  $\pm 30^\circ$  from the surface normal. The beam is incident at angles smaller than  $30^\circ$  for most of the time that the surface is rotating through the ion beam so that the effective angle is much less than  $30^\circ$ . Because the cosine function does not depart appreciably from a value of 1 for angles  $< 30^\circ$ , it is a good approximation to assume normal incidence for this geometry. Note in Fig. (4.14) that only a small error is introduced by assuming  $\theta = 0$  and  $\theta = 30^\circ$  are equivalent. Thus, for this mask configuration equation (4.25) gives,

$$\begin{aligned} \phi_s (90\%) &= \frac{0.96}{2.4} \left[ 8.48 \times 10^{22} \right] \left[ 40 + \sqrt{2} 18 \right] \left[ 10^{-7} \right] \\ &= 2.2 \times 10^{17}/\text{cm}^2 \end{aligned}$$

and the surface concentration from equation (4.21) is,

$$C_s (90\%) = 0.9 \times 0.99 / 2.4 = 0.37.$$

Therefore, the profile of Ti ions may be approximated by a 37% concentration from the surface to a depth of 40 nm.

The same calculation may be done for the case of no mask with the help of a simplifying approximation that the effective angle of implantation is  $30^\circ$ . This angle can be rationalized by noting that as a



point on the diameter rotates through the beam, it spends one-half of the time at angles greater than  $30^\circ$  and one-half of the time at angles less  $30^\circ$ . Then equation (4.29) for  $\phi_s$  (90%) gives,

$$\begin{aligned}\phi_s (90\%) &= \frac{0.96}{2.4} \left[ 8.48 \times 10^{22} \right] \left[ \cos 30 \right]^{5/3} \left[ 40 \cos 30 + \sqrt{2} 18 \right] \left[ 10^{-7} \right] \\ &= 1.6 \times 10^{17} / \text{cm}^2\end{aligned}$$

and equation (4.28) for  $C_s$  gives,

$$C_s = 0.9 \times 0.95 \times 0.787 / 2.4 = 0.28.$$

Therefore, a first-order approximation of the profile is a Ti concentration of 28% extending to a depth of  $40 \cos(30^\circ) = 35$  nm. These values of  $C_s$  and  $R_p$  for the two methods of masking compare well with the data in Fig. (4.15) for Ti implanted AISI 52100 steel. The trend of smaller concentration and smaller depth in going from normal incidence with a mask to no mask is reproduced and the absolute values are an adequate first order estimate. This agreement shows that with reasonable values of  $R_p$ ,  $\Delta R_p$ , and  $S$ , and if other artifacts are not prevalent such as radiation enhanced diffusion and preferential sputtering, then reasonable agreement between measured and calculated profiles may be expected.

### Power Limit

In both methods of masking the total power on the sample will be essentially the same since all the beam power available can be concentrated in the rod whether or not it is masked. There may be small differences in the power because of the beam utilization factor  $F_b$  will differ for the two cases. Equation (4.33) can be used to calculate the maximum power than can be delivered to the rod in order not to exceed  $150^\circ\text{C}$ . For our steel rod,  $k=0.2$  and there is good thermal heat sinking at one end. The rod diameter  $D$  is  $1/2"$  and the length  $l$  exposed to the beam is  $2"$ . First we find if the area of the clamping system is large enough to conduct the heat from the workpiece, across the interface, and into the heat sink which is kept at room temperature. The rod is clamped along the  $1"$  section which has a surface area  $\pi D l = \pi \times 1.27\text{cm} \times 2.54 \text{ cm} = 10 \text{ cm}^2$ . Equation (4.34) indicates that for full beam power incident on the cylinder  $\Delta T$  across the interface will be

$$\Delta T = \frac{100 \text{ W}/10\text{cm}^2}{1 \text{ W}/\text{cm}^2} = 10 \text{ K}$$

which is a very acceptable value.

The maximum temperature of the rod tip is given by equation (4.33) multiplied by  $1/2$  to account for the fact that the power is incident along the entire rod (Hirvonen, 1986). The temperature rise for full available power incident on the rod becomes  $\Delta T = J l / 2k$  but the 100 Watts of power must conduct through the cross-sectional area of the rod,  $\pi D^2 / 4$ , in order to reach the heat sink, so the effective power density incident on the rod for the purpose the heat conduction calculation is  $100 \text{ Watts} / 1.27 \text{ cm}^2 = 79 \text{ Watts}/\text{cm}^2$ . The temperature rise is then

$$\Delta T = 79 \times 5.08 / (2 \times 0.2) = 1000 \text{ K}.$$

Therefore, to maintain the tip temperature below  $150^\circ\text{C}$ , the available beam current at 100 keV must be reduced by the factor  $1 \text{ mA} \times (150-25)/1000 = 0.125 \text{ mA}$  or an average power of 12.5 Watts incident on the sample.

### Time and Cost

$F_b$ , the beam utilization factor, is less than 1 only when the temperature rise is not a problem and available beam current limits the implantation time, and  $F_i$  is less than 1 only when the temperature

rise limits the beam current on the sample. Therefore, for this case  $F_b = 1$  and  $F_i = 0.125$  because the beam current had to be reduced from the 1 mA available to 0.125 mA. The time of implantation given by equation 4.36 for the two methods of implantation becomes

$$t_i = \frac{16 \text{ (mA-s)}}{10^{17} \text{ (ions)}} \times \frac{2.2 \times 10^{17} \text{ (ions/cm}^2\text{)}}{1.0 \text{ (mA)}} \times \frac{\pi \times 1.27 \times 5.08 \text{ (cm}^2\text{)}}{0.125 \times 1.0}$$

$$= 95 \text{ min} \quad (\text{for } \pm 30^\circ \text{ mask});$$

$$t_i = \frac{16}{10^{17}} \times \frac{1.6 \times 10^{17}}{1.0} \times \frac{\pi \times 1.27 \times 5.08}{0.125 \times 1.0} = 69 \text{ min} \quad (\text{for no mask})$$

where the area to be implanted is  $\pi D l$  and  $l$  is the 2" exposed length of the cylinder. The cost for the former is  $\$300/\text{hx}1.58\text{h} = \$475$  and for the latter the cost if  $\$300/\text{hx}1.15\text{h} = \$345$ . For batch processing the cost and time may be considerably reduced because  $F_i$  can become 1.0 with  $F_b$  as high as 0.8. For cylindrical geometry and batch processing the price could be as low as  $20 \text{ cm}^2 \times \$0.2/\text{cm}^2 = \$4$  per rod. The rotation speed of 10 rpm indicates that for the case of no mask,  $10 \text{ rpm} \times 60 \text{ min} = 690$  revolutions of the rod during implantation. This is an ample number of revolutions to ensure that there is uniform coverage of the rod. The total number of revolutions should be greater than 100 to achieve a uniformity of better than 1%.

### C. Quality Control

In general, ion implantation does not change the visual appearance of a part such as color, luster, shape or roughness. Unlike parts that have been coated with TiN by chemical vapor deposition and which have a gold color, the ion-implantation vendor returns a part to the customer which may look no different that it did prior to treatment. Understandably the customer, unfamiliar with the process, may have doubts as to whether the correct dose was used for the implantation or whether the parts were cooled properly and not overheated. Whether or not overheating occurred can be tested with microhardness measurements before and after implantation. Whether a part received the correct dose is a quality control question that can only be addressed by experimental measurements of implanted-atom profiles after processing.

There are several implanted atom profiling techniques, some of which were used to generate the profiles shown in Figures (4.7 - 4.15). The most common are Rutherford Backscattering Spectroscopy (RBS), Nuclear Reaction Profiling (NRP), Auger Electron Spectroscopy combined with sputter erosion of the surface (AES), Secondary Ion Mass Spectroscopy (SIMS), and X-ray Fluorescence Spectroscopy (XRF). All of these techniques are available at various vendors that specialize in surface analysis services. Table (5.1) lists features of each of the methods and thus provides guidelines for which method may apply to a specific ion-target combination.

Table 5.1 — Methods Used to Obtain Implanted Atom Depth Concentration Profiles

	IONS Detected	Sensitivity	Accuracy of Dose Meas.	Depth Profile Meas.	Typical Lateral Resolution (mm)
RBS	$M_1 > M_2$	good	good	yes	1
	$M_1 < M_2$	poor	fair	yes	1
NRP	$M_1 \leq 52$	good	good	yes	1
AES	$M_1 > 5$	fair	fair	yes	0.1
SIMS	$M_1 > 1$	excellent	fair	yes	0.1
XRF	$M_1 \geq 24$	good	fair	no	0.01 (in SEM)

RBS is overall the most convenient and precise method when the mass  $M_1$  of the ion is heavier than the  $M_2$  of the substrate. NRP is the most precise for light elements in heavy substrate but it is more time consuming than AES or SIMS. Therefore, the precision of NRP is frequently used to calibrate AES and SIMS methods for a given system so that the more convenient methods can be used to generate profiles in a shorter space of time. XRF is useful for quality control during batch processing. If, using one of the other four techniques, it is known that the desired profile has been produced in a part, then XRF can be calibrated with this part using x-ray heights of an element in the substrate and the signal from the implanted ion. This is a measure of the retained dose. Then other parts treated the same way in a batch process can be checked by XRF to see if the same dose is retained. Since XRF is a very common and easily used instrument, this is a quick and inexpensive quality control procedure.

Another aspect of quality control is the uniformity of ion dose over the implanted area. All of the methods in Table (5.1) have lateral resolution capabilities and could be used to profile different regions of the implanted area to check for uniformity of ion dose.

## VI. SUMMARY

This chapter has touched upon all of the practical issues involved in applying ion implantation to parts and tools. In Section II, the reader can determine whether or not ion implantation is of interest by applying the criteria and features listed in Table (2.3) and by perusing the list of current applications in Table (2.2). Once satisfied that ion implantation is applicable, the fundamental physical principles of the process are briefly described in Section III for those interested in the formation of the surface alloy. This section may be skipped with no consequence to the understanding of the subsequent sections. Section IV, the heart of the chapter, is a detailed account of the considerations required to successfully ion implant a part and includes tables and formulas for the computation of the implanted atom concentration profile, computation of sample heating and methods to control it, and computation of the implantation time and cost. Section V is a summary of Section IV which illustrates the planning of implantation treatments in a step-by-step procedure. Materials scientists and engineers who were unfamiliar with ion implantation technology should after reading this chapter, feel comfortable discussing the details of the treatment with vendors or with researchers in the field.

The primary advantages driving the development of ion implantation technology for metals applications are the low processing temperature and the fact that the surface finish is not effected (no re-finishing required). It is likely that surface coating technologies will never overcome the surface finish advantage of ion implantation; but the low temperature processing advantage could conceivably be equaled by new and innovative coating technologies. For example, if adherent and bulk property TiN CVD coatings could be applied at 125°C, some of the applications now using ion implantation may be also treated using this method. Another new technique under development is ion beam assisted deposition (IBAD) where a low energy beam (100 to 1000 eV) of nitrogen ions strikes a surface on which Ti is simultaneously being deposited by means of a physical vapor deposition technique. This method shows promise of being able to produce bulk property refractory films at very low temperatures. In spite of these possible new developments, ion implantation processing of metals will continue to play a role in applications and in materials research and development because of the speciality of the process. By virtue of the unique ability to implant any ion into practically any target, ion implantation as a speciality industry can be expected to grow in pace with materials technology in general.

## VII. ACKNOWLEDGMENTS

I wish to express appreciation to Fred Smidt for his continued support of this project and for critical reading of the chapter, and to my colleagues Ken Grabowski, Bob Gossett, Dick Kant, Jim Hirvonen and Irv Manning, whose work makes up a large portion of this chapter. Special thanks also to Robin Watkins for her invaluable assistance in constructing the range tables.

## VIII. REFERENCES

- Armini, A.J. and Bunker, S.N., (1985) Nucl. Instrum. and Meth. in Phys. Res. **B6**, 214.
- Beeler J.R., (1969) Radiation Damage in Reactor Materials, I.A.E.A., Vienna.
- Beeler J.R. and Besco D.G., (1964) Report GE-TM 64-5-20 and Report GE-TM 64-5-21.
- Behrisch R., (1981), **Sputtering by Ion Bombardment**, ed., R. Behrisch (Springer, NY).
- Biersack J.P., (1983) **Ion Implantation Equipment and Techniques**, eds., H. Ryssel and H. Glawisching (Springer, NY).
- Borders J.A., and Poate J.M. (1976) Physical Review **B13**, 969.
- Butler J.W., (1981), **Encyclopedia of Chemical Technology**, Vol. 13, (John Wiley) p. 706.
- Cheng Y.T., Nicolet M.-A. and Johnson W.L. (1985) Appl. Phys. Lett. **45**, 185.
- Czjzek C., Ford J.L.C. Jr., Love J.C., Obsenshain F.E. and Wegener H.H.F. (1968) Phys. Rev. **174**, 331.
- Dautreppe D., (1971) **Hyperfine Interactions in Excited Nuclei**, eds., G. Goldring and R. Kalish (Gordon and Breach, New York) p. 1255.
- Davisson, C.M. (1986) Nucl. Instrum. and Meth. in Phys. Res. **B13**, 421.
- Dearnaley G., (1983) Thin Sol. Films, **107**, 315.
- Doran D.G. (1970) Radiat. Eff. **2**, 249
- Erginsoy C., Vineyard G.H. and Englert A. (1964) Phys. Rev. **133**, 595.
- Erginsoy C., Vineyard G.H. and Simizu (1965) Phys. Rev. **139**, 118.
- Feldman L.C., Augustyneak W.M. and Kauffman E.N. (1971) **Hyperfine Interactions in Excited Nuclei**, eds., G. Goldring and R. Kalish (Gordon and Breach, New York), p. 174.
- Feldman L.C. and Murnick D.E. (1971) **Hyperfine Interactions in Excited Nuclei**, eds., G. Goldring and R. Kalish (Gordon and Breach, New York) p. 226.
- Gibbons J.F., Johnson W.S. and Mylroie S.W., (1975) **Projected Range Statistics in Semiconductors and Related Materials** (Halsted, Stroudsburg, PA).
- Gossett, C.R., (1980), unpublished data.
- Grabowski K.S., Correll F.D. and Vozzo F.R., (1985) Nucl. Instrum. and Meth. in Phys. Res. **B7/8**, 798.
- Grabowski K.S., Hartley N.E.W., Gossett C.R. and Manning I., (1984) Mater. Res. Soc. Symp. Proc. Vol. 27 eds., G.K. Hubler, O.W. Holland, C.R. Clayton and C.W. White (Elsevier, NY) p. 615.
- Grabowski K.S., Hubler G.K., Hodge E.T., Jeffries R.A., Clayton C.R., Wang Y-F. and Kuhlman G., (June 27, 1985a), Naval Research Laboratory Memorandum Report 5592.

- Grabowski K.S. and Kant R.A., (1983) **Ion Implantation: Equipment and Techniques**, eds., H. Glawischnig (Springer, NY) p. 364.
- Grant W.A. (1981) Nucl. Instrum. and Meth. **182/183**, 809.
- Handbook of Chemistry and Physics, 47th edition, (CRC, Cleveland, OH), p. F-134.
- Hirvonen J.K., (1984) **"Ion Implantation and Ion Beam Processing of Materials"**, eds., G.K. Hubler, O.W. Holland, C.R. Clayton and C.W. White, Mater. Res. Soc. Symp. Proc. Vol. **27** (Elsevier, NY) p. 621.
- Hirvonen, J.K., (1986) to be published (ASM).
- Hubler G.K., Singer I.L. and Clayton C.R., (1985) Mater. Sci. and Engineer. **69**, 203.
- Hubler G.K. (1984) unpublished data.
- Johnson R.A., (1964) Phys. Rev. **134**, A1329.
- Johnson W.L., Cheng Y.T., Van Russern M. and Nicolet M.A. (1985) Nucl. Instrum. and Meth. in Phys. Res., **B7/8**, 657.
- Johnson W.S. and Gibbons J.F., (1970) Projected Range Statistics in Semiconductors (Stanford U.P., Stanford, CA).
- Kinchin G.H. and Pease R.S. (1955) **Reports on Progress in Physics**, The Physical Society, London, Vol. 18, p. 1.
- Land D. and Brennan J., (1978) **Atomic and Nuclear Data Tables** Vol. 22, 235.
- Liau Z.L. and Mayer J.W. (1980), **Ion Implantation**, ed. J.K. Hirvonen (Academic, NY) Chap. 2.
- Lindhard J., Scharff, M. and Schiott H.E. (1963) Matt. Fys. Medd. Dan. Vid. Selsk, **36** #14.
- Manning I. (1984) to be published.
- Manning I. (1985) unpublished data.
- Manning I. and Mueller G.P. (1974) Comp. Phys. Commun. **7**, 85.
- Matsunami N., Yamamura Y., Itikawa Y., Itoh N., Kazumata Y., Miyagawa S., Marita K., Shimizu R. and Tawara H., (1984) **Atomic Data and Nuclear Tables**, Vol. **31**, 1.
- Pogoshev D., Valori R. and Hubler G.K. (1983) ASME J. Lubrication Technol. **105**, 534.
- Pronko P.P., McCormick A.W., Ingram D.C., Rai A.K., Woollam J.A., Appleton B.R. and Poker D.B. (1984), Mat. Res. Soc. Proc. Vol. **27**, eds., G.K. Hubler, O.W. Holland, C.R. Clayton and C.W. White (Elsevier, NY) p. 559.
- Reynolds G. (1985) Nucl. Instrum. and Meth. in Phys. Res. **B13**, 467.
- Reynolds G.W., Knudson A.R. and Gossett C.R., (1981) Nucl. Instrum. and Meth. **182/183**, 179.
- Sartwell, B.D. and Baldwin, D.A. (1985) Mater. Sci. and Engin. **69**, 539.

- Sigmund P. (1969) *Phys. Rev.* **184**, 383.
- Sigmund P. (1981) in **Sputtering by Ion Bombardment**, ed., R. Behrisch (Springer, NY).
- Singer I.L. (1984) *Vacuum* **34**, 853.
- Singer I.L. and Jeffries R.A. (1984), *Mater. Res. Soc. Symp. Proc. Vol. 27*, eds., G.K. Hubler, O.W. Holland, C.R. Clayton and C.W. White (Elsevier, NY) p. 673.
- Sioshansi P. (1984), *Thin Sol. Films*, **118**, 61.
- Smidt F.A. and Sartwell B.D. (1985), *Nucl. Instrum. and Meth. in Phys. Res.*, **B6**, 70.
- Smith B., (1977) **Ion Implantation Range Data for Silicon and Germanium Device Technology** (Research Studies Press, Forest Grove, Oregon).
- Sood D.K. (1978) *Physics Letters* **68A**, 469.
- Vianden R., Kauffman E.N. and Rodgers J.W. (1980) *Phys. Rev.* **B22**, 63.
- Westmoreland J.E. and Hubler G.K. (1977) unpublished data.
- Wilson W.D., Haggmark L.G. and Biersack J.P. (1977), *Phys. Rev.* **B15**, 2458.
- Winterbon K.B. (1975) **Ion Implantation Range and Energy Distributions: Low Ion Energies**, Vol. II (Plenum, NY).

# ION-IMPLANTED ELEMENTS WHICH IMPROVE PROPERTIES OF METALS

[illegible]

Fig. 1.1 — Periodic Chart of the elements that illustrates ions that have been used to improve oxidation (o), aqueous corrosion (c), wear (w), or fatigue (f).

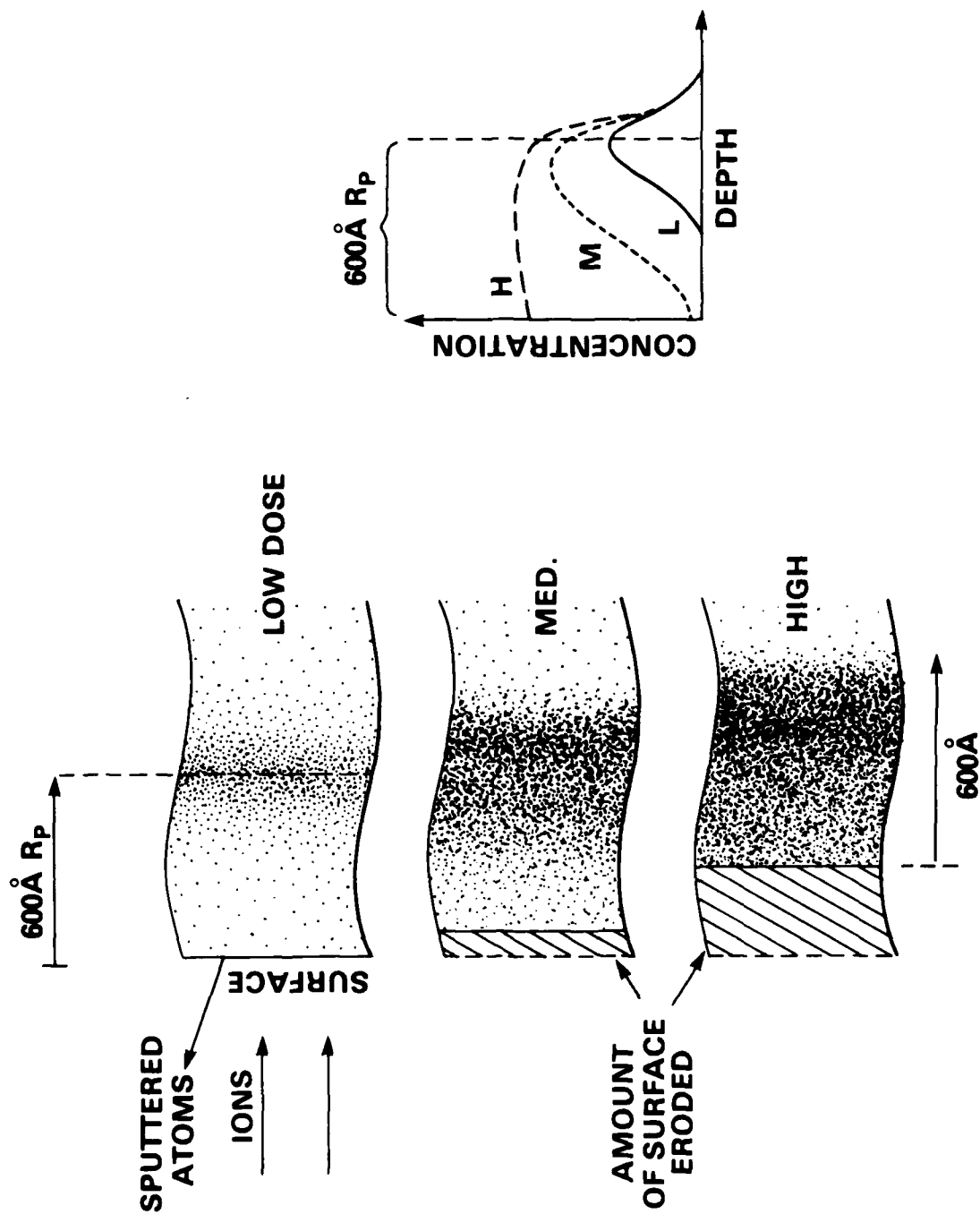


Fig. 2.1 — Schematic view of the development of the concentration profile of ions implanted to high doses.



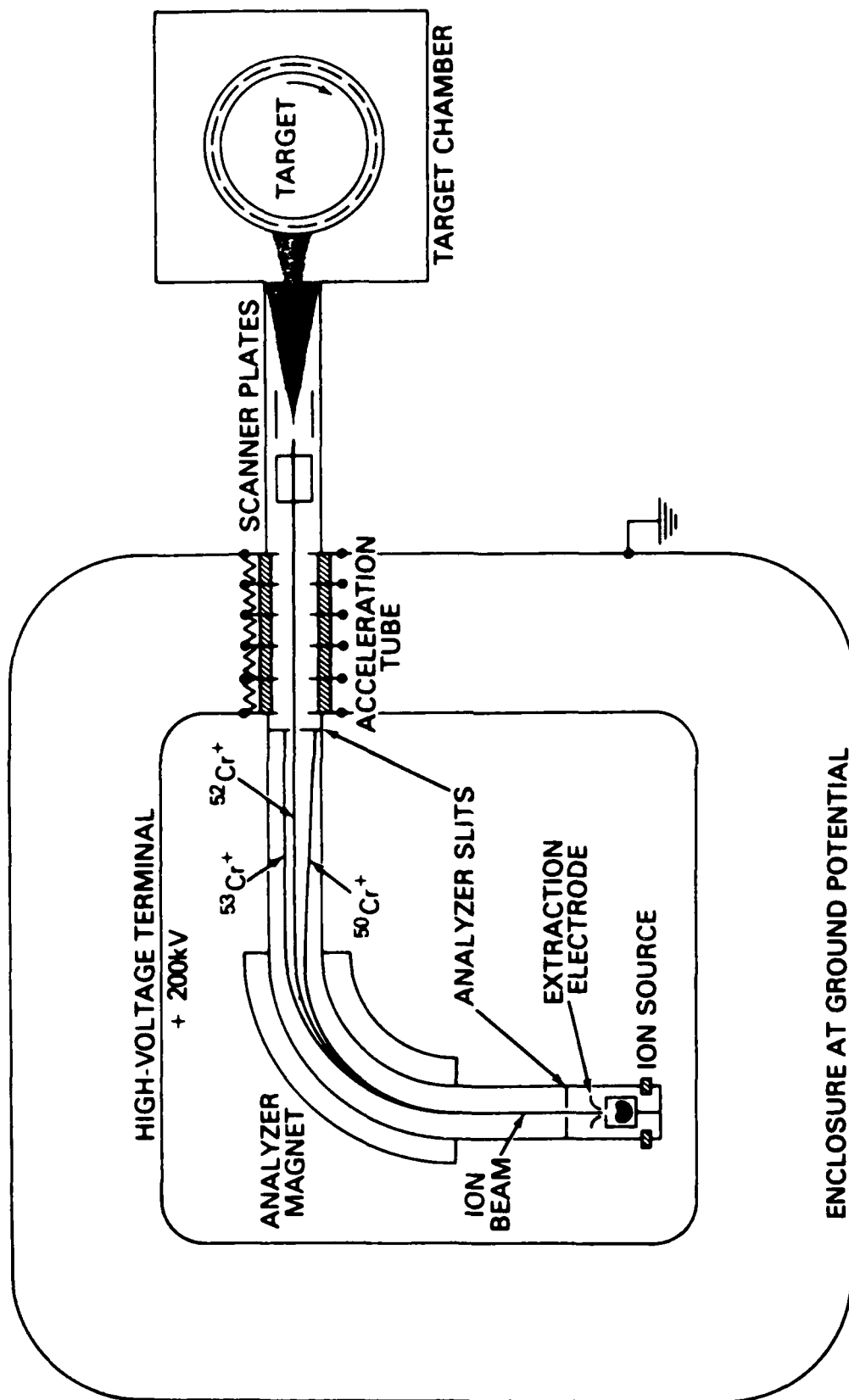


Fig. 2.2 — Schematic view of production type ion implantation system.

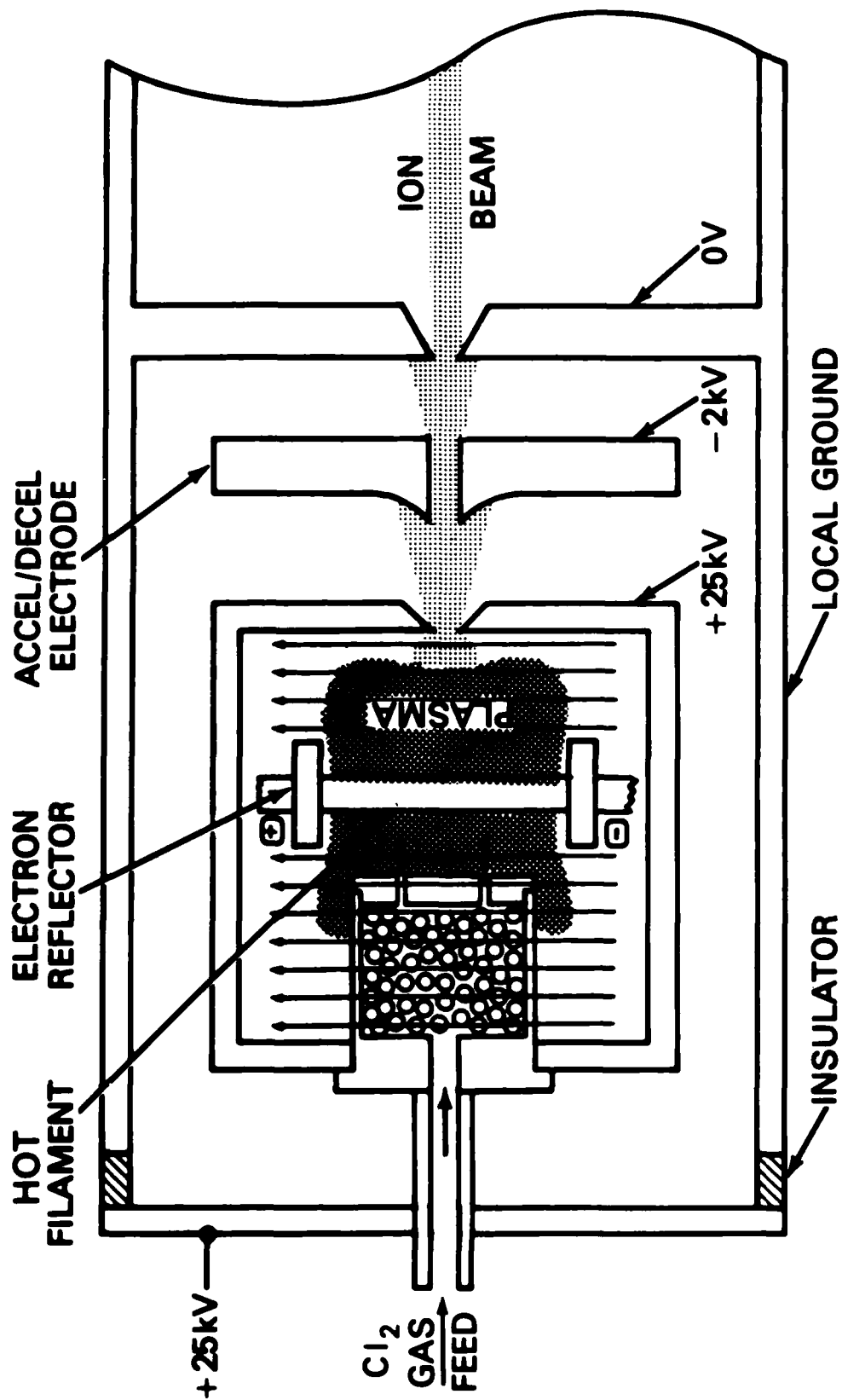


Fig. 2.3 — Schematic view of typical ion source for ion implantation system.

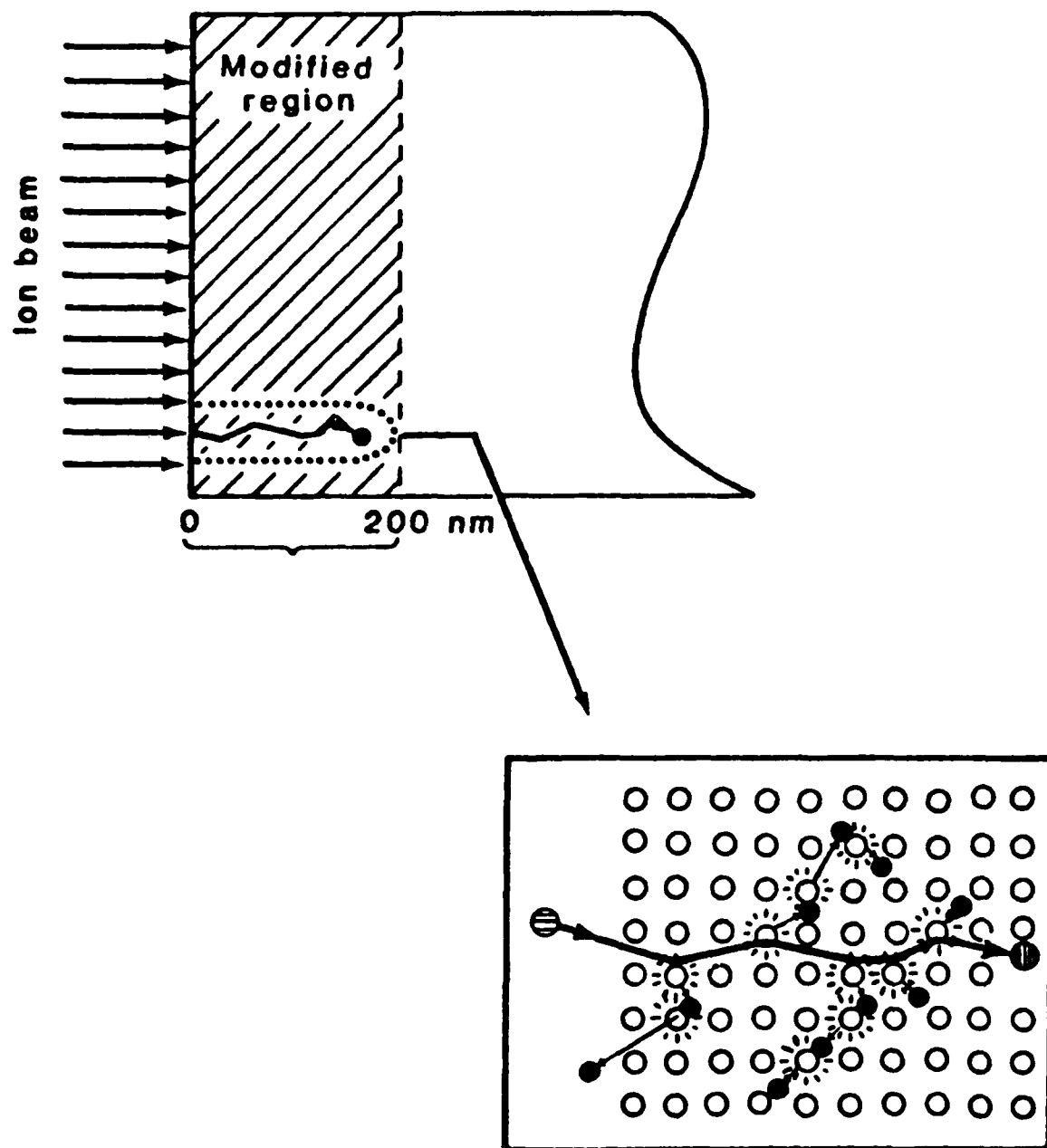


Fig. 3.1 — Schematic view of ion implantation process (top) and a single collision cascade (bottom) (adapted from Picraux, 1984).

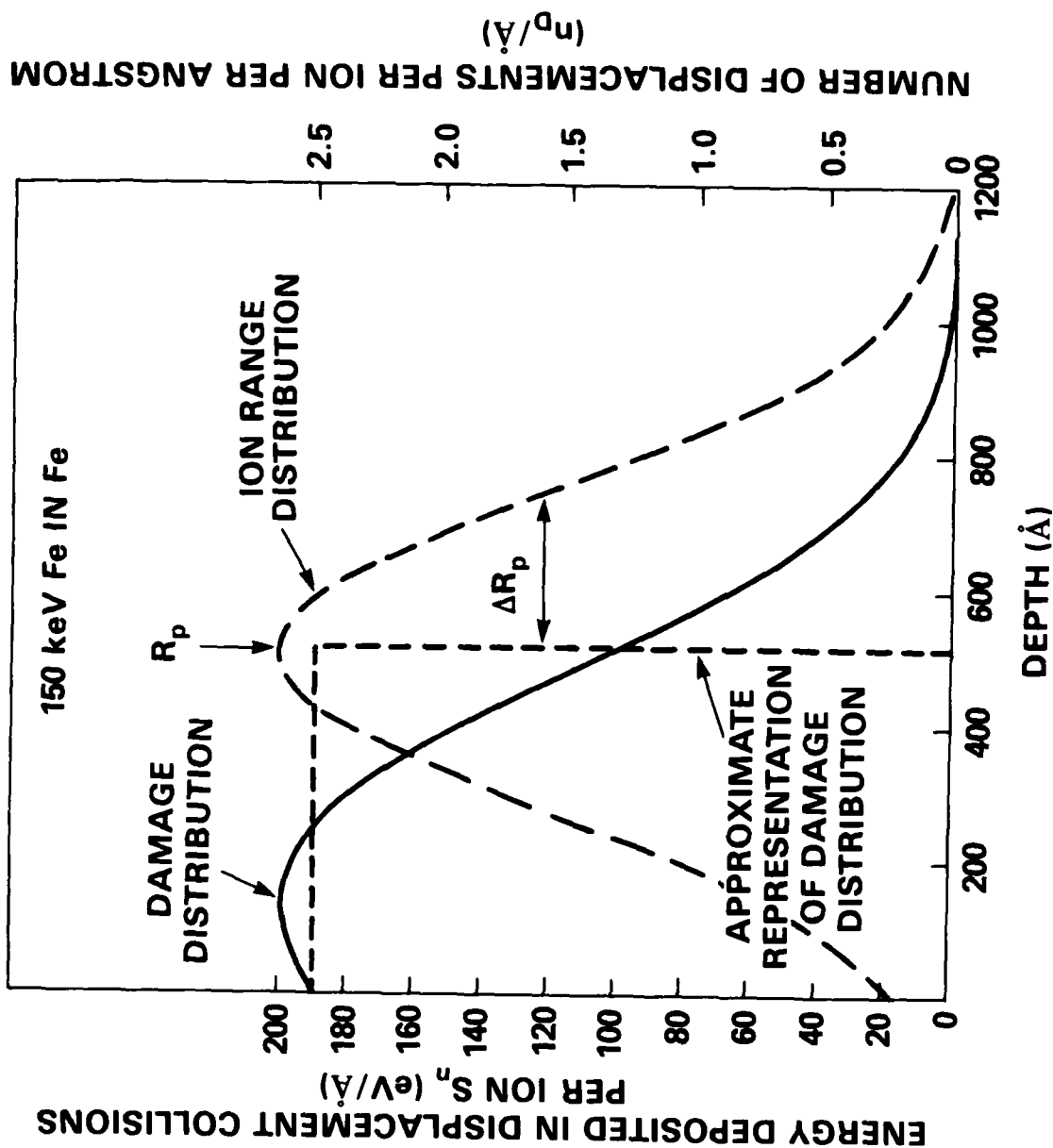


Fig. 3.2 — Calculated energy deposited in displacement collisions vs depth and range distribution for 150 keV Fe ions incident on an iron substrate. The dashed line is an easily calculated approximation to the damage distribution.

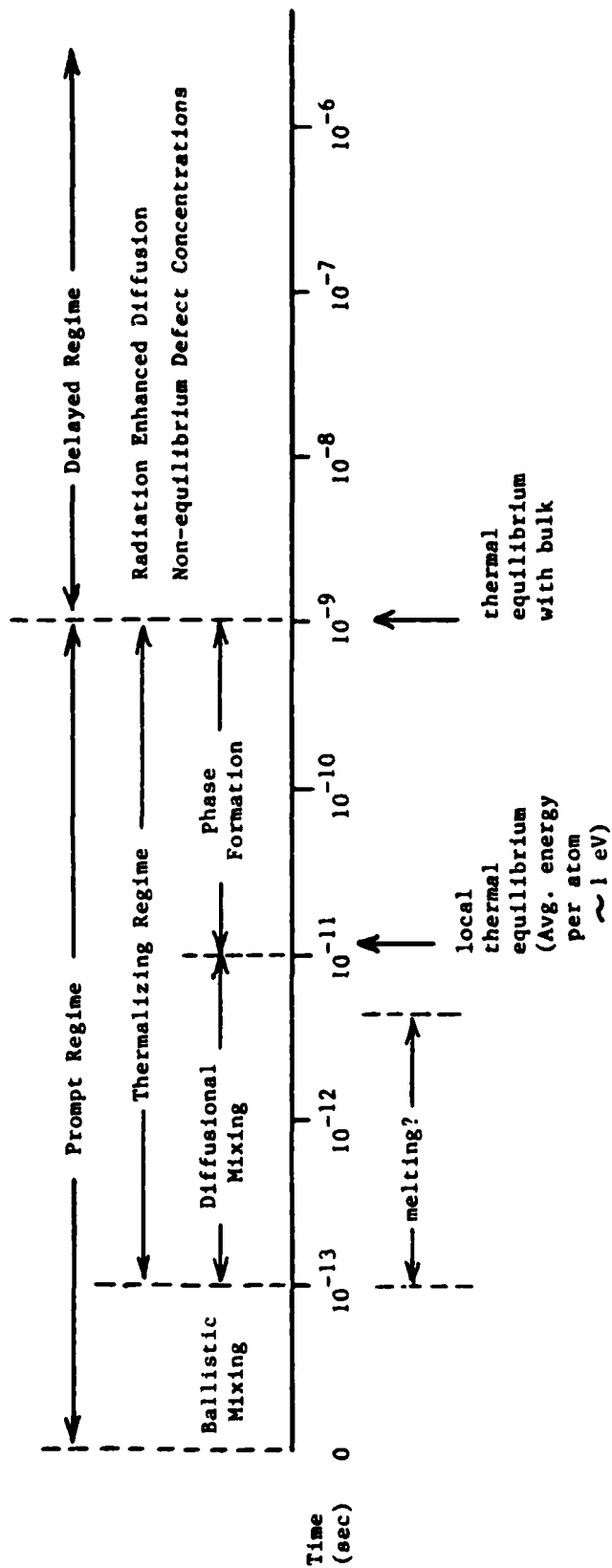


Fig. 3.3 -- Time regimes of a system undergoing ion mixing.

## KINETICS OF SOLID-SOLID TRANSFORMATION

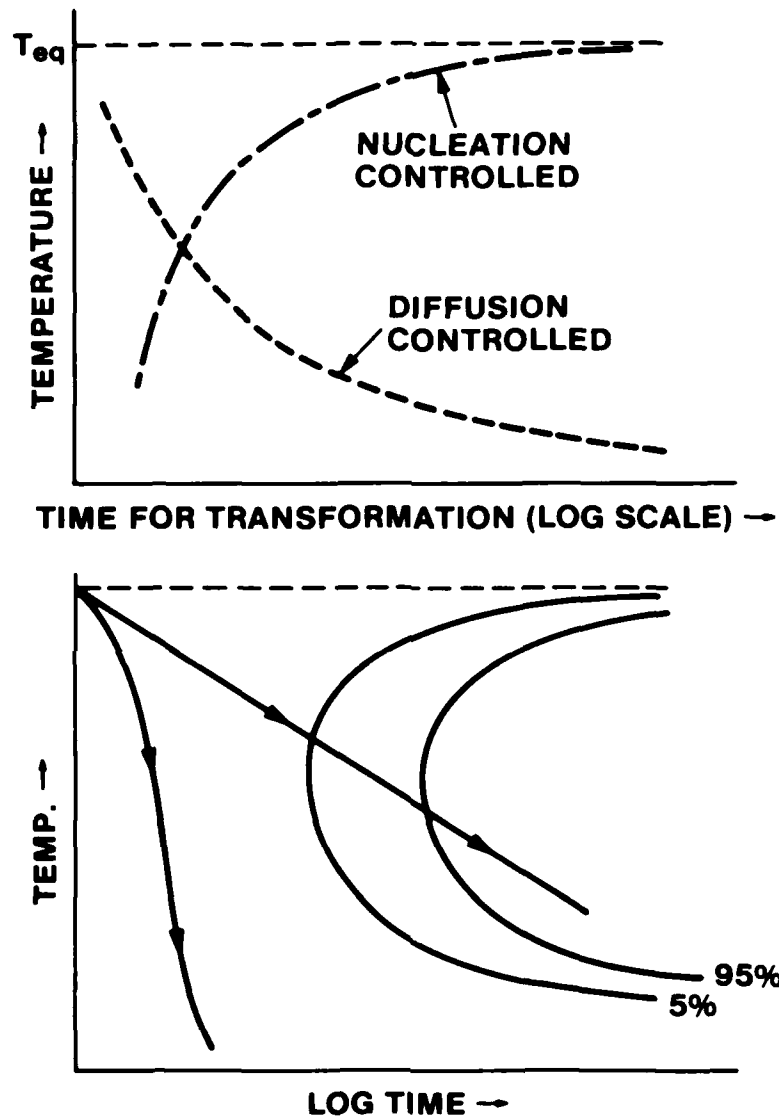


Fig. 3.4 — Time-Transformation-Temperature diagram demonstrating effect of the fast-quench ( $10^{14}$ K/s) in a collision cascade on formation of metastable microstructures.

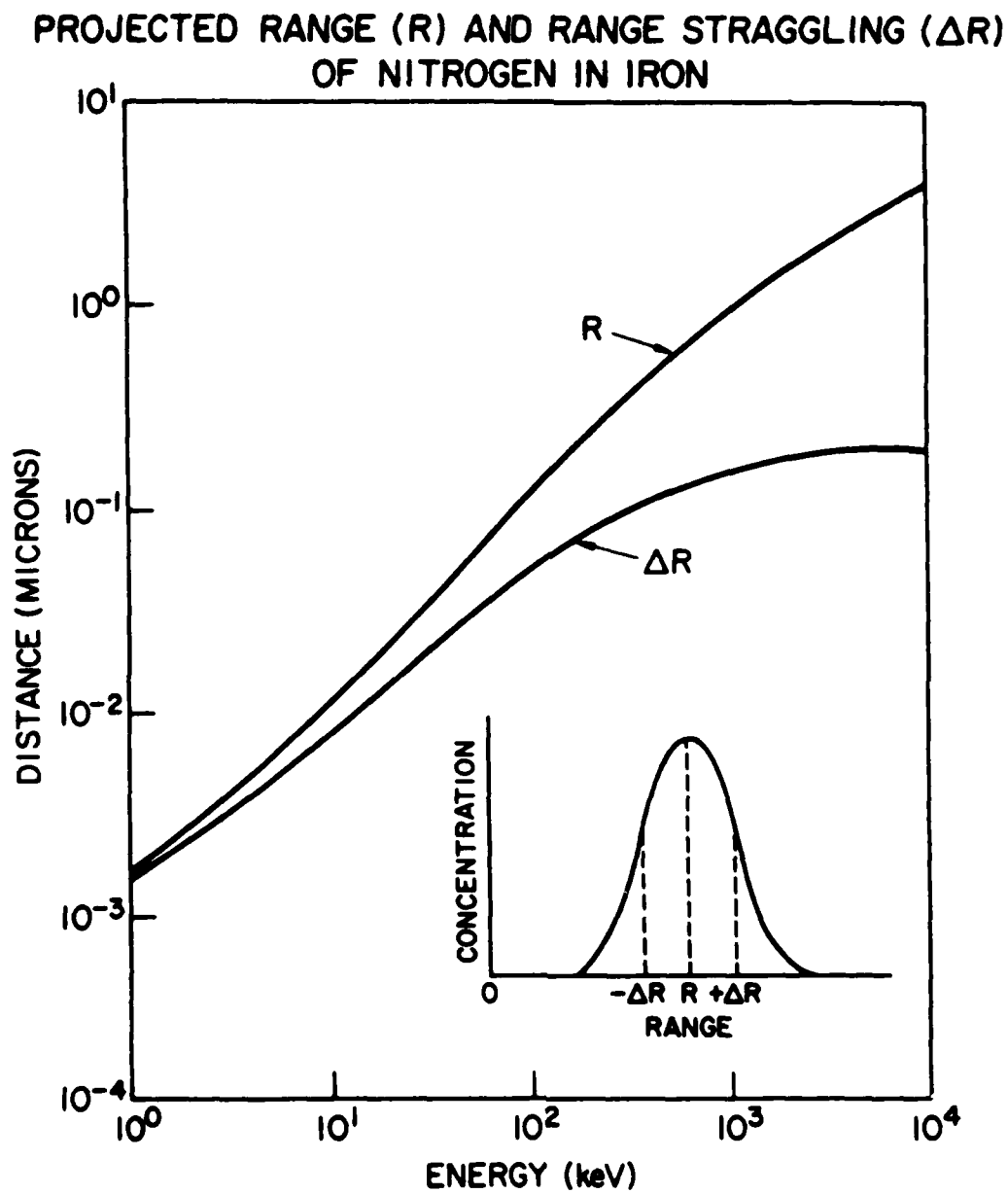


Fig. 4.1 — The projected range,  $R_p$ , and standard deviation of the projected range  $\Delta R_p$ , of nitrogen ions implanted into iron versus the initial ion energy.

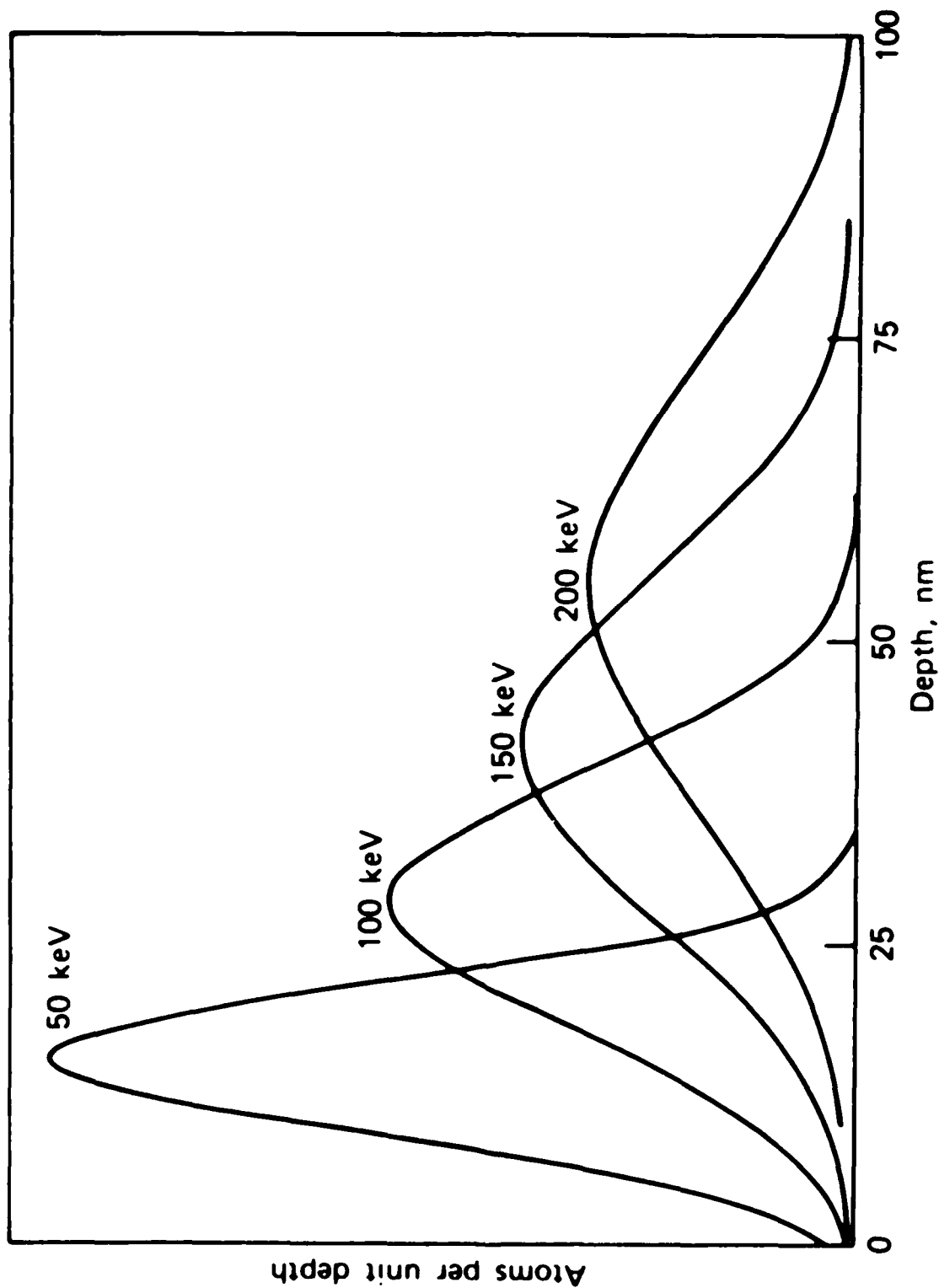


Fig. 4.2 — The calculated range distribution for iron ions of various incident energies,  $E_i$ , in an iron substrate at normal incidences (from Butler, 1981).



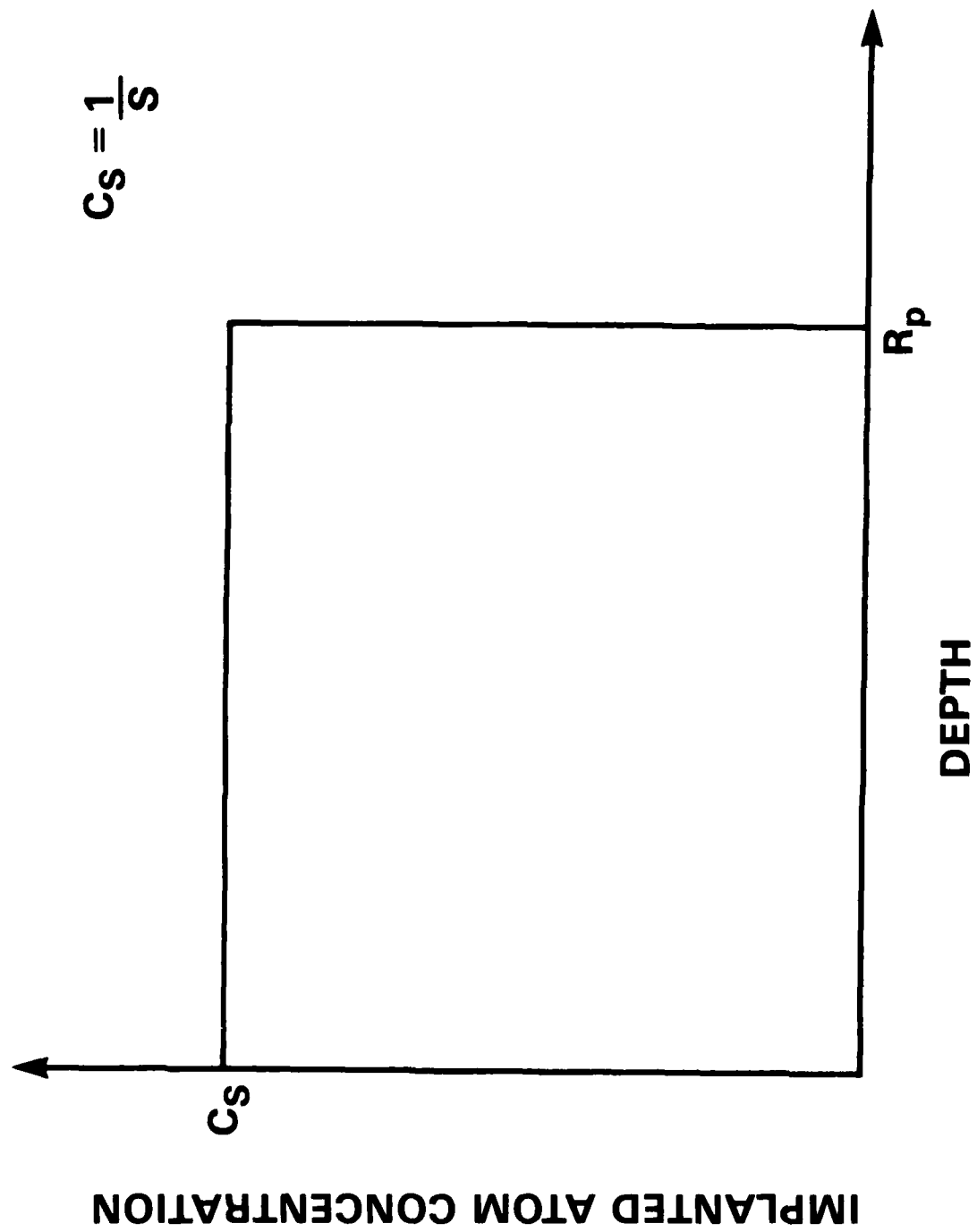


Fig. 4.3 — Zeroth-order estimates of the implanted atom profile at saturation dose.

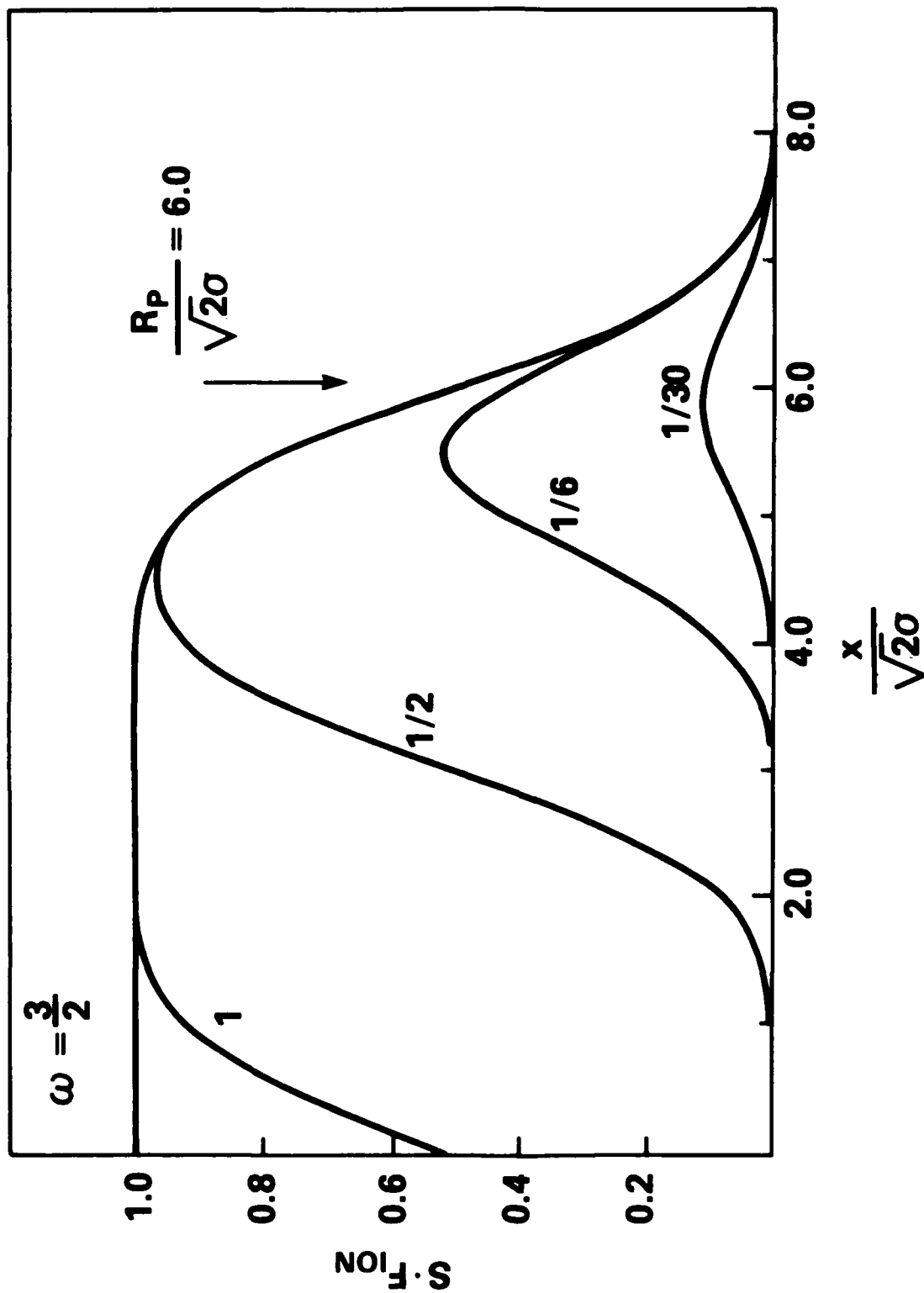


Fig. 4.4a — Development of implanted ion distribution with increasing dose for the cases, a)  $R_p / \Delta R_p = 6\sqrt{2}$  and b)  $R_p / \Delta R_p = \sqrt{2}$ .  $W$  is the amount of material sputtered away relative to the projected range,  $R_p$  (from Grabowski et. al., 1984).

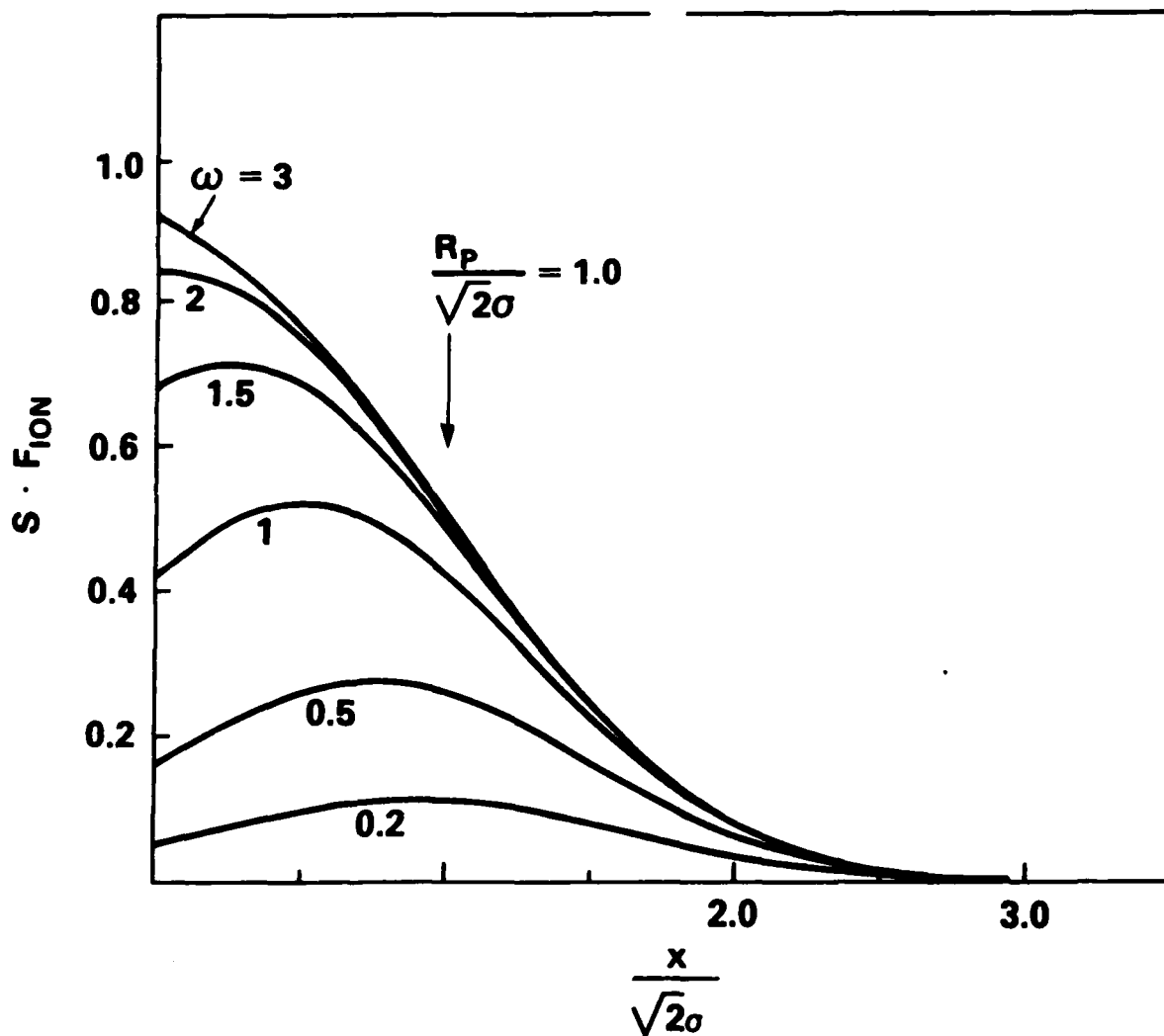


Fig. 4.4b (Continued) — Development of implanted ion distribution with increasing dose for cases, a)  $R_p/\Delta R_p = 6\sqrt{2}$  and b)  $R_p/\Delta R_p = \sqrt{2}$ .  $W$  is the amount of material sputtered away relative to the projected range,  $R_p$  (from Grabowski et. al., 1984).

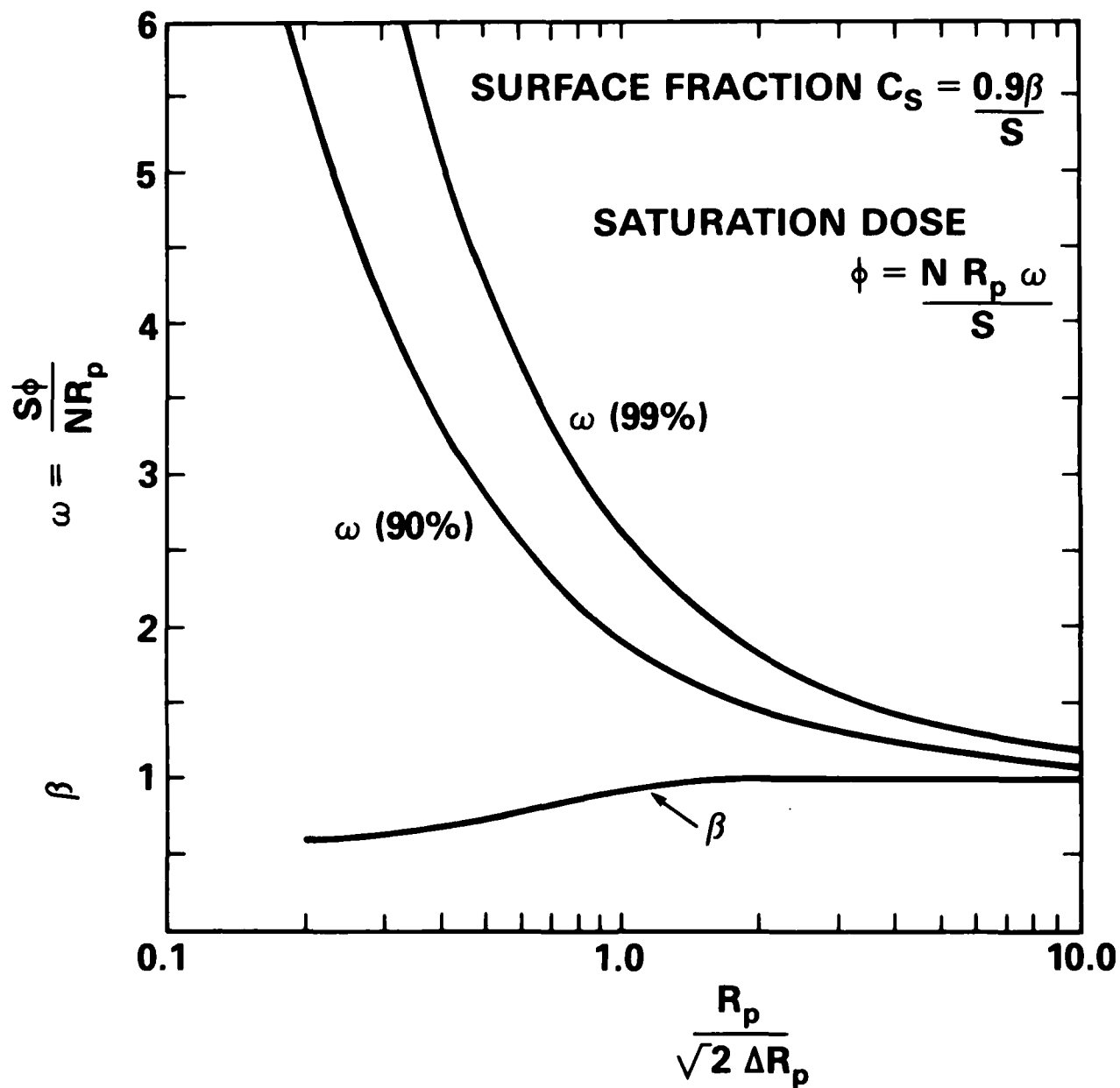


Fig. 4.5 — Dose to achieve 90% and 99% of saturation dose versus the modified ratio of  $R_p$  and  $\Delta R_p$ . The curve labeled  $\beta$  corrects the surface concentration for the tail of the Gaussian distribution which extends beyond the surface.

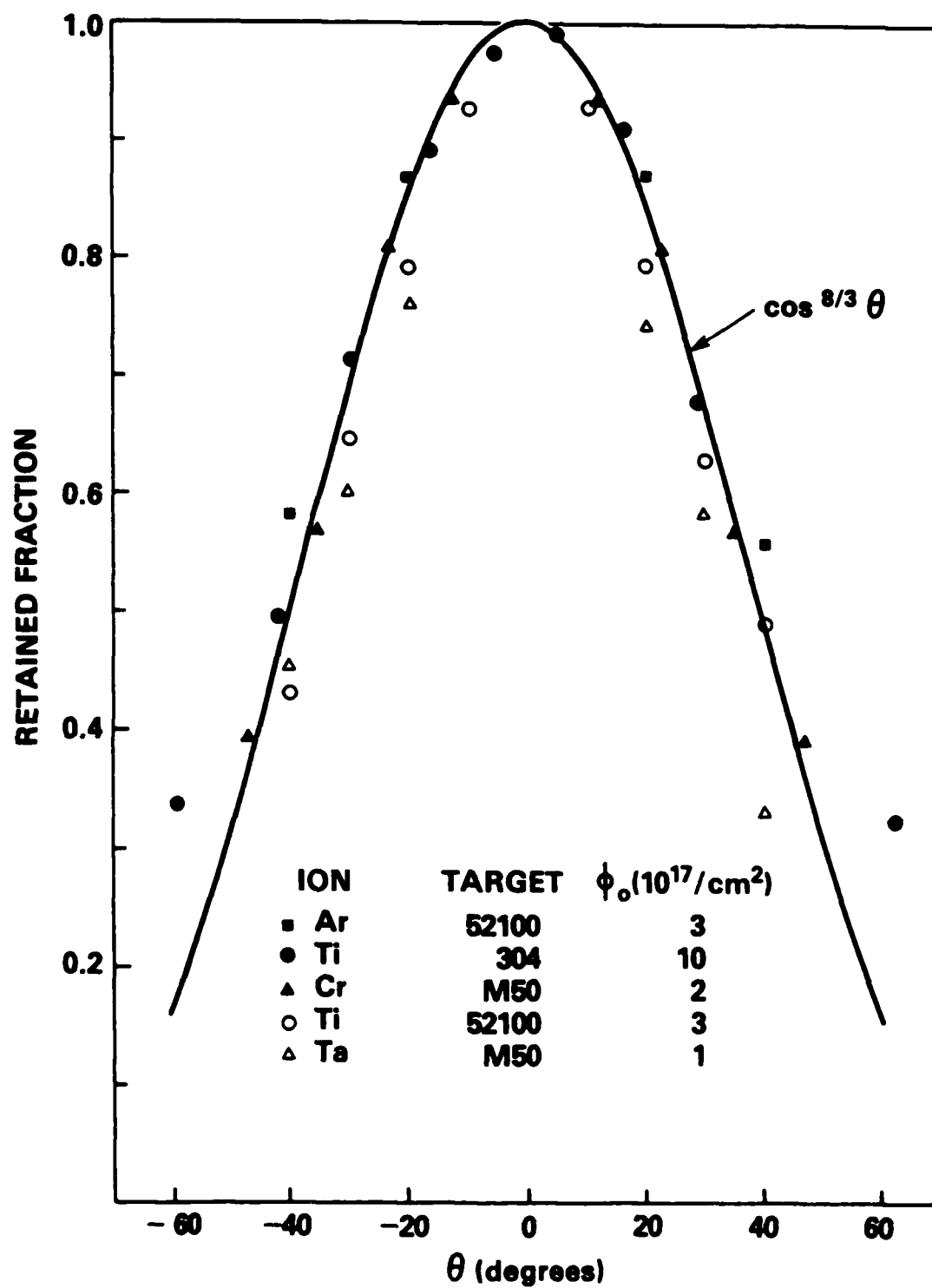


Fig. 4.6a — Normalized retained dose at saturation from simplified theory and from measurements on steel cylinders. Data points at normal incident are not plotted (from Grabowski et al., 1984).

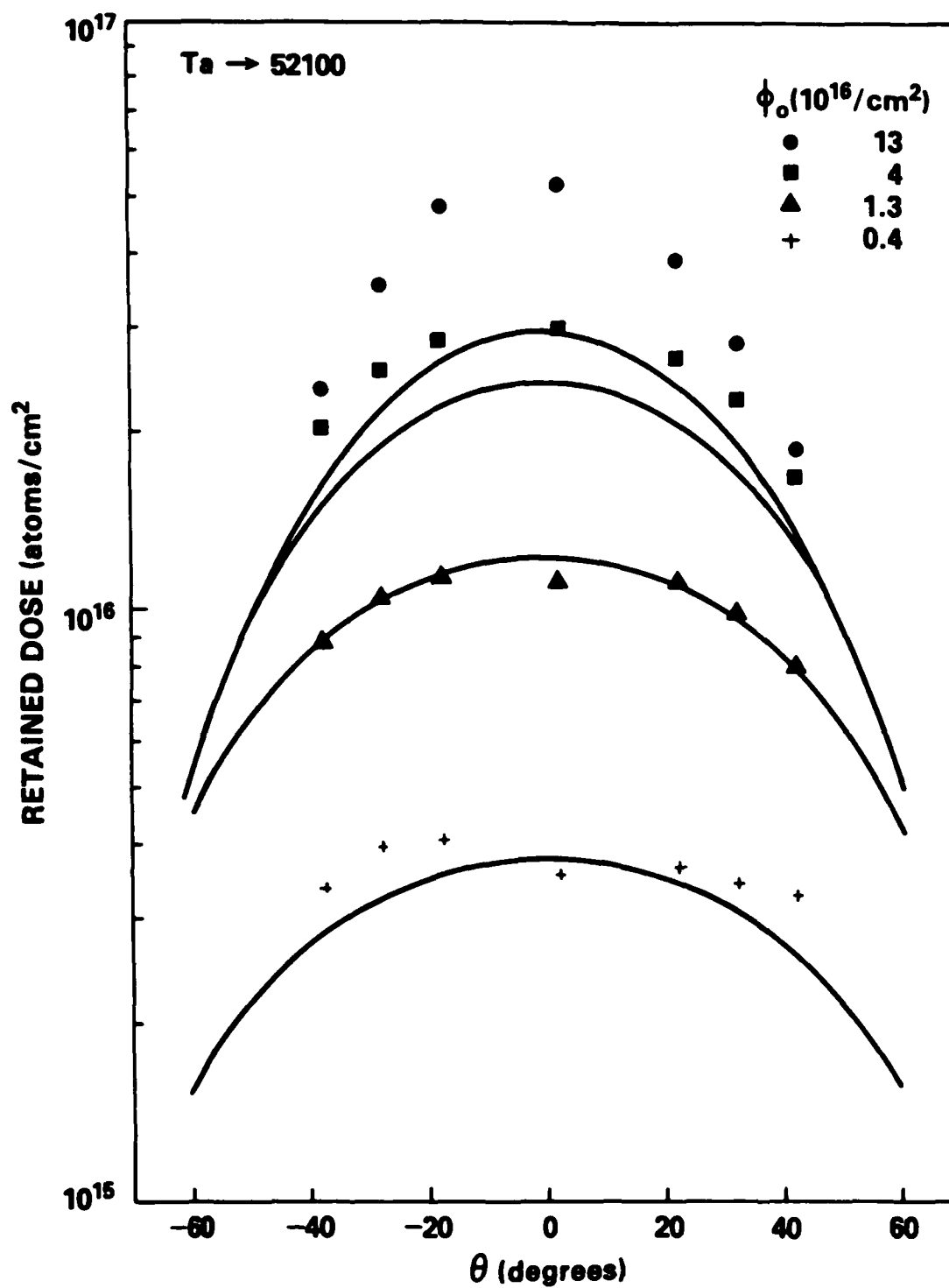


Fig. 4.6b — Retention of implanted Ta in 52100 cylinder as a function of fluence and angle of incidence for theory and experiment (from Grabowski et. al., 1984).

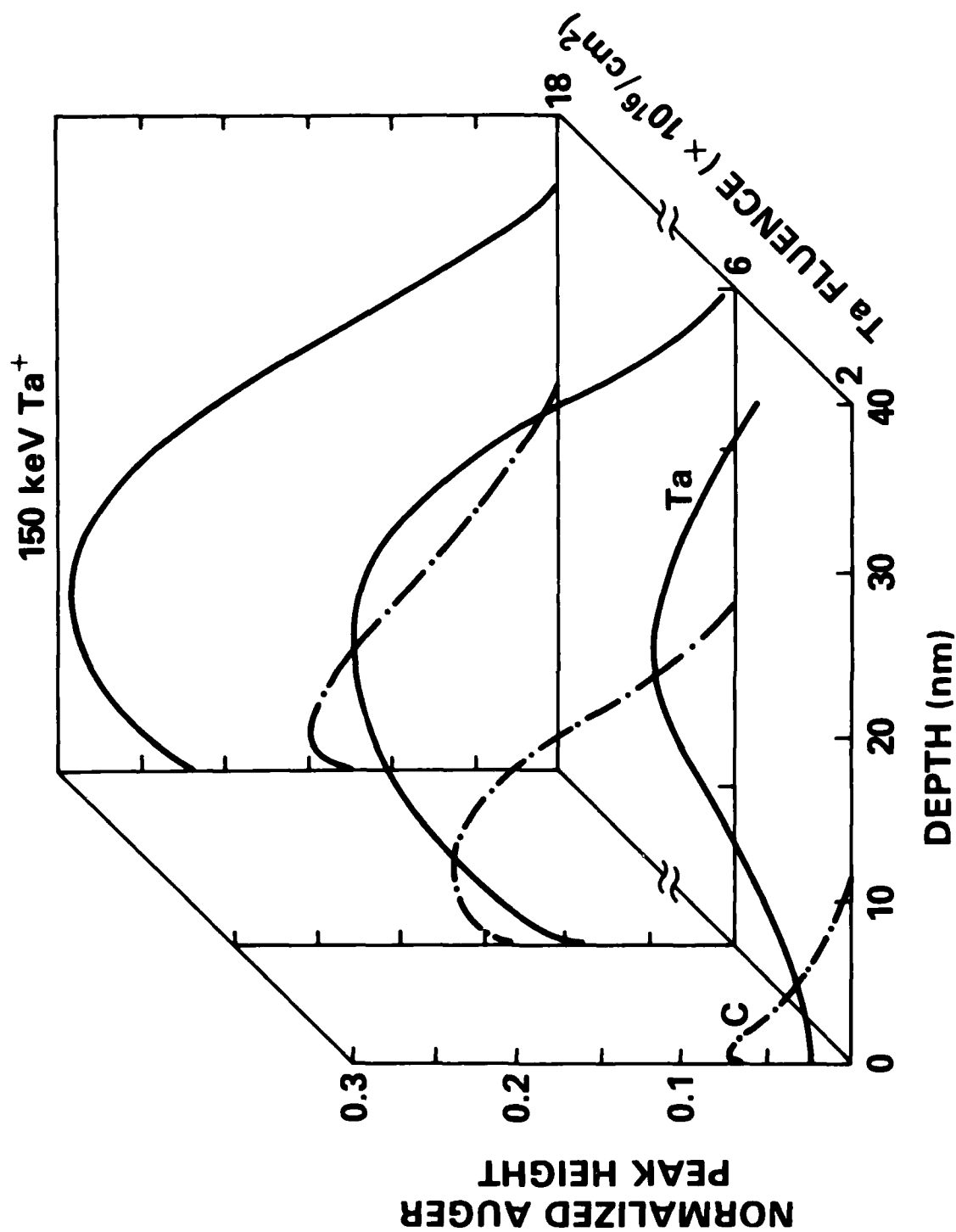


Fig. 4.7 — Auger sputter depth profiles of Ta and C for pure Fe films implanted with three different doses of 150 keV Ta ions (from Hubler et al., 1985).

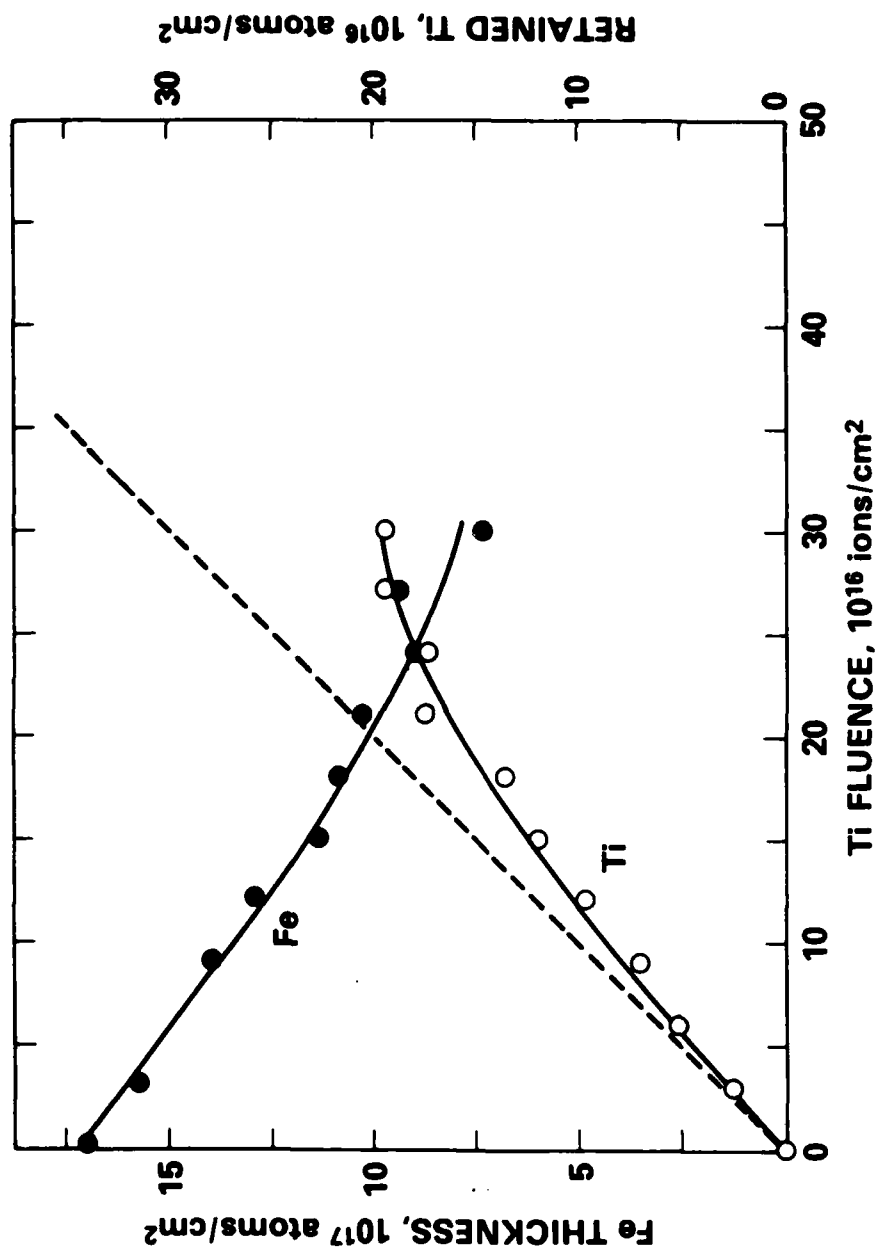


Fig. 4.8a — Iron thickness and retained dose of titanium as a function of fluence for the implantation of 190 keV  $Ti^{+}$  ions into an iron film 200 nm thick electron beam deposited onto a Si(100) substrate (a) for an implantation performed at a pressure of  $8 \times 10^{-9}$  Torr and (b) for an implantation performed with the chamber backfilled with CO to a pressure of  $1 \times 10^{-6}$  Torr: -----, expected retained dose in the zero-sputtering limit (from Sartwell and Baldwin, 1986).



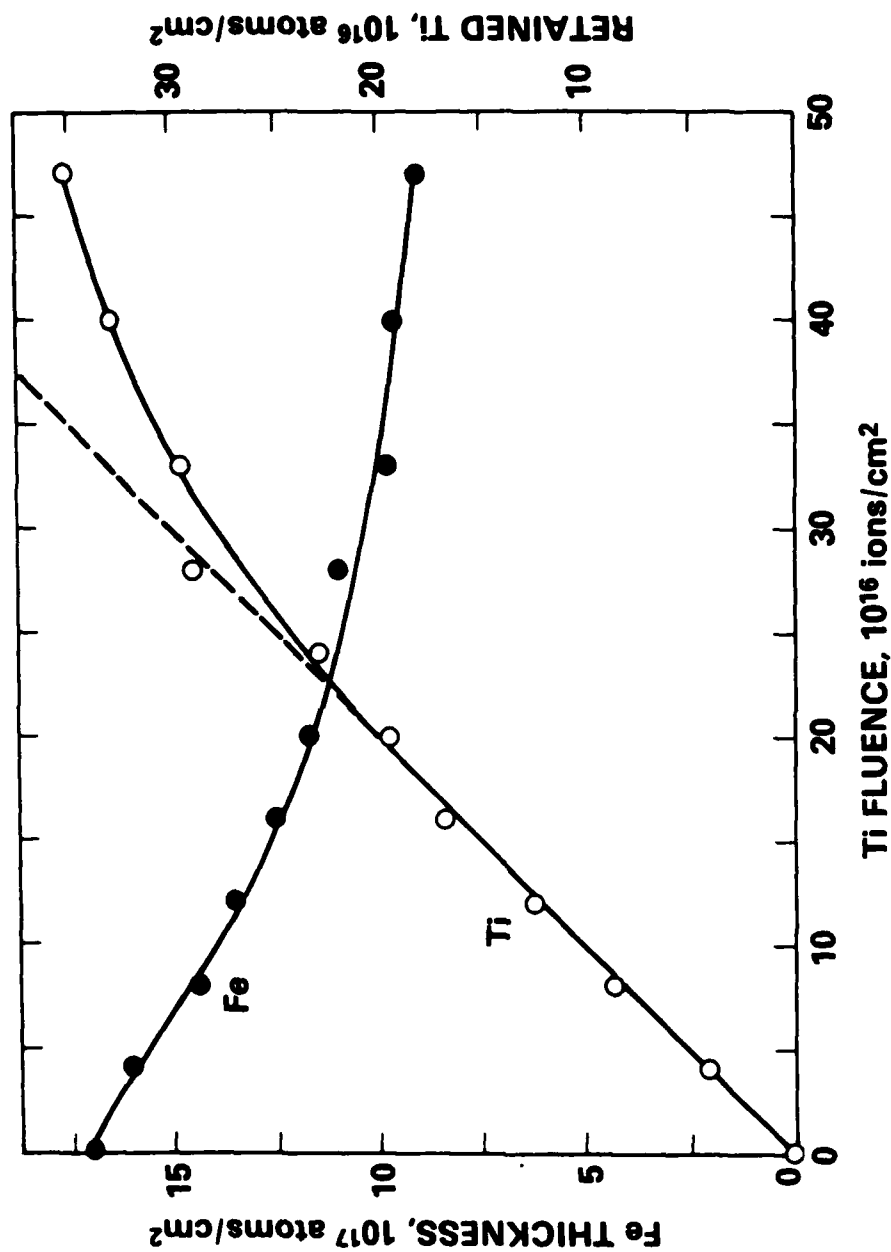


Fig. 4.8b — Iron thickness and retained dose of titanium as a function of fluence for the implantation of 190 keV  $Ti^{+}$  ions into an iron film 200 nm thick electron beam deposited onto a Si(100) substrate (a) for an implantation performed at a pressure of  $8 \times 10^{-9}$  Torr and (b) for an implantation performed with the chamber backfilled with CO to a pressure of  $1 \times 10^{-6}$  Torr: -----, expected retained dose in the zero-sputtering limit (from Sartwell and Baldwin, 1986).

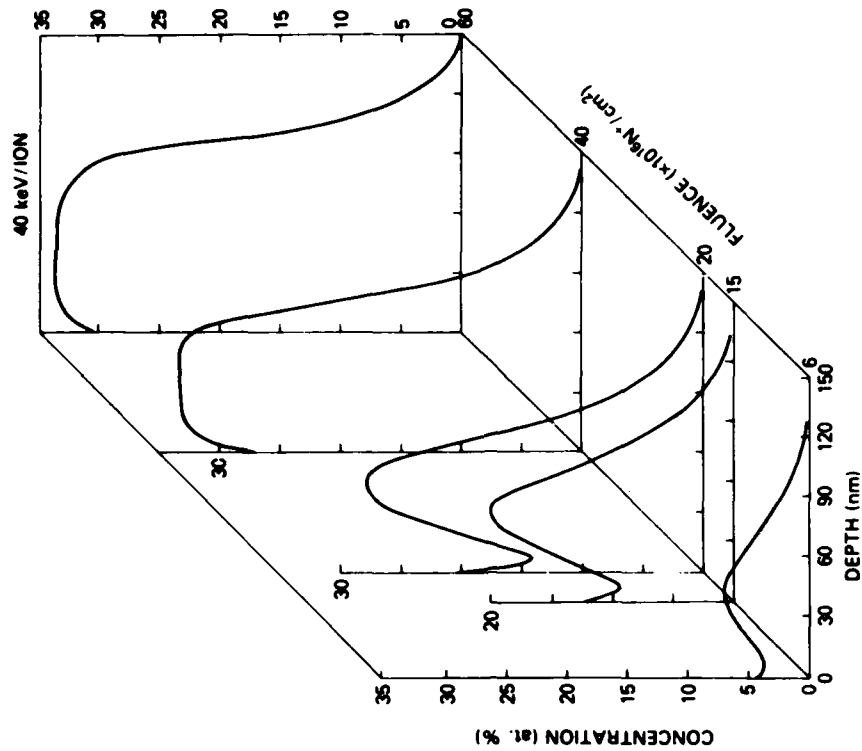
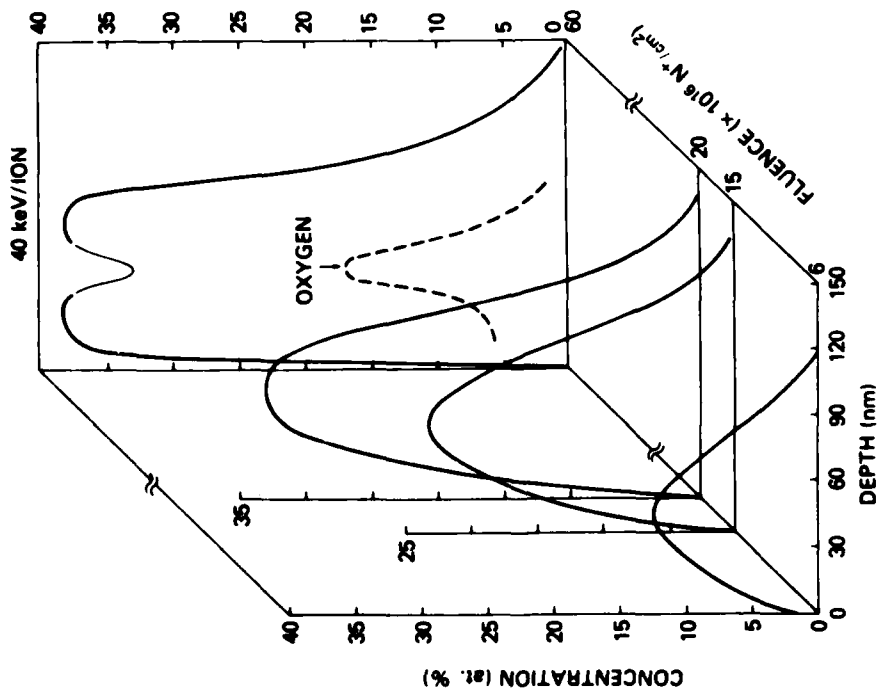


Fig. 4.9 — Concentration vs depth profiles of N in N-implanted (a) AISI 304 steel and (b) AISI 1018 steel as a function of dose (from Singer, 1984).

# C AND Ti PROFILES IN Ti-IMPLANTED STEEL

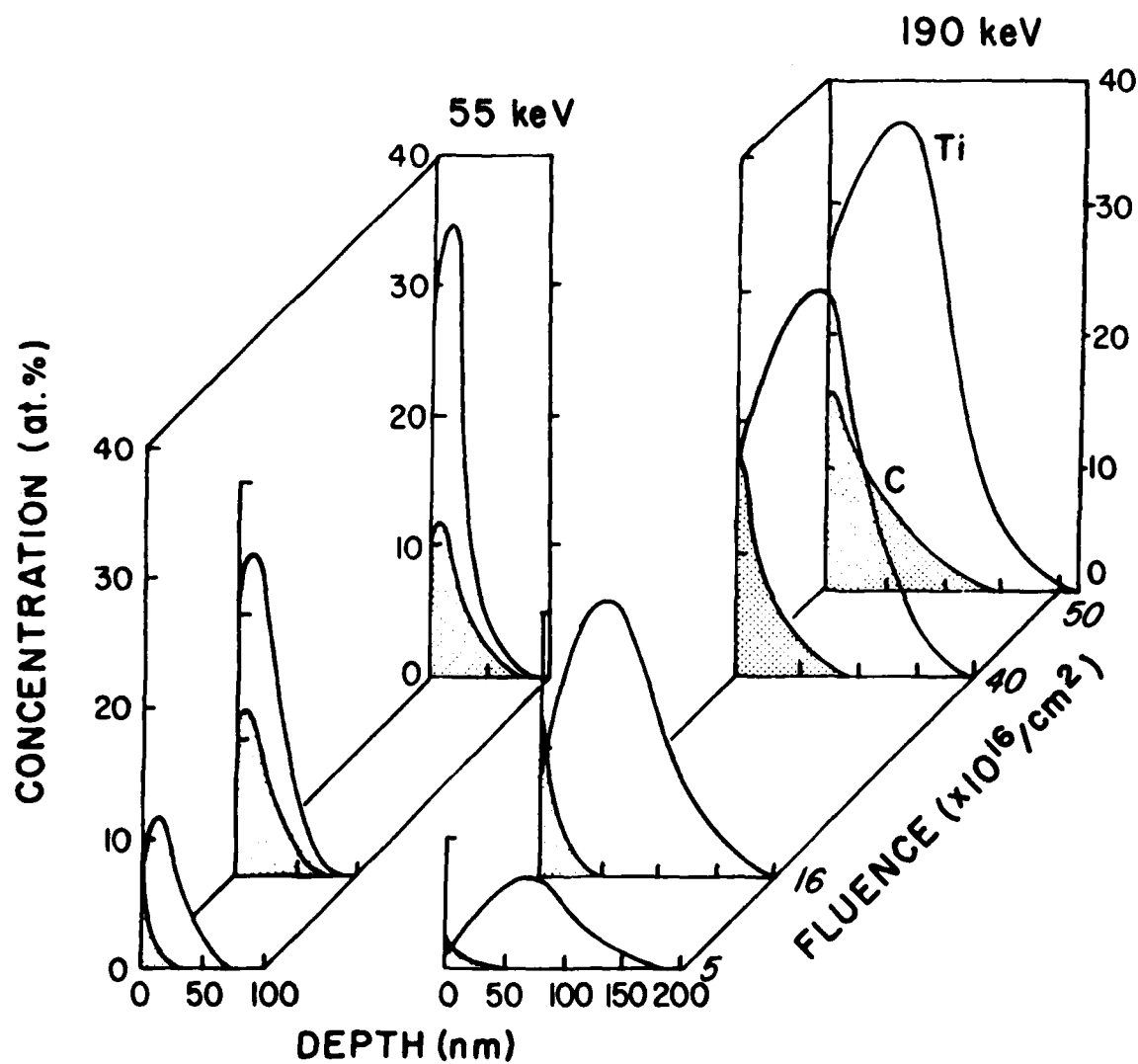


Fig. 4.10 — Concentration vs depth profiles for Ti and excess carbon in Ti-implanted AISI 52100 steel at several doses and energies (from Singer, 1984).

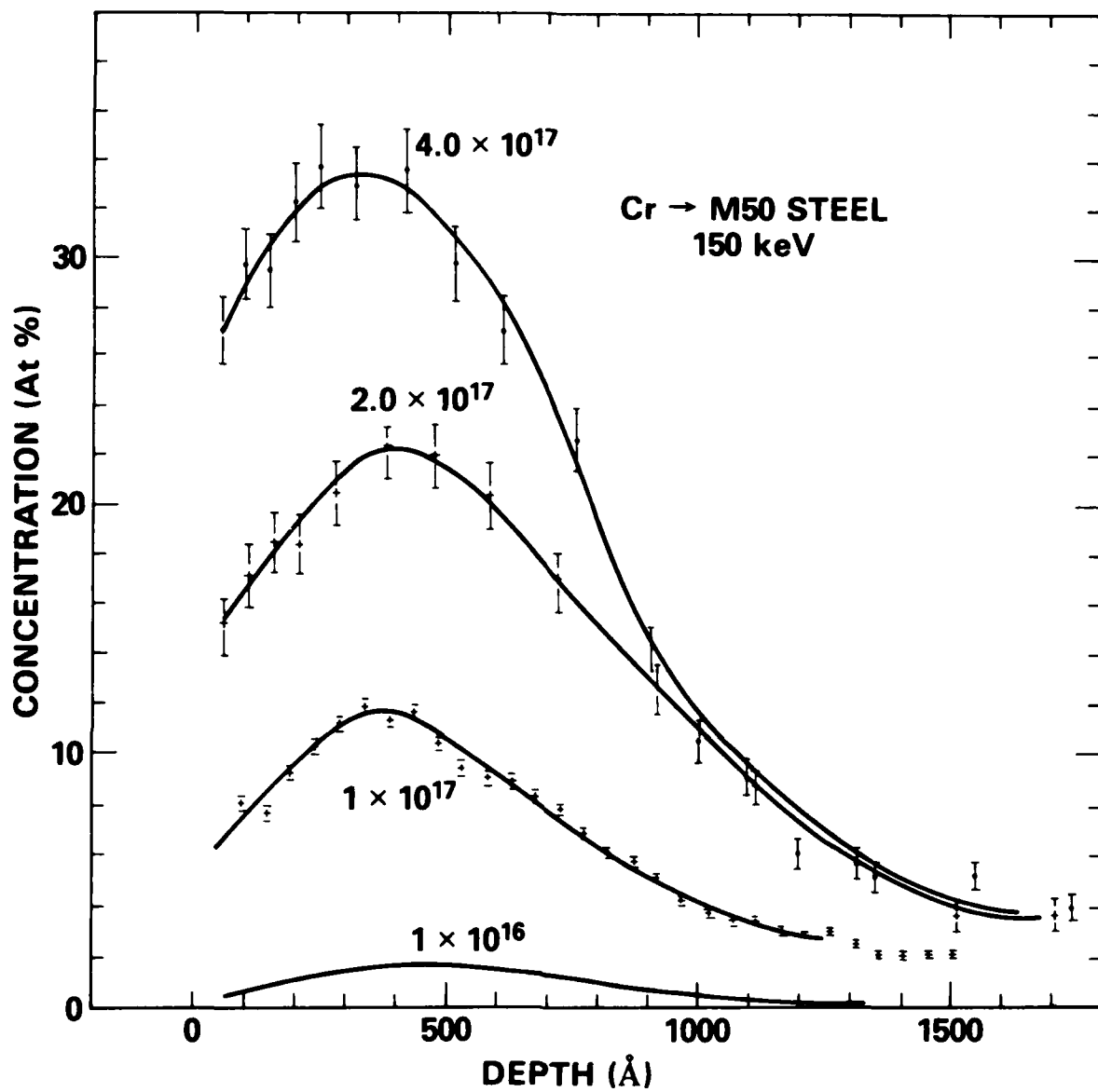


Fig. 4.11 — Concentration vs depth profiles for 150 keV Cr-implanted into AISI M50 for several doses. Profiles were obtained with the Cr ( $\rho, \gamma$ ) Mn resonant reaction technique (from Gossett, 1980).

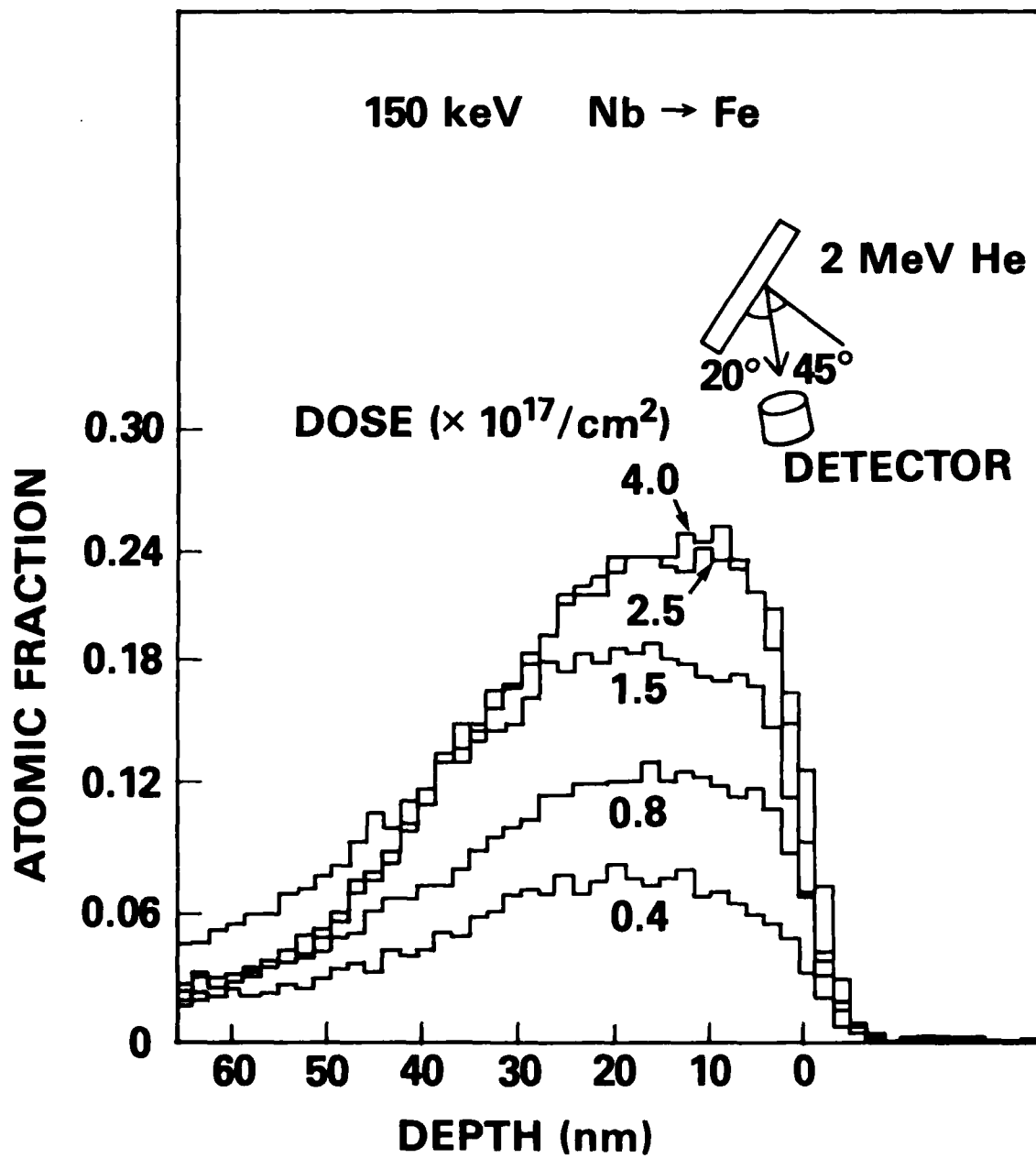


Fig. 4.12 — Concentration vs depth profiles for 150 keV Nb implanted into pure Fe for several doses. Profiles were obtained using 2.0 MeV  $\text{He}^+$  ion Rutherford Backscattering technique (from Hubler, 1984).

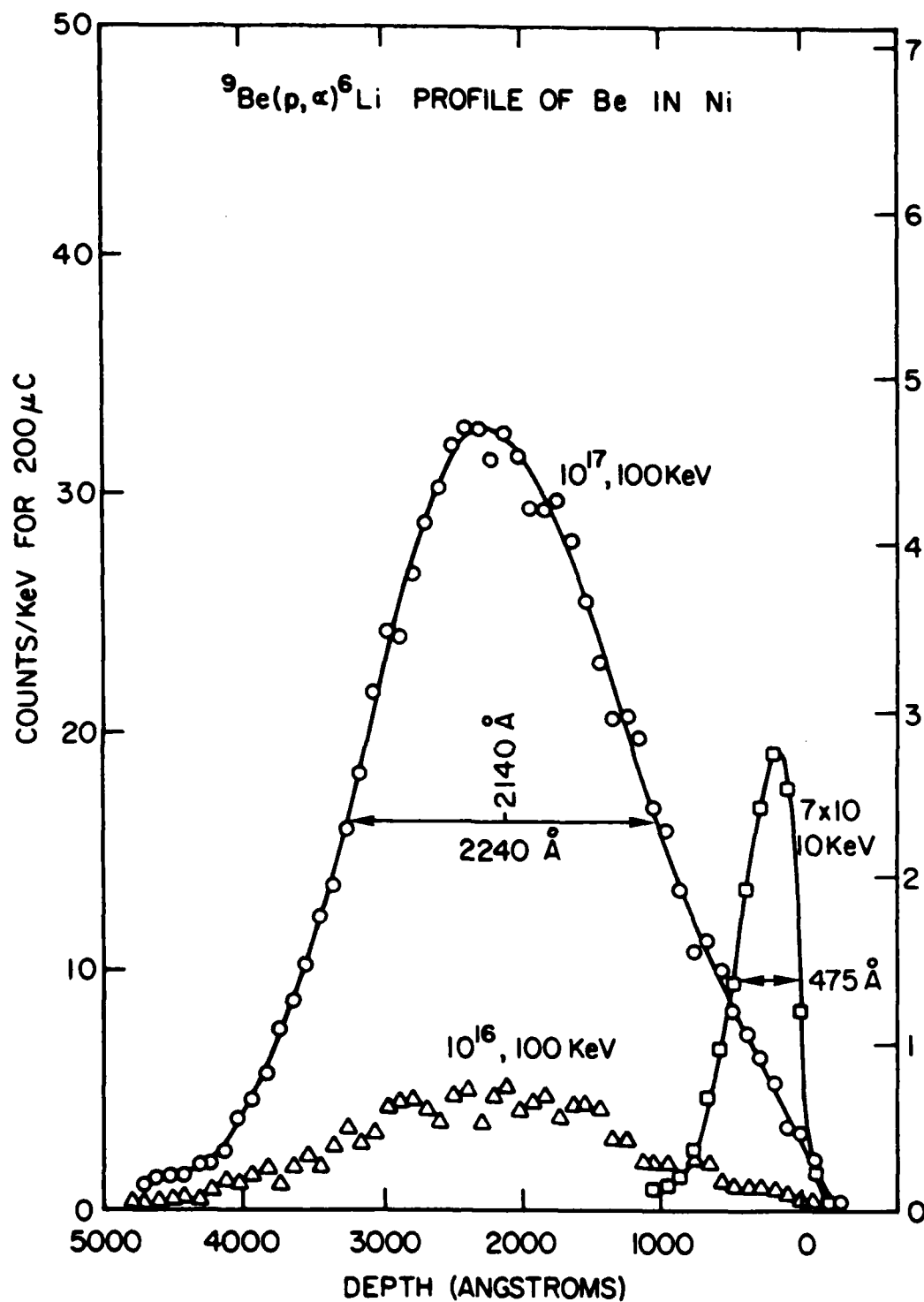


Fig. 4.13 — Concentration vs depth profiles for Be-implanted pure Ni for several ion doses and energies. Profiles were obtained with the Be ( $p,\alpha$ ) Li nuclear reaction technique (from Westmoreland and Hubler, 1977).

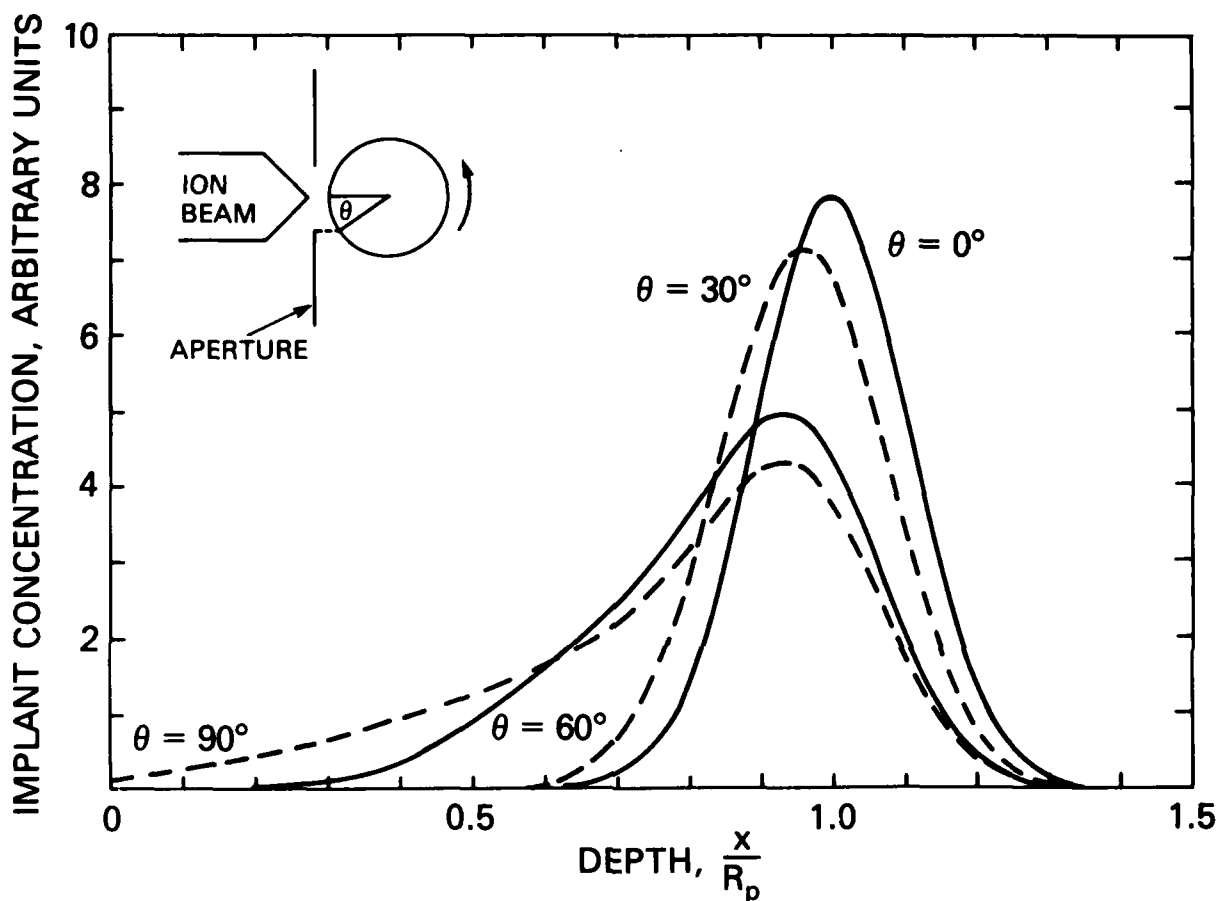


Fig. 4.14 — Theoretical relative concentration profiles for B-implanted Be with the beam incident on a rotating Be cylinder in which an aperture is used to limit the included angles of incidence.  $\theta$  is the maximum angle of incidence and  $R_p/\Delta R_p = 7$  for the cases shown (from Smidt and Sartwell, 1985).

# CONCENTRATION VS DEPTH PROFILES ANGLE DEPENDENCE

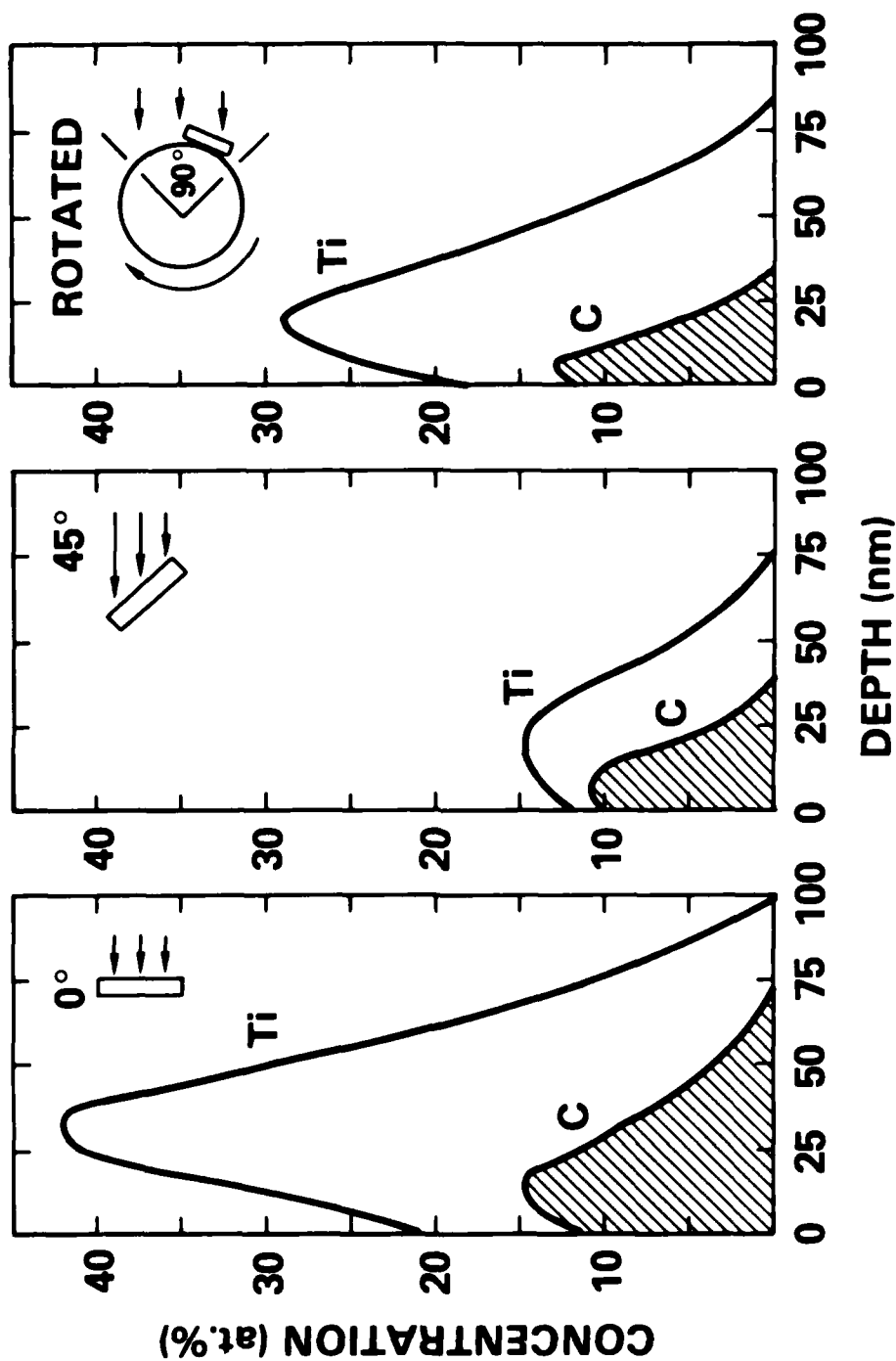


Fig. 4.15 — Auger composition vs depth profiles for steel disks implanted in geometries shown in the figure with Ti ions to a dose of  $4 \times 10^{17}/\text{cm}^2$  at 100 keV (from Singer and Jeffries, 1984).



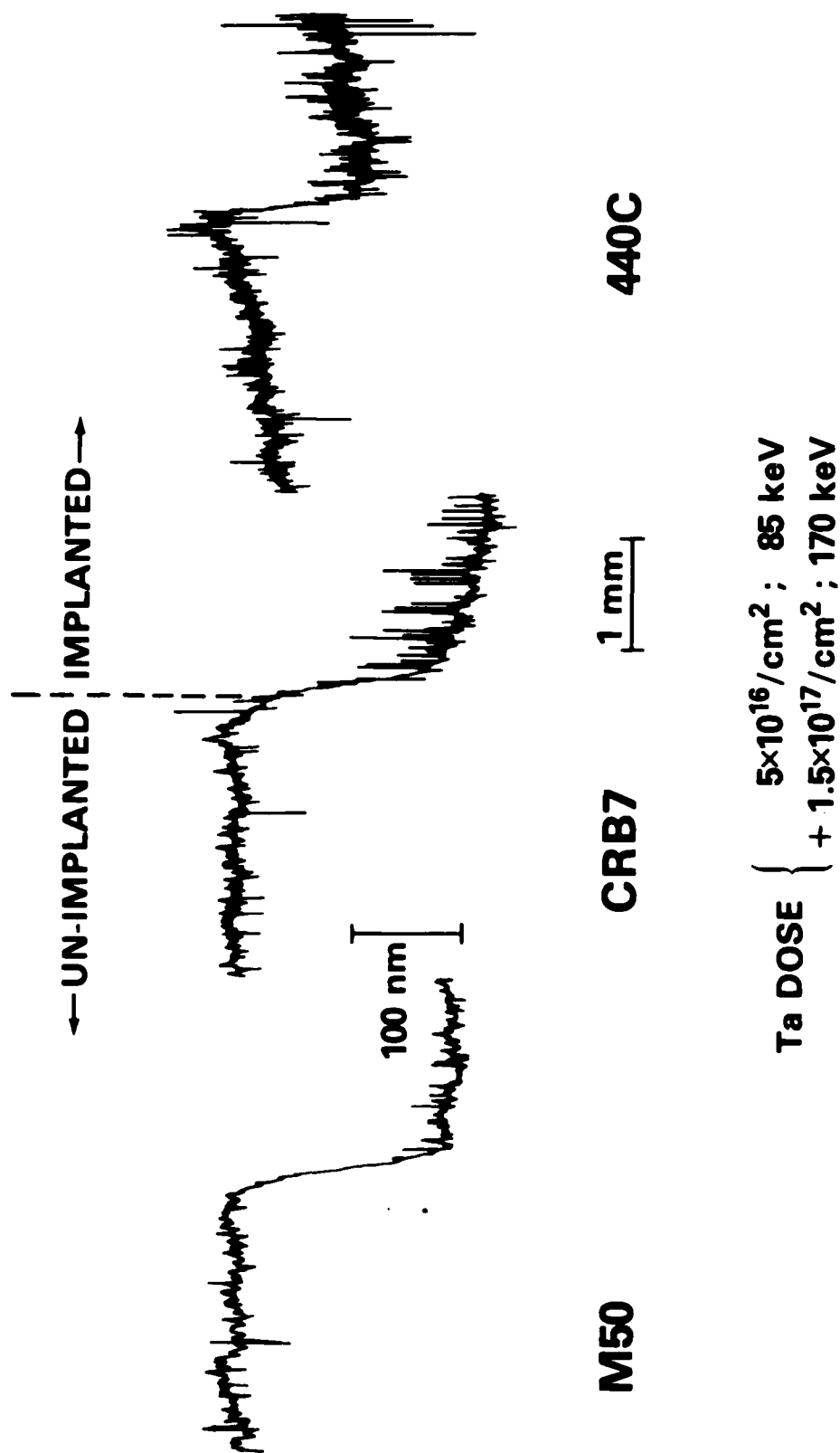
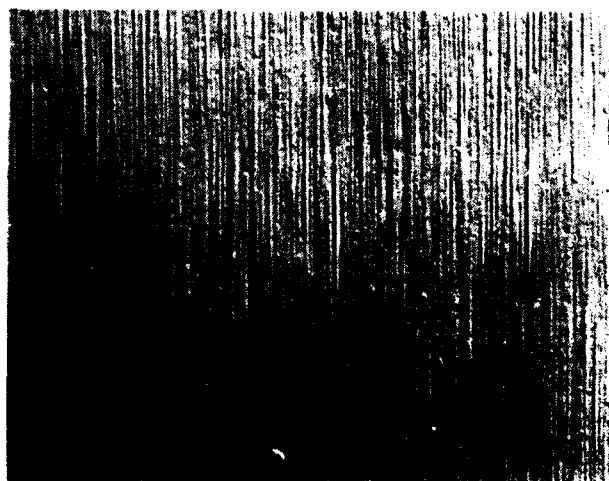


Fig. 4.16 — Surface topological profiles spanning unimplanted and implanted regions on AISI M50, CRB7 and 440C steel rods implanted with Ta ions at the energies and doses shown. The 1 cm diameter rods were rotated at 20 rpm during implantation and the beam was confined to incident angles of  $\pm 30^\circ$  (from Hubler, 1984).

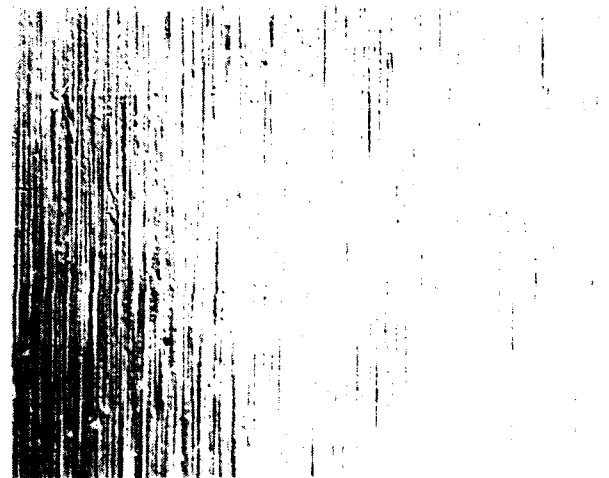
# M50 STEEL

UN-IMPLANTED



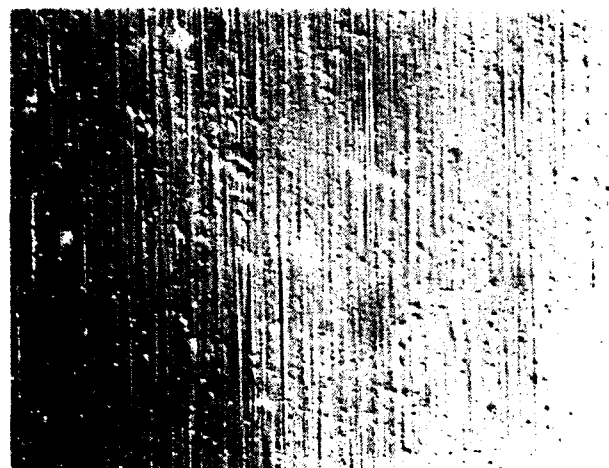
NITROGEN

$5 \times 10^{17} / \text{cm}^2$  ; 150 keV



TANTALUM

$5 \times 10^{16} / \text{cm}^2$  ; 85 keV  
+  $1.5 \times 10^{17} / \text{cm}^2$  ; 170 keV

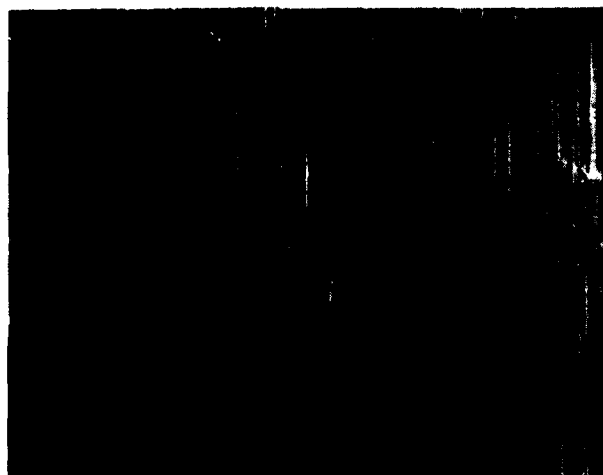


30  $\mu\text{m}$

Fig. 4.17a — Differential interference contrast micrographs of unimplanted, N- or Ta-implanted 3/8" diameter rods. (a) AISI M50 steel (b) AISI CRB7 steel. The rods were rotated at 20 rpm during implantation and beam was confined to incident angles of  $\pm 30^\circ$  (from Hubler, 1984).

# CRB7 STEEL

UN-IMPLANTED



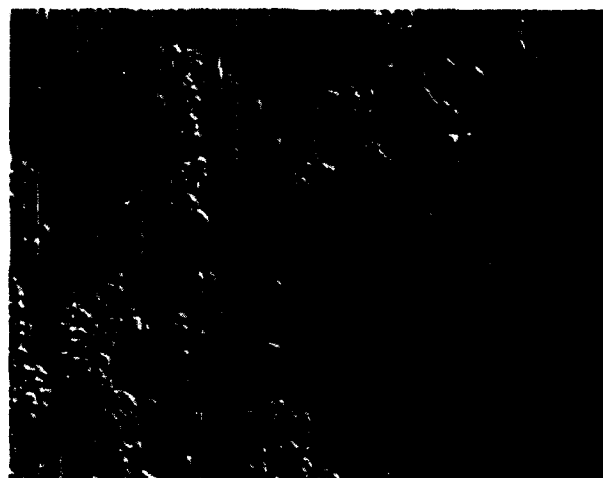
NITROGEN

$5 \times 10^{17} / \text{cm}^2$  ; 150 keV



TANTALUM

$5 \times 10^{16} / \text{cm}^2$  ; 85 keV  
+  $1.5 \times 10^{17} / \text{cm}^2$  ; 170 keV



30 $\mu$ m

Fig. 4.17b — Differential interference contrast micrographs of unimplanted, N- or Ta-implanted 3/8" diameter rods. (a) AISI M50 steel (b) AISI CRB7 steel. The rods were rotated at 20 rpm during implantation and beam was confined to incident angles of  $\pm 30^\circ$  (from Hubler, 1984).

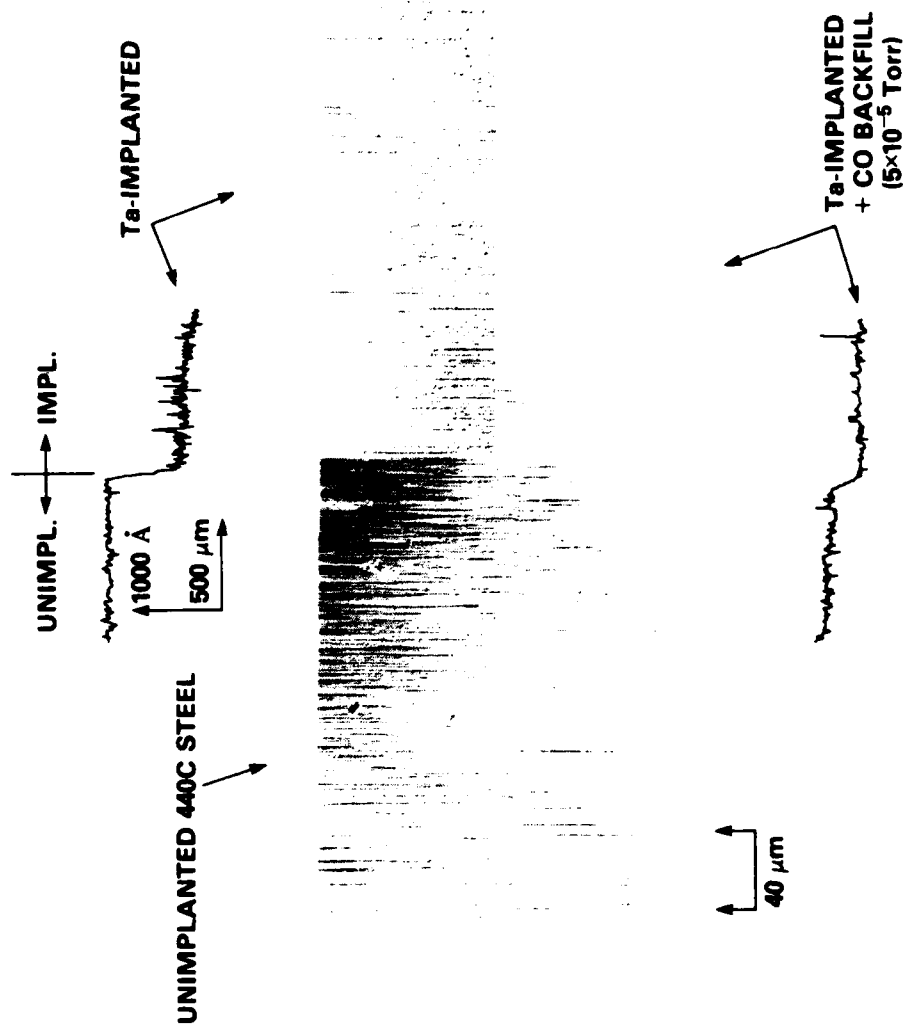


Fig. 4.18 — Surface topological profiles spanning unimplanted and Ta-implanted regions of AISI 440C steel and differential interference contrast micrographs of the same surfaces with and without backfilling target chamber with CO gas during implantation. The Ta implantation conditions were  $0.3 \times 10^{17}/\text{cm}^2$  at 70 keV followed by  $0.8 \times 10^{17}/\text{cm}^2$  at 170 keV (from Hubler, 1984).

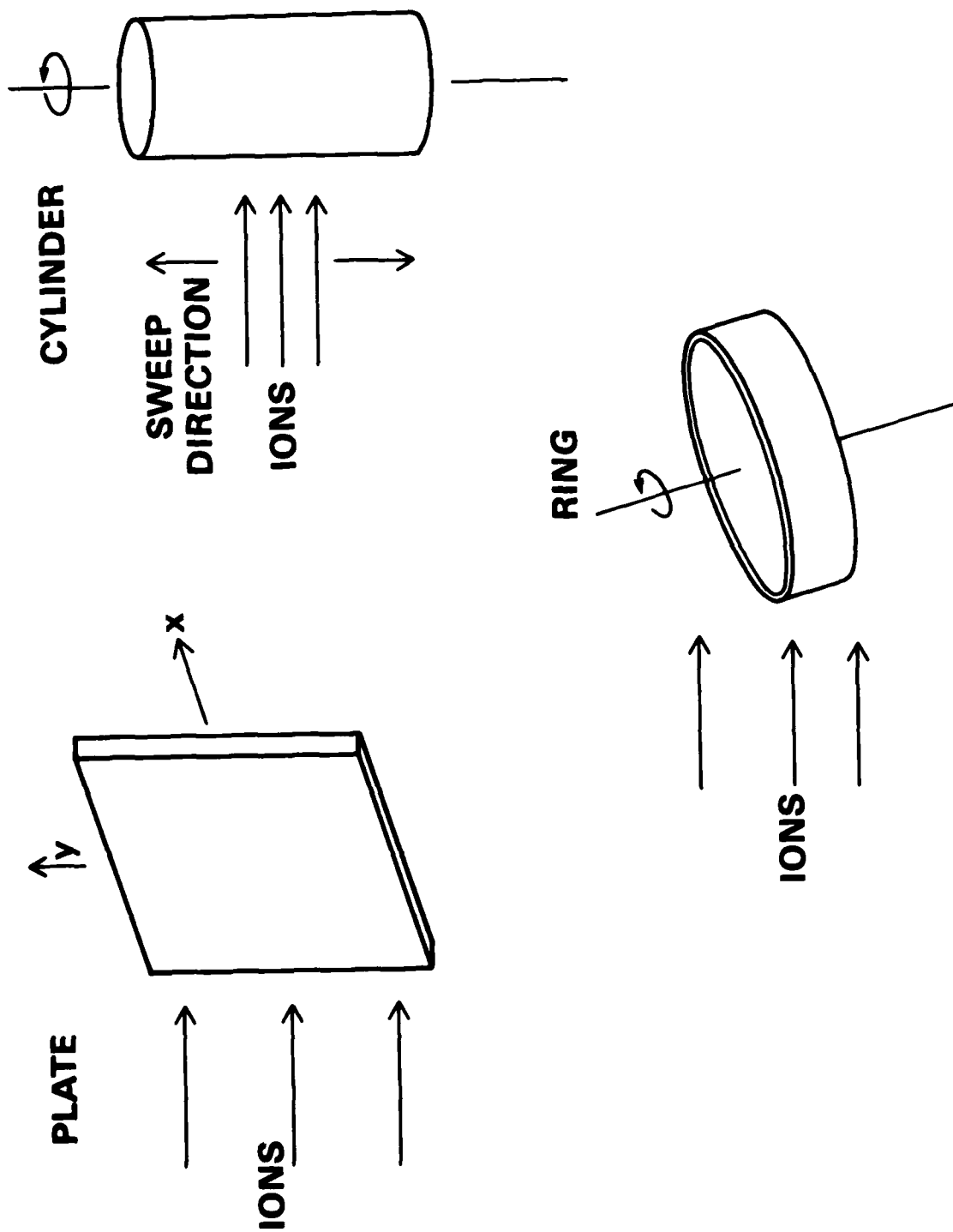


Fig. 4.19 — Schematic representation of some possible workpiece geometries.

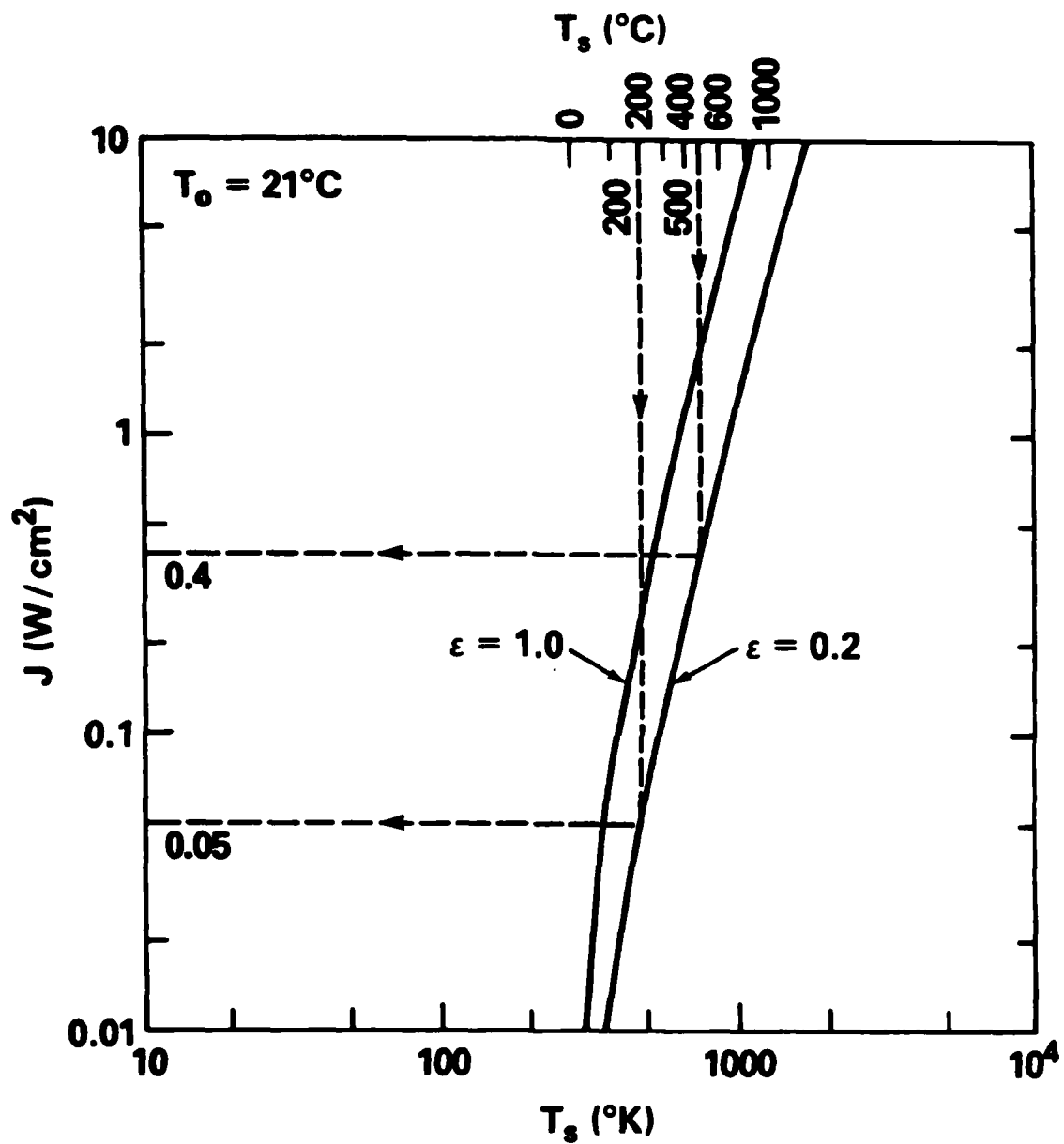


Fig. 4.20 — Power radiated per unit surface area as a function of surface temperature and effective total emissivity,  $\epsilon$ , for surroundings at 21°C (from Grabowski and Kant, 1983).

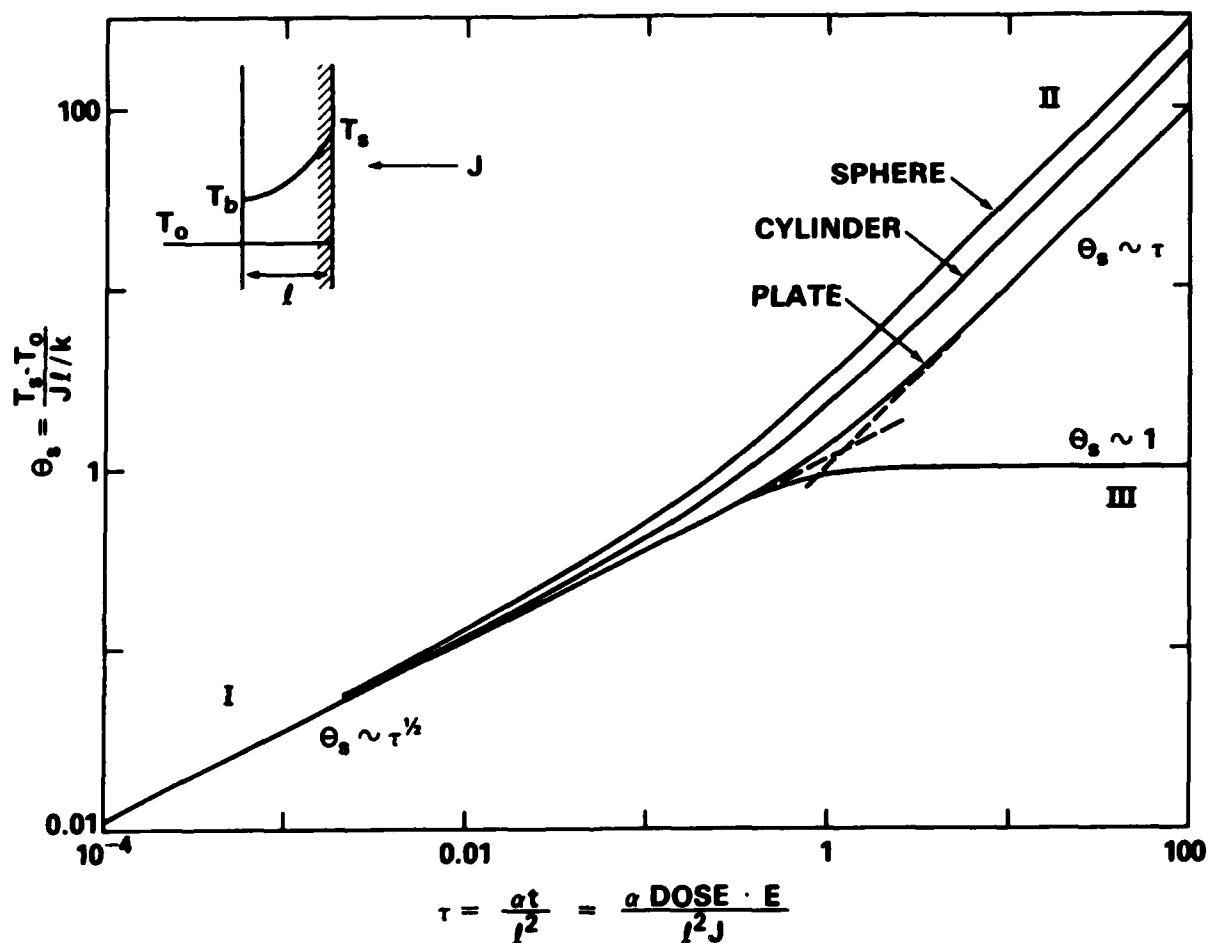


Fig. 4.21 — Dimensionless surface temperature rise,  $\theta_s$ , vs dimensionless time (or dose),  $\tau$ , for incident power density,  $J$ , assuming one dimensional heat transfer.  $l$  represents plate thickness, or cylinder or sphere radius;  $k$ , thermal conductivity;  $\alpha$ , thermal diffusivity;  $\phi$ , ion dose; and  $E$ , ion energy. Heat is withdrawn from the target in region III by a heat sink (from Grabowski and Kant, 1983).

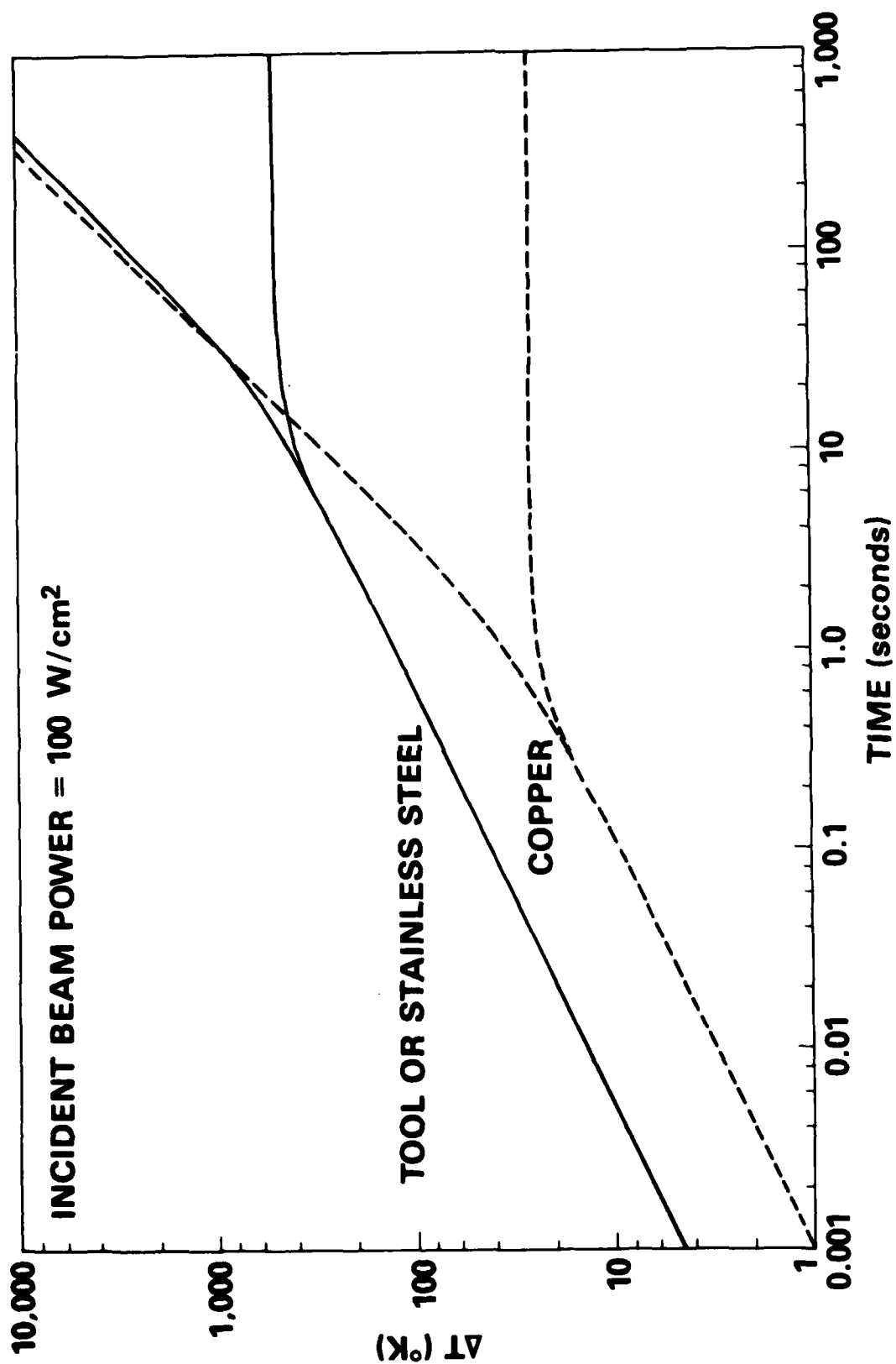
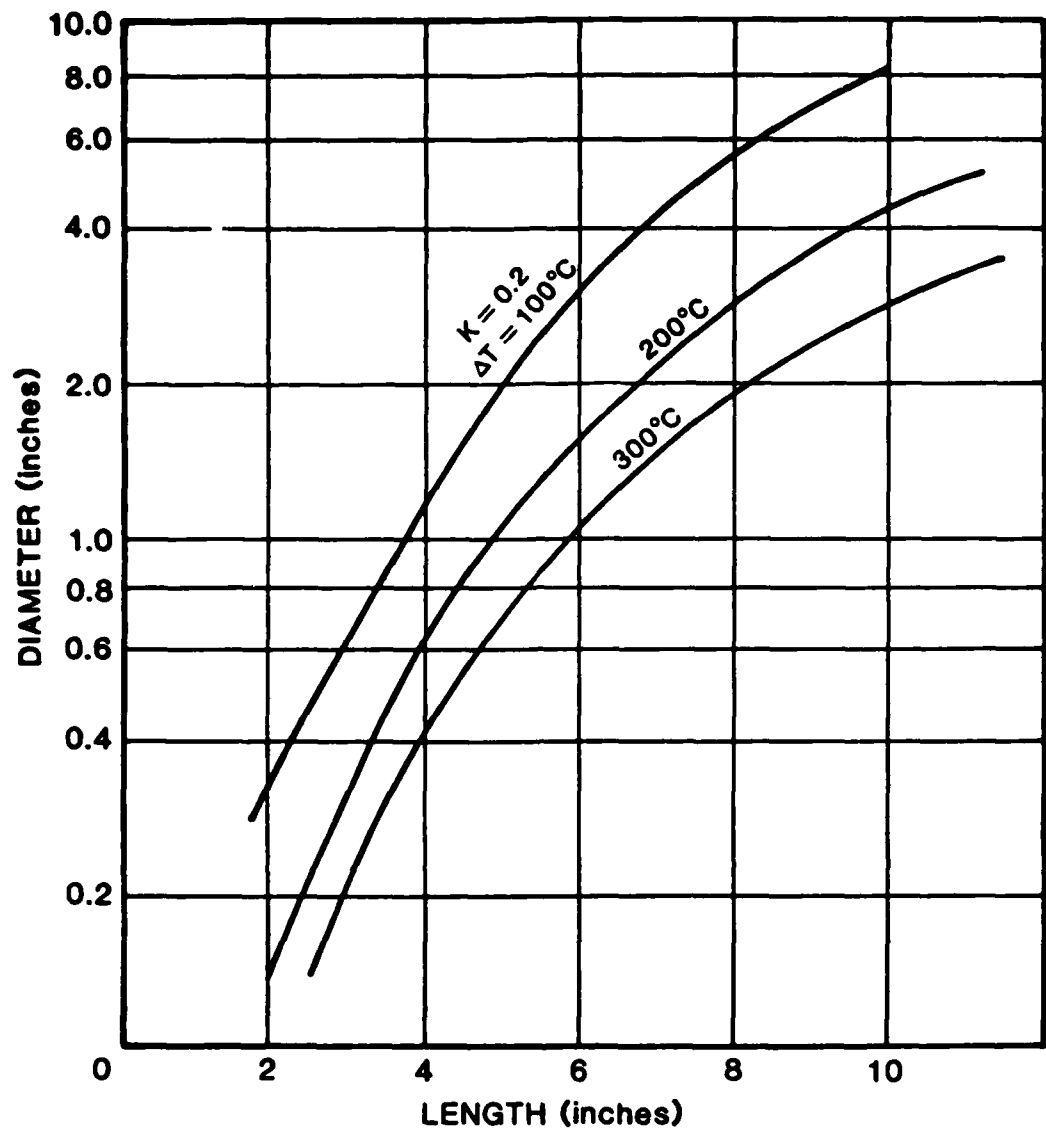


Fig. 4.22 — Surface temperature rise vs time for an incident power density of  $100 \text{ W/cm}^2$  obtained from Figure (4.21) for the specific cases of 1 cm thick steel and copper plates.





$$\Delta T \propto \frac{J \left( \frac{W}{\text{cm}^2} \right) L^2 D}{2 K A_{\text{eff}}}$$

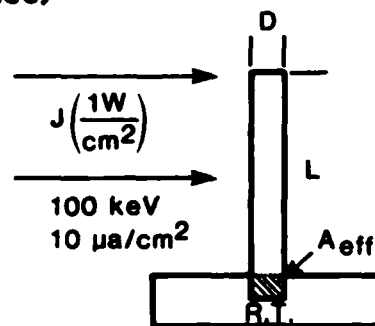


Fig. 4.23 — Temperature rise of tool steel rod versus the rod diameter and length for an incident power density of  $1 \text{ W}/\text{cm}^2$  along the entire rod length. The rod is assumed to be heat sunk at one end over a length equal to one diameter with an interface conductance of  $1 (\text{W}/\text{cm}^2 - \text{K})$  (after Hirvonen, 1985).



**Fig. 4.24 — Photograph of apparatus used to rotate and water-cool samples in an ion implantation vacuum chamber (from Grabowski et. al., 1985).**

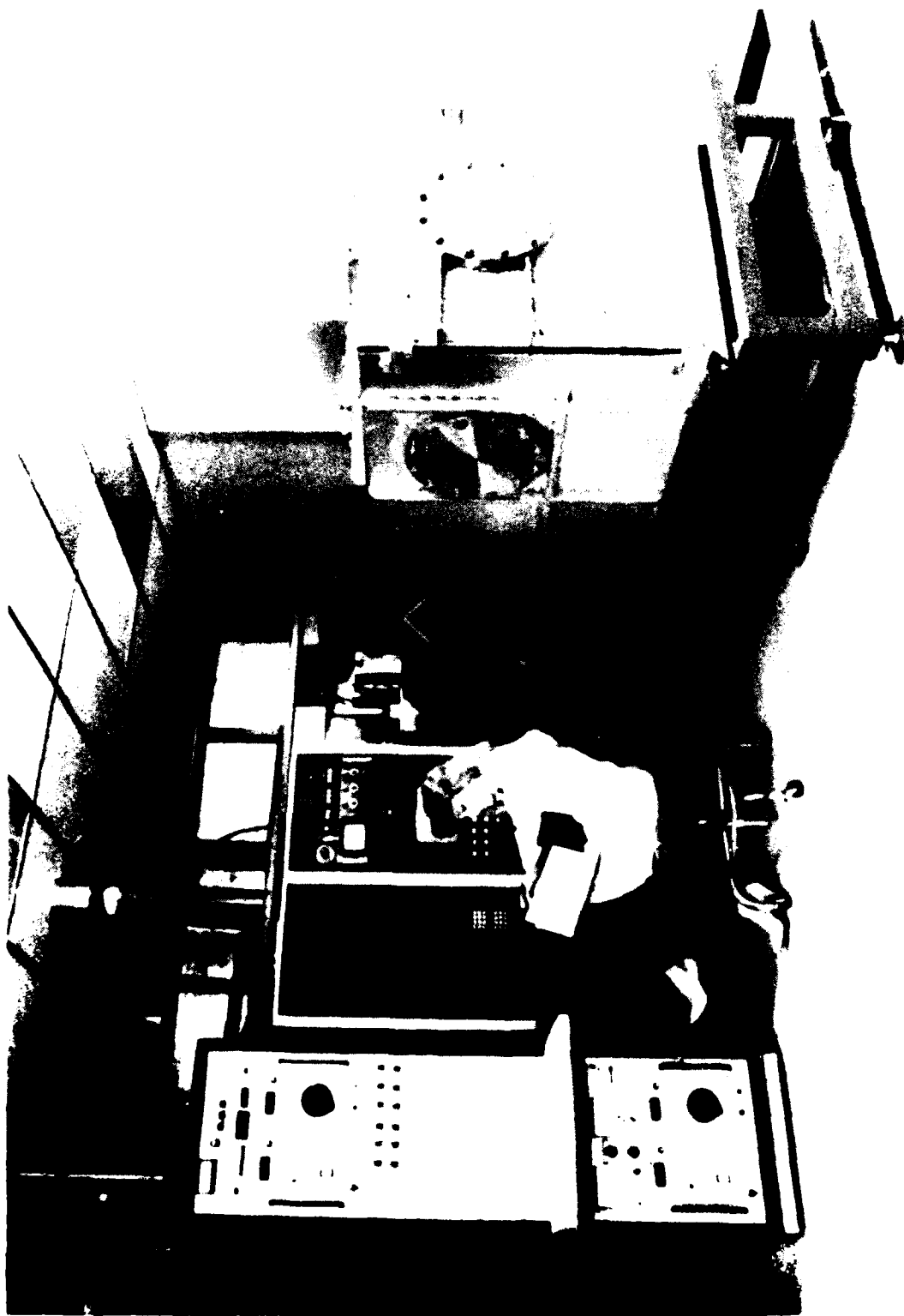


Fig. 4.25 — Photograph of Navy Manufacturing Technology Implantation Facility located at Spire Corporation. From left to right: Ion Implanter, defocussing section, work piece manipulation chamber.

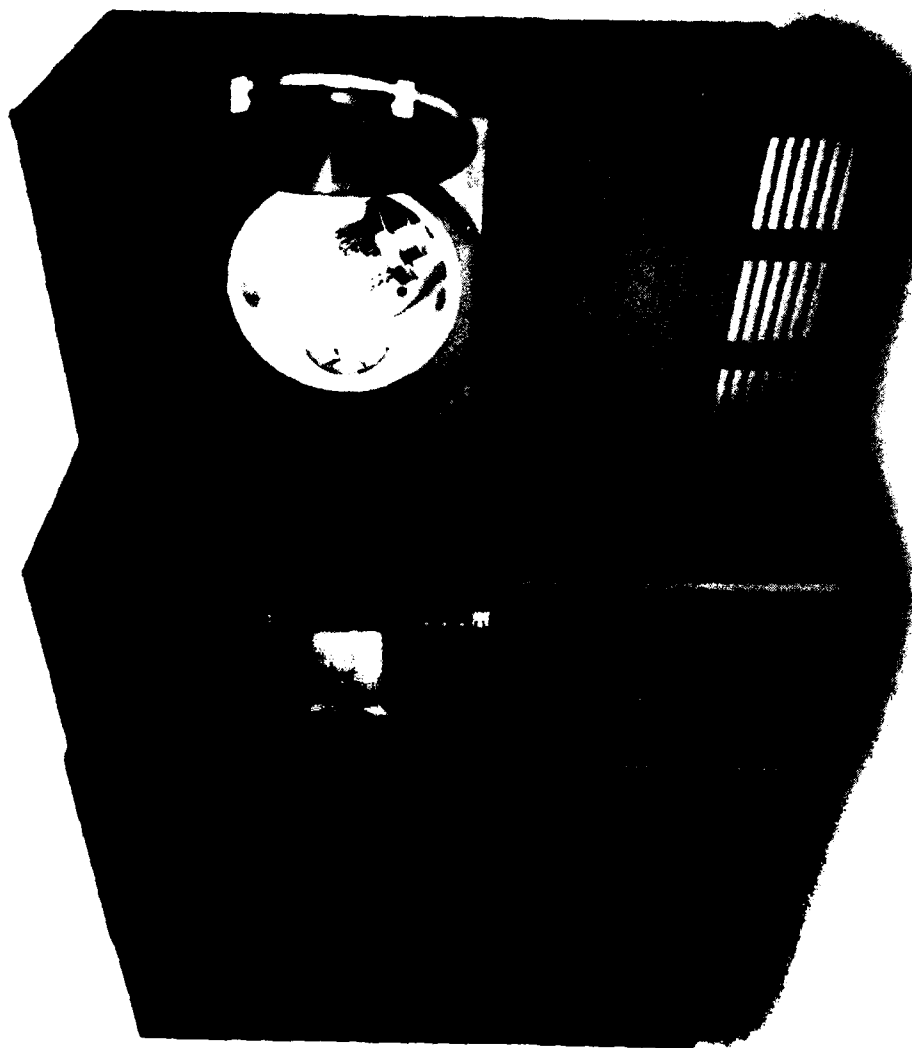


Fig. 4.26 — Photograph of commercially available non mass-analyzed ion-implanter.

END

5-87

DTIC